POLITECNICO
MILANO 1863

Scuola di Ingegneria Industriale e dell'Informazione
Dipartimento di Scienze e Tecnologie Aerospaziali
Corso di Laurea in Ingegneria Aeronautica

FLUTTER ANALYSIS OF OPEN ROTORS

Relatore: Paolo MANTEGAZZA
Co-relatore: Andrea PARRINELLO

Tesi di laurea di:
Davide PREDERI
Matr. 799776

Anno Accademico 2014 - 2015

Davide PREDERI: *FLUTTER ANALYSIS OF OPEN ROTORS,* Tesi di Laurea Specialistica, © anno accademico 2014 - 2015.

A Giacomo e Raffaella,
con sincero affetto.

ABSTRACT

The thesis is aimed to show the importance of aeroelastic analysis, e.g. flutter prediction, in the preliminary design of Contra Rotating Open Rotor (CROR). To this end, the structural sub-system is modelled with the Finite-Element (FE) solvers NASTRAN® and ANSYS®. A comparison of natural frequencies and mode shapes is performed using both tetrahedral and shell element models. The aerodynamic subsystem is modelled with the Finite-Volume (FV) full potential solver S^T. The solver model unsteady transonic flows by means of an independent approximation of the density and velocity potential fields. It can also model non-isentropic flows thanks to a new form of Kutta condition [53–55]. An *ad hoc* technique is developed for simulating the flow field around two lifting bodies with relative motion, i.e. the front and rear propeller stages. The flutter analyses are carried out using the so-called K-E(fficient) method (also used in NASTRAN® aeroelastic toolbox) and a root-tracking non-linear method for computing the $V-g$ and $V-\omega$ diagrams.

The effectiveness of the proposed aeroelastic analysis for Single Rotating Propfan (SRP) is successfully assessed by tackling a set of realistic dynamic problems and by comparing the results with reference experimental and numerical data available in literature and with the results obtained by the Euler flow solver *AeroX* [44, 58]. The results of the CROR cannot be validated because there are neither data available in the literature nor other alternative procedures.

Key words: aeroelasticity, contra-rotating open rotor, transonic flow, flutter, full potential.

SOMMARIO

Questo lavoro di tesi è volto a dimostrare l'importanza dell'analisi aeroelastica, e.g. predizione del flutter, nell'analisi preliminare di Contra Rotating Open Rotor (CROR). A tal fine, il sistema strutturale è modellato con i programmi ad elementi finiti NASTRAN® e ANSYS®. Viene condoto un confronto delle frequenze proprie e delle forme modali usando sia modelli ad elementi solidi (tetraedri) sia ad elementi di piastra. Il sistema aerodinamico è modellato con il solutore a potenziale a volumi finiti S^T. Il programma risolve correnti transoniche non stazionarie grazie ad un'approssimazione indipendente per i campi della densità e del potenziale di velocità. Questo è anche in grado di risolvere correnti non isentropiche grazie ad una nuova forma della condizione di Kutta [53–55]. È stata sviluppata una tecnica *ad hoc* per simulare le correnti attorno a due corpi portanti in moto relativo (cioè lo stadio anteriore e posteriore). Le analisi di flutter sono effetuate con il metodo K-E(fficiente) (già usato nel toolbox aeroelastico di NASTRAN®) e con un metodo non lineare di inseguimento degli autovalori in modo da tracciare i diagrammi $V-g$ e $V-\omega$.

La validazione della tecnica proposta per l'analisi aeroelastica di Single Rotating Propfan è ampiamente supportata dal confronto dei risultati ottenuti con i dati sperimentali e numerici presenti in letteratura e con quelli ottenuti dal solutore euleriano *AeroX* [44, 58]. Non è stato possibile validare le tecniche per il CROR poichè non sono presenti dati in letteratura e non sono reperibili altri strumenti di analisi.
Parole chiave: aeroelasticità, contra-rotating open rotor, regime transonico, flutter, aerodinamica a potenziale.

Grazie per i
magnifi"chi" regali.

— Un Amico

RINGRAZIAMENTI

Voglio ringraziare particolarmente il Professor Mantegazza. Il suo supporto e il suo incoraggiamento sono stati fondamentali. Lo ringrazio soprattutto per gli insegnamenti scolastici e non che mi ha fornito: non avrei potuto desiderare di meglio.

Desidero ringraziare Andrea Parrinello per tutto il tempo che mi ha dedicato e per la pazienza che ha avuto. I suoi consigli e le sue soluzioni sono state importantissime.

Ringrazio anche Andrea Gadda per il suo prezioso contributo durante la fase di validazione di tutti i risultati. La sua attività è sicuramente un valore aggiunto a questo lavoro.

Dedico questo lavoro di tesi ai miei genitori Giacomo e Raffaella. Non finirò MAI di ringraziarli per avermi permesso di intraprendere questo percorso di studi così arduo e difficile. Li ringrazio anche per avermi spronato nei momenti difficili, permettendomi così di diventare l'uomo che sono. Non potrei proprio desiderare genitori migliori.

Milano, anno accademico 2014 - 2015 D. P.

CONTENTS

1 INTRODUCTION 1
- 1.1 What is an open rotor? . . . 1
- 1.2 Challenges . . . 2
- 1.3 Propfan Research and Development . . . 5
- 1.4 Aeroelasticity in Open Rotor Research . . . 6
- 1.5 Overview of the Thesis . . . 8

2 AERODYNAMIC SUB-SYSTEM 10
- 2.1 Rotating Frame Formulation of Fluid Dynamics . . . 10
  - 2.1.1 Euler Equations for Rotating Flows . . . 11
  - 2.1.2 Bernoulli Theorem for Rotating Flows . . . 13
- 2.2 Non Isentropic Potential ALE Flow Formulation . . . 15
  - 2.2.1 Compressible Potential Flow Model . . . 15
  - 2.2.2 Entropy Correction and Wake Equations . . . 17
- 2.3 External Boundary Conditions . . . 20
- 2.4 Boundary Conditions on the Body . . . 21
- 2.5 Periodic Boundaries . . . 22
- 2.6 Wake Influence and Domain size . . . 28

3 STRUCTURAL SUB-SYSTEM 30
- 3.1 Reference Frames . . . 30
- 3.2 Kinematic Relations . . . 31
- 3.3 Virtual Work Principle of Inertia Forces . . . 33
- 3.4 Virtual Work Principle of Elastic Forces . . . 37
- 3.5 Numerical Procedures . . . 39
  - 3.5.1 Building, assembly and factorization of various matrices . . . 39
  - 3.5.2 Trim with centrifugal loads . . . 40
  - 3.5.3 Building the *prestress stiffness* matrix . . . 41
  - 3.5.4 Eigenproblem: frequencies and modes . . . 41
  - 3.5.5 Building the reduced system . . . 41

4 INTERFACE 42
- 4.1 Background . . . 42
- 4.2 Structural Sub-System . . . 44
- 4.3 Fluid-Structure Coupling . . . 45
  - 4.3.1 Moving Least Squares . . . 45
- 4.4 Transpiration Boundary Condition . . . 46
  - 4.4.1 Linearised Formulation . . . 47
  - 4.4.2 Non Linear Formulation . . . 48
- 4.5 Boundary Condition for Contra Rotating Blade Rows . 48

4.5.1 Boundary Conditions on the Real Body 52
4.5.2 Transpiration Boundary Condition 52

5 FLUTTER ANALYSIS 53
5.1 Rotor Aeroleasticity 53
5.2 Aerodynamic Transfer Function 55
5.3 Flutter Calculation 58
5.3.1 K-E(fficient) Method 58
5.3.2 Flutter Eigensolution as a Nonlinear Problem . 60

6 RESULTS 63
6.1 TEST CASE 1 63
6.1.1 Aerodynamic Analyses of a Single Rotating Propeller (SRP) 65
6.1.2 Aerodynamic Analyses of a Contra-Rotating Open Rotor (CROR) 68
6.2 TEST CASE 2 70
6.2.1 FE Analyses 70
6.2.2 Aerodynamic Analysis 73
6.2.3 Flutter Analysis 74
6.3 TEST CASE 3 81
6.3.1 FE Analyses 81
6.3.2 Aerodynamic Analysis 87
6.3.3 Aeroelastic Trim 90
6.3.4 Flutter Analysis 94
6.4 TEST CASE 4 96
6.4.1 Aerodynamic Analyses 96
6.4.2 Processing of the Aerodynamic Modal Responses 96
6.4.3 Flutter Analyses 99

7 CONCLUDING REMARKS AND FUTURE DEVELOPMENTS 102

A VALIDATION OF "GHOST TECHNIQUE" 105
A.1 Aligned Airfoils 107
A.2 Misaligned Airfoils 111

B AERODYNAMIC TRANSFER FUNCTIONS 115
B.1 Numerical Results 115

LIST OF FIGURES

Figure 1 Different configuration in Open Rotors taken from: ®www.redstar.gr and ®www.gfdiscovery.blogspot.it . . . 1
Figure 2 Problematic Airframe Installation. ®www.airinsight.com/ . . . 3
Figure 3 Compatible Aircraft Configurations for Integration with Airframes . . . 4
Figure 4 Experimental Setup of SR-5 propeller [30] . . . 5
Figure 5 Various Blade Model of [30] . . . 5
Figure 6 Airframe Installation at Flight Test. ®www.airinsight.com . . . 6
Figure 7 Flutter Boundaries - [30] . . . 7
Figure 8 Domain Decomposition. . . . 18
Figure 9 Periodic Domain XY view. . . . 23
Figure 10 Periodic Faces. . . . 24
Figure 11 Lateral Surface Mesh. . . . 24
Figure 12 Example of the periodic boundary for a 2D application. . . . 25
Figure 13 Periodic domain and wake representation for a 3D case - view 1. . . . 26
Figure 14 Periodic domain and wake representation for a 3D case - view 2. . . . 27
Figure 15 Blade Element Momentum Theory - www.sites.google.com/site/aerodynamics4students/ . . . 29
Figure 16 Number of "Wake Turns" VS Thrust Relative Error [%] . . . 29
Figure 17 fig:Different Aerodynamic Models . . . 43
Figure 18 MLS interface for SR-3 propfan blade. The left-hand image is the structural mesh for FEM analysis (SHELL elements). The right-hand image is the aerodynamic mesh for FV analysis. . . . 46
Figure 19 Vortexes interaction in CRORs. [73] . . . 49
Figure 20 Relative motion between the two rotor blades. In the first simulation, the meshed blade is the black one, while the ghost (gray) is located downstream. . . . 50
Figure 21 Visualization of the Ψ angle in both cases. . . . 51
Figure 22 Physical explanation of influence coefficients [71] 54

Figure 23 A bending vibration with $\sigma_n = 180°$ of turbomachines blades is here represented. It can be inferred that the perturbations are periodic every two blade passages. [68] 55
Figure 24 Blendend step input $q(\tau)$ and its derivative $\dot{q}(\tau)$ as a function of time τ. 57
Figure 25 62
Figure 26 Generic Blade Design Characteristic. 64
Figure 27 Blade shape available on [63] 64
Figure 28 Comparison between the results obtained by the reference [63], S^T and AX. 66
Figure 29 Comparison between Mach distributions. 67
Figure 30 Comparison between Cp distributions. 67
Figure 31 Trend of the C_T of the front (black) and after (gray) rotors. 69
Figure 32 SR-5 *NASTRAN*® structural model 70
Figure 33 Rotating Mode Shapes of the SR-5 blade. 72
Figure 34 Comparison between Mach distributions. 73
Figure 35 Comparison between Cp distributions. 74
Figure 36 Aerodynamic Modal Responses of Case 2. Only the first two rows and columns are reported. (●) for S^T and (●) for AeroX. 75
Figure 37 Aerodynamic Modal Responses of Case 2. Only the first two rows and columns are reported. (●) for S^T and (●) for AeroX. 76
Figure 38 V-f of Case 2. (●) for S^T and (●) for AeroX. . . . 77
Figure 39 Reference V-f of Case 2. 77
Figure 40 V-g of Case 2. (●) for S^T and (●) for AeroX. . . . 78
Figure 41 Reference V-g of Case 2. 78
Figure 42 V-f of Case 2. (●) for S^T and (●) for AeroX. . . . 79
Figure 43 Reference V-f of Case 2. 79
Figure 44 V-g of Case 2. (●) for S^T and (●) for AeroX. . . . 80
Figure 45 Reference V-g of Case 2. 80
Figure 46 CAD of the blade [60] 81
Figure 47 84
Figure 48 85
Figure 49 86
Figure 50 Mach distributions for $V_\infty = 70$ m/s at $h = 0$ km. 88
Figure 51 Cp distributions for $V_\infty = 70$ m/s at $h = 0$ km. . 88
Figure 52 Mach distributions for $V_\infty = 205$ m/s at $h = 10$ km. 89
Figure 53 Cp distributions for $V_\infty = 202$ m/s at $h = 10$ km. 89
Figure 54 Relative error between the solutions calculated with the modal basis and with SOL 106 in NASTRAN®. 92
Figure 55 Relative error between mode shapes including or not the aerodynamic load. 93
Figure 56 $V - g$ and $V - \omega$ diagrams at 0 meters 95

Figure 57 $V-g$ and $V-\omega$ diagrams at 5.000 meters . . . 95
Figure 58 $V-g$ and $V-\omega$ diagrams at 10.000 meters . . . 95
Figure 59 Thrust coefficient C_T of the front (●) and after (●) rotors at the asymptotic velocity $V_\infty = 130\ m/s$. 97
Figure 60 Example of the frequency spectrum. 98
Figure 61 Example of the filtering of an element of the matrix $\mathbf{H_{am}}(k, M_\infty)$ with a Butterworth filter of 15th order and cut-off reduced frequency of 2.27. 99
Figure 62 Example of the interpolation of an element of the matrix $\mathbf{H_{am}}(k, M_\infty)$. 99
Figure 63 $V-g$ and $V-\omega$ with $\Phi = 0°$ 100
Figure 64 $V-g$ and $V-\omega$ with $\Phi = 180°$ 101
Figure 65 The density field $\rho(\mathbf{x}, \bar{t})$ of each STEP is represented. 106
Figure 66 Detail of grid with two NACA. 107
Figure 67 Detail of the grid with one NACA (XY view). . . 108
Figure 68 Cp distributions over the airfoils. The *reference* solution is (●) while the *ghost* one is dashed-(●). 109
Figure 69 Density Fields for $M_\infty = 0.5$ 110
Figure 70 Density Fields for $M_\infty = 0.7$ 110
Figure 71 Detail of grid 111
Figure 72 Cp distributions over the airfoils. The *reference* solution is (●) while the *ghost* one is dashed-(●). 113
Figure 73 Density Fields for $M_\infty = 0.5$ 114
Figure 74 Density Fields for $M_\infty = 0.7$ 114
Figure 75 Comparison of the aerodynamic transfer functions matrix $\mathbf{Q_{am}}(t)$ computed with S^T (●) and AeroX (●) at $V_\infty = 70\ m/s$. 117
Figure 76 Comparison of the aerodynamic transfer functions matrix $\mathbf{H_{am}}(k, M_\infty)$ computed with S^T (●) and AeroX (●) at $V_\infty = 70\ m/s$. The marker of the real part is the square, while that of the imaginary part is the circle. 119

LIST OF TABLES

Table 1 U.L. strain and stress tensors 40
Table 2 Flight Conditions 65

Table 3	Blade Pitch Angle at 75% of span-wise direction for equally partitioned thrust between both rotors at an angular velocity of $\Omega = 895$ RPM and at an altitude of 35.000 ft	68
Table 4	Comparison of the most important parameter of CROR.	69
Table 5	Non Rotating Normal Frequencies [Hz] of the SR-5 blade	71
Table 6	Rotating Normal Frequencies [Hz] of the SR-5 blade	71
Table 7	SR-5 Operating Conditions	73
Table 8	Unsteady Aerodynamics Data	74
Table 9	Material Properties	82
Table 10	Non Rotating Normal Frequencies [Hz].	83
Table 11	Rotating Normal Frequencies [Hz] with $\Omega = 1900$RPM.	83
Table 12	Dependency of Eigenvalues with variable pitch angle at $\Omega = 895$ RPM	85
Table 13	Non Rotating Frequencies [Hz] (Case 1)	86
Table 14	Rotating Frequencies [Hz] with $\Omega = 895$RPM (Case 1)	87
Table 15	Relationship between $\beta_{0\%}$ (at the root of the blade) and V_∞	87
Table 16	Comparing Normal Frequencies [Hz] with or without the aerodynamic pressure load	91
Table 17	Pitch Angles $\beta_{0\%}$ for CROR.	96
Table 18	Asymptotic condition for the test cases. The polytropic ideal gas model ($\gamma = 1.4$) is employed.	105
Table 19	Aerodynamic coefficients for $M_\infty = 0.5$. The *Reference Mesh* gives the exact solution while the *Ghost Technique* exploits the so called formulation.	108
Table 20	Aerodynamic coefficients for $M_\infty = 0.7$. The *Reference Mesh* gives the exact solution while the *Ghost Technique* exploits the so called formulation.	108
Table 21	Aerodynamic coefficients for $M_\infty = 0.5$. The *Reference Mesh* gives the exact solution while the *Ghost Technique* exploits the so called formulation.	112
Table 22	Aerodynamic coefficients for $M_\infty = 0.7$. The *Reference Mesh* gives the exact solution while the *Ghost Technique* exploits the so called formulation.	112

1

INTRODUCTION

In recent years, there has been a renewed interest in open rotor propulsion systems, since they could be an improved solution for the next generation of transport aircraft. In fact, open-rotors are more fuel-efficient and environmentally friendly than turbofan but more noisy and complex to built. Furthermore, noise, fluid-structure and rotor-to-rotor interactions remain key issues to be solved for a fully accomplished design of open rotor engines.

1.1 WHAT IS AN OPEN ROTOR?

Simply explained, an open rotor is a gas turbine whose fan stage is not within the nacelle. Two common open rotor configurations exist: puller and pusher. The puller configuration has propellers mounted at the front of the engine, while the pusher configuration mounts them directly behind the turbine stage.

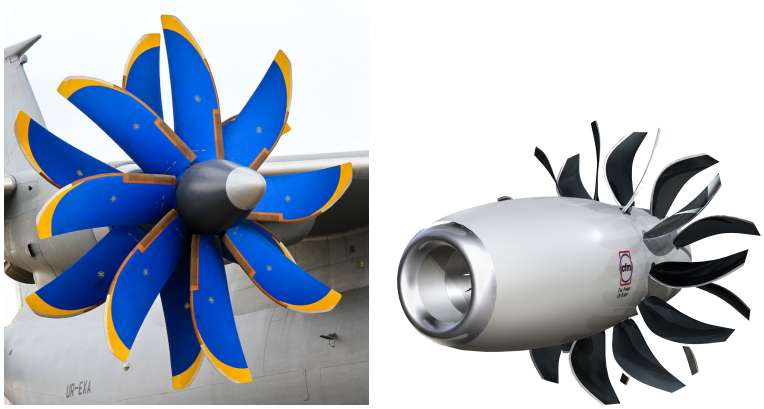

(a) *Puller CROR.* **(b)** *Pusher CROR.*

Figure 1: Different configuration in Open Rotors taken from: ®`www.redstar.gr` and ®`www.gfdiscovery.blogspot.it`

Both can have either a single propeller or a pair of contra-rotating propellers; however, historically [36], puller configurations have generally had only one propeller while pusher configurations have usually had two contra-rotating propellers. The advantage of using a second propeller stage is that the rotational component of velocity (swirl) of the air leaving the first stage will be realigned through the second stage, so increasing the effective engine thrust. This means that to

achieve a given thrust, an open rotor with contra-rotating blades can have a reduced propeller diameter and/or angular velocity compared to a single stage engine. Reduced propeller diameter offers the benefit of an easier integration within an aircraft design. As the noise generated by the propeller increases with the rotational speed of the blades, reduced propeller angular velocity offers the benefit of a quieter operation; however, the interaction between contra-rotating blades rows creates additional noise. Moreover, contra-rotating propellers are suitable for higher speeds, almost as fast as today's turbofan powered aircraft. The drawbacks associated with a pair of contra-rotating propellers are increased weight, complexity and cost. For example, one of the most compelling issue is related to the solution adopted to drive the large and slow moving propeller(s). Ref.[69] reports the two common solutions:

- To use a reduction gearbox driven by a high speed low pressure turbine. The gearbox is heavy and complex to build; so, unreliability and maintenance efforts are increased;
- To use directly a low speed, multi-stage, low pressure turbine which normally operates at faster speeds with respect to the propellers, but a compromise between fast and low rotational speeds has to be found [48].

1.2 CHALLENGES

In the seventies, the two oil crisis evidenced that aeronautical industries and airlines could be put at stake by oil providers. To face this issue, in 1975 the U.S. Senate directed NASA to looking for every potential fuel-saving concept for aircraft engines. The Advanced Turboprop project [30] led to the concept of Contra-Rotating Open Rotor (CROR). This CROR concept showed a potential for large fuel savings but led to significantly high noise emissions due to the absence of a screening duct. Because of the high noise emissions combined with the decrease of the price of the oil barrel in the late eighties, the contra-rotating open rotor never reached the commercial aviation. In our days, more than 50% of the operating costs of airlines is represented by fuel. In parallel, Airbus forecasts a doubled number of passengers by 2031 [2]. For such reasons, the European commission has established, through the Advisory Council for Aeronautics Research in Europe (ACARE), a set of demanding objectives to reduce emissions by 2050. Noise, CO_2 and NOx emissions should be reduced by 65%, 75% and 80%, respectively, with respect to their 2000s values. Therefore, to allow a sustainable air transportation, new concepts are needed for both engines and aircraft in general. Several of them are already feasible, among which: lightweight construction with advanced composite structure, airport collaborative decision making, with continuous climb departures and

less taxing stand by, aerodynamically optimized wing geometries, e.g. laminar wings, and fuel efficient engines, to name but a few. For the latter, two main types of engine are currently studied: the Ultra-High Bypass Ratio (UHBR) engine that is based on a larger fan exhaust engine, thus improving the propulsive efficiency, and the CROR engine, which relies on two rows of contra-rotating rotors and has already proved its viability within the framework of NASA Advanced Turboprop project [30]. Nevertheless, a lot of work has still to be done for the development of aircrafts mounting CROR engines. In fact, there are not only noise and aeroelastic issues, but also the integration with airframes, blades containments and other certification requirements need further developments. Possible configurations of future airplanes are reported in fig.(3). Whichever mounting configuration is selected, the significant weight and interference drag associated with large engine size will create installation challenges.

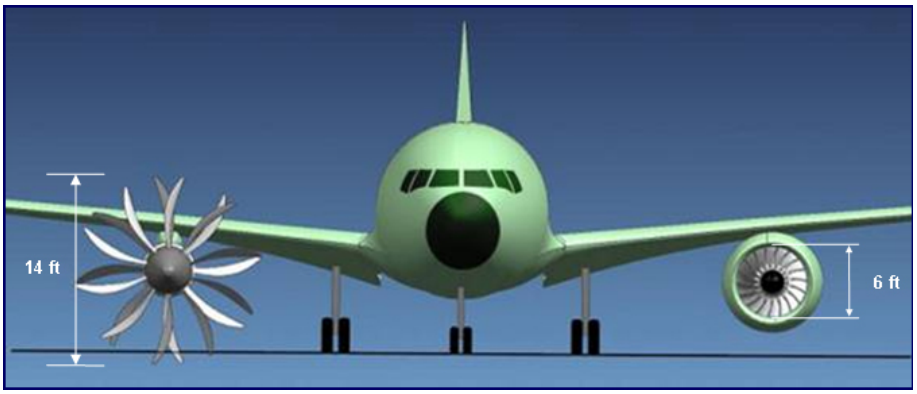

Figure 2: Problematic Airframe Installation. ®www.airinsight.com/

From the certification requirements point of view, designers must demonstrate that the probability of a blade failure is extremely low (in the order of a single failure per 1×10^8 flying hours). The propeller blades for the new open rotors will be highly optimized aerodynamically, lighter and less bulky than conventional propeller blades, thus making their design an extremely challenging task. There is also the requirement for aircraft manufacturers to ensure that aircraft systems (e.g. hydraulics systems) and passengers are sufficiently protected in the case of blade failure. Fulfilling this requirement may involve repositioning of certain aircraft systems or the use of shielding.

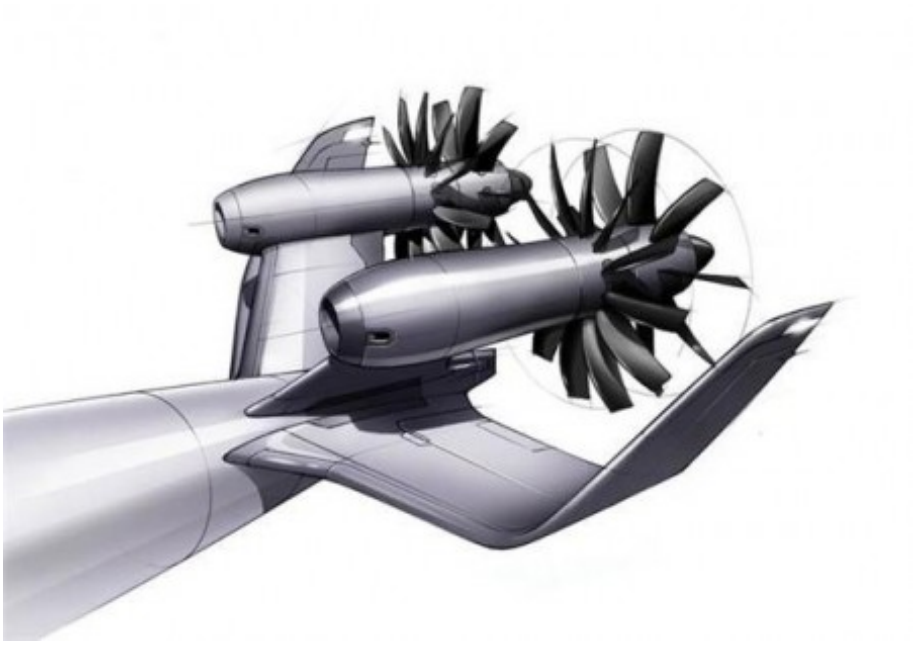

(a) ®www.falconairacademy.com/

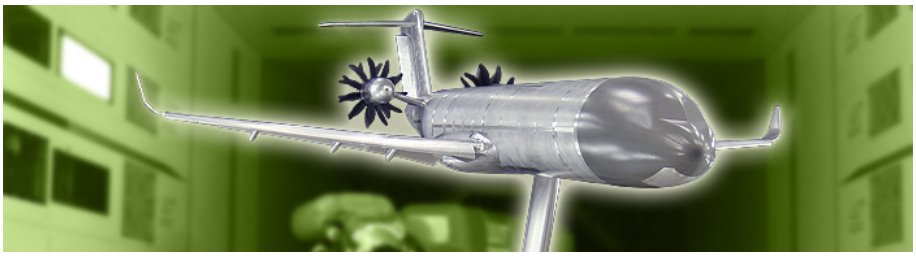

(b)

(c) ®www.styleofspeed.com

Figure 3: Compatible Aircraft Configurations for Integration with Airframes

1.3 PROPFAN RESEARCH AND DEVELOPMENT

The Advanced Turboprop project goals [30] were to show fuel and direct operating cost savings [48] over comparable turbofans and aircraft interior noise (and vibration) similar to that at turbofans, so to meet Federal Aviation Regulations [13, 43].

Figure 4: Experimental Setup of SR-5 propeller [30]

The first activity was the design of new propellers, knowing how sweep had been successful in reducing compressibility losses in wings, researchers designed blades with blade tips having 30° to 60° of sweep [4]. An added benefit of sweep was the potential decrease of the noise levels resulting from the high blade tip speed. The SR-1 propeller achieved a propulsion efficiency of 77% at Mach 0.8, quite close to the goal and without flutter instabilities. The changes in radial thickness distribution dictated by the structural and aeroelastic design plus the use of titanium instead of steel prevented flutter problems in the case of SR-1 blade. More blades models were produced in order to find the best solution for both structural and aerodynamic requirements, with the testing of SR-3, SR-5 and SR-7 designs [11, 17].

	SR-1	SR-2	SR-3	SR-5	SR-6
Tip sweep, degrees	30	0	45	60	40
Number of blades	8	8	8	10	10
Power loading	37.5	37.5	37.5	26	30
Tip speed, feet/second	800	800	800	600	700

Figure 5: Various Blade Model of [30]

A lot of aeroelastic analysis were conducted in order to develop programs that can achieve good correlations with experimental data [5, 7, 21]. The improvements were relevant and good accordances with experimental data were eventually achieved in [22] and [34] . Furthermore, a lot of experimental test were conducted with the purpose of building aircraft powered by propfan. The effort was relevant and several flight test were carried out [31, 41, 66]. In fig.(6) is represented the installation of Pratt & Whitney/Allison 578-DX engine onto the McDonnell Douglas MD-80.

Figure 6: Airframe Installation at Flight Test. ®www.airinsight.com

1.4 AEROELASTICITY IN OPEN ROTOR RESEARCH

Design studies on forced excitation, stall flutter and classical flutter were carried out and predicted the results reported in fig.(7). Forced excitations occur over the entire flight envelope and are caused by unsteady, unsymmetrical airflows produced by gusts, up-wash from the wing, and airframe-induced flow field distortions. It is observed that forced excitations peak is during flow-speed climb and high-speed cruise conditions. Stall flutter occurs primarily at low speed and re-

sults from blade separated flow. Classical flutter, a particular concern with propfans, happens at high speeds, beyond Mach 0.6. From the literature, no whirl flutter analysis has been carried out yet.

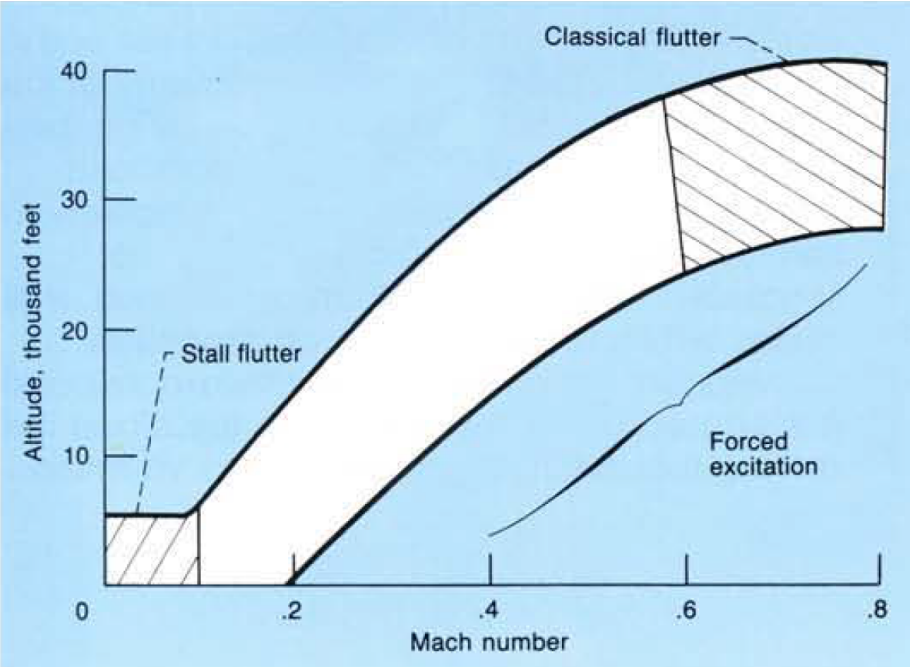

Figure 7: Flutter Boundaries - [30]

From the structural point of view, it has been shown the inadequacy of beam based approximations as a viable blade model at high sweeps and low aspect ratios [9]. The deficiency of the beam model is even more remarkable when blades are built with composite materials because the anisotropy behaviour cannot be modelled adequately. For more details, ref.[28] develops a rigorous formulation, providing some examples of anisotropic beam, e.g. helicopter rotor blade. So, shell or solid elements must be used to create a suitable high fidelity model for modal analysis. The results presented in [23], obtained with NASTRAN CQUAD4 shell elements, show a good agreement with experimental data. Besides, [74] presents a deep analysis on the effects of centrifugal and Coriolis forces onto the dynamic behaviour of rotating structures. For stationary analysis, *prestress stiffness* matrices, trimmed with centrifugal load, and *centrifugal stiffness* matrices have to be added to the classical linear stiffness matrix.

The aerodynamics can be modelled with various strategies. Ref.[52] compares the flow field obtained by experimental data (laser doppler velocimetry) with those obtained by subsonic lifting-line theory. The agreement is only qualitative and it can be inferred that more sophisticated models should been used. Because the similarities between propfan and turbomachinery, ref.[23] chooses an unsteady strip theory containing blade rows interactions (commonly treated with *travelling waves modes*). This modified strip theory (as explained in [51])

takes into account sweep effects. There is a good accordance with experimental data, so it can be roughly inferred that 3D effects are not so important in predicting flutter boundaries. Furthermore, the simple hypothesis of assuming a perfectly rigid disk with independent deformable blades is valid. Blades interact with each other mainly because of aerodynamic loads. When transonic regimes are reached, this modified theories cannot properly represent the aerodynamic flow field because of the non linearities introduced by shocks. Aerodynamic interactions among blades have to be correctly modelled, so recent researches prefer CFD analysis on the complete geometry instead of using 2D theories. Aeroacoustic interactions are also important factors to be accounted for the study of open rotors because they are the main cause of vibration and noise emission of this application. As it will be explained, there is only an aerodynamic coupling between the blades because, from the structural point of view, they are mostly independent bodies that vibrate onto a rigid hub. Nevertheless, an aeroacustic analysis and a prediction of acoustic vibratory loads are far away from the scope of this work, which is focused only on the flutter analysis of open rotors.

1.5 OVERVIEW OF THE THESIS

The aim of this thesis is two-fold. On one hand, it aims at showing the importance of classical flutter analysis within the aeroelastic design of open rotors and propfan. On the other hand, it tries to verify if a full potential (FP) method can be a simplified yet useful tool in predicting the aerodynamic behaviour of blades, even if Euler and Navier-Stokes solver are becoming more and more viable tools. It will be shown that an FP solver provides solutions very similar to Eulerian ones, even in presence of shocks on blades surface, better correlations being obtained if entropy corrections are inserted at transonic regimes. The time needed to perform flutter analysis is always smaller using an FP solver, so it can be a valid tool in the preliminary design at least.

The thesis is so organized:

Chapter 2. First, the rotating frame formulation of fluid dynamics explains how Eulerian or Navier-Stokes solvers can treat rotating problems. The common solution is to use a non-inertial reference frame so adding two source terms in the right hand side of the momentum equation (i.e. centrifugal and Coriolis forces). After that, the formulation of the two independent fields full potential solver is reported with particular focus onto boundary conditions and domain discretization.

Chapter 3. The theoretical background for solving structure subjected to rotating loads is recalled. The purpose of this chapter is

a better understanding of what common structural FEM solver (i.e. NASTRAN or ANSYS) do when simulating such a problem. Particular attention is given to the numerical implementation of the effects of inertia forces, i.e. the centrifugal and Coriolis loads. Eventually, the work-flow for solving the eigenvalues problem is presented in order to build a reduced order structural system.

Chapter 4. This chapter provides an overview of the background of the closed-loop interaction between the structural and the aerodynamic sub-system. The aeroelastic interface strategy is the core for connecting the aerodynamics to the structure. In particular, the employed technique for the fluid-structure coupling consists in an interpolation scheme based on Moving Least Squares. After that, the transpiration boundary condition, which is at the base of aeroelastic analyses, is explained. Eventually, the formulation for solving the aerodynamic flow field for both single and double stage open rotors is detailed.

Chapter 5. This chapter presents an overview of the flutter analysis methods in the frame of classical aeroelasticity. Primarily, the K-E and a root-tracking non-linear methods are used for computing the so-called $V-g$ and $V-\omega$ diagrams. Moreover, the identification of the aerodynamic transfer functions $\mathbf{H_{am}}(k, M_\infty)$ is described.

Chapter 6. In this chapter the results of the various analysis are reported. Various blade shapes are available from the literature and three different shape are investigated. Sec.(6.1) shows a correlation analysis between the full-potential solver and a uRANS solver of ref.[27]. A comparison with AeroX, an Euler solver developed at POLIMI, is always carried out to further validate the solutions obtained. In sec.(6.2) a test case for single stage open rotors is treated. These first two test cases are the background for the validation and verification of the various proposed methods for aeroelastic analyses in open rotors applications. Then, two other cases are investigated in sec.(6.3) and in sec.(6.4). The first one is the aeroelastic analysis of a single stage rotor, while the second one is the aeroelastic analysis of a contra-rotating open rotor (CROR).

2

AERODYNAMIC SUB-SYSTEM

This chapter is aimed at providing a theoretical background for the aerodynamic modelling that can be used for solving the flow field around rotating bodies. In sec.(2.1), the Euler equation of fluid dynamics are derived for a rotating reference frame. Then, sec.(2.2) shows the formulation of the full-potential method chosen for our aerodynamic analyses. Eventually, the last sections presents the various boundary conditions needed to correctly model the case of contra-rotating open rotor.

2.1 ROTATING FRAME FORMULATION OF FLUID DYNAMICS

When simulating fluid flows around aerodynamic bodies that operate under an imposed steady rotation - including turbomachinery, propeller, and rotor applications - it is useful to write the equation of motion in a rotating reference frame connected to the body [20, 35]. Therefore, if the rotating velocity is constant, the problem is steady in the non-inertial frame and a significant reduction of computation time can be achieved over the time required to solve the problem in the inertial|fixed frame, where a time dependent system must be solved. Using a non inertial frame implies the introduction of apparent forces in the momentum equation, i.e. the *centrifugal* and the *Coriolis* forces. They act as source terms and can be simply added to the right hand side of the equations without any complications. In the inertial frame, there is a different view of the problem. The fluid is at rest and the grid, i.e. the aerodynamic body, moves with its own velocity. Obviously, apparent forces must not be included in the equations. The drawback of using such a formulation is that Euler|Navider-Stokes equations are not invariant with respect arbitrary rigid motions, e.g. rotations. In particular, the components of the velocity vector, $\mathbf{u} = \{u, v, w\}^T$, depend on the reference system chosen.

In the followings, the assumption of a constant angular velocity $\mathbf{\Omega}$ is considered. An interested reader could look at [40] where a more general treatment of non-inertial frames is given, albeit only 2D applications being reported.

2.1.1 Euler Equations for Rotating Flows

In the non inertial frame, the equations can be obtained in term of the absolute velocity (velocity relative to the inertial frame) or the velocity relative to the non-inertial frame. In the same way [10], let $\mathbf{u_r}$ be the fluid velocity relative to the rotating frame and $\mathbf{u}$ be the absolute velocity. The relationship between $\mathbf{u_r}$ and $\mathbf{u}$ is

$$\mathbf{u} = \mathbf{u_r} + \boldsymbol{\Omega} \times \mathbf{R}, \tag{2.1}$$

where $\mathbf{R}$ is the distance from the axis of rotation. The unsteady compressible Euler equations for the relative velocity in a frame rotating with constant angular speed, in absence of external volume force or heat addition, are given by (e.g. [33] or [57])

$$\begin{aligned} &\frac{\partial \rho}{\partial t} + \nabla \cdot [\rho \mathbf{u_r}] = 0, \\ &\frac{\partial (\rho \mathbf{u_r})}{\partial t} + \nabla \cdot [\rho \mathbf{u_r} \otimes \mathbf{u_r} + p\mathbf{I}] = -2\rho(\boldsymbol{\Omega} \times \mathbf{u_r}) - \rho \boldsymbol{\Omega} \times (\boldsymbol{\Omega} \times \mathbf{R}), \end{aligned} \tag{2.2}$$

$$\frac{\partial E_r}{\partial t} + \nabla \cdot [\mathbf{u_r}(E_r + p) + k\nabla T] = 0, \tag{2.3}$$

with:

$$\begin{aligned} E_r &= \frac{p}{\gamma - 1} + \frac{1}{2}\rho |\mathbf{u_r}|^2 - \frac{1}{2}\rho |(\boldsymbol{\Omega} \times \mathbf{R})|^2 \\ &= E - \rho \mathbf{u_r} \cdot (\boldsymbol{\Omega} \times \mathbf{R}), \end{aligned} \tag{2.4}$$

being the total energy per unit volume in the rotating frame. These are the conservation laws seen by an observer in the rotating frame, and $\mathbf{u_r}$ is the velocity field relative to the rotating frame. It is clear that, from the numerical point of view, the mesh is fixed in time and space, while the fluid motion can be divided into a "rigid" motion (i.e. rotational) and a perturbation motion due to the interaction with aerodynamic bodies.

An alternative form of eqs.(2.2) is obtained by substituting the expression for $\mathbf{u_r}$ from eq.(2.1) into eqs.(2.2). After remembering the identities:

$$\nabla \cdot (\vec{a} \otimes \vec{b}) = \vec{b}(\nabla \cdot \vec{a}) + (\vec{a} \cdot \nabla)\vec{b},$$

$$\nabla \times (\vec{F} \times \vec{G}) = \vec{F}(\nabla \cdot \vec{G}) - \vec{G}(\nabla \cdot \vec{F}) - (\vec{F} \cdot \nabla)\vec{G} + (\vec{G} \cdot \nabla)\vec{F}, \tag{2.5}$$

$$\nabla \cdot (\boldsymbol{\Omega} \times \mathbf{R}) = 0, \tag{2.6}$$

$$\nabla(\boldsymbol{\Omega} \times \mathbf{R}) = -\boldsymbol{\Omega}_\times = -\begin{bmatrix} 0 & -\Omega_3 & \Omega_2 \\ \Omega_3 & 0 & -\Omega_1 \\ -\Omega_2 & \Omega_1 & 0 \end{bmatrix},$$

the mass conservation with the absolute velocity $\mathbf{u}$ becomes,

$$\frac{\partial \rho}{\partial t} + \nabla \cdot [\rho(\mathbf{u} - \boldsymbol{\Omega} \times \mathbf{R})] = 0. \tag{2.7}$$

Developing the momentum equation,

$$\frac{\partial(\rho \mathbf{u_r})}{\partial t} + \nabla \cdot [\rho \mathbf{u_r} \otimes \mathbf{u_r} + p\mathbf{I}] = -2\rho(\boldsymbol{\Omega} \times \mathbf{u_r}) - \rho\boldsymbol{\Omega} \times (\boldsymbol{\Omega} \times \mathbf{R}),$$
$$\frac{\partial(\rho \mathbf{u})}{\partial t} - \frac{\partial \rho}{\partial t}(\boldsymbol{\Omega} \times \mathbf{R}) + \mathbf{u_r}\nabla \cdot (\rho \mathbf{u_r}) + (\rho \mathbf{u_r} \cdot \nabla)\mathbf{u_r} + \nabla p = -2\rho(\boldsymbol{\Omega} \times \mathbf{u_r}) - \rho\boldsymbol{\Omega} \times (\boldsymbol{\Omega} \times \mathbf{R}),$$
$$\frac{\partial(\rho \mathbf{u})}{\partial t} - (\boldsymbol{\Omega} \times \mathbf{R})\nabla \cdot (\rho \mathbf{u_r}) + \mathbf{u_r}\nabla \cdot (\rho \mathbf{u_r}) + (\rho \mathbf{u_r} \cdot \nabla)\mathbf{u_r} + \nabla p = -2\rho(\boldsymbol{\Omega} \times \mathbf{u_r}) - \rho\boldsymbol{\Omega} \times (\boldsymbol{\Omega} \times \mathbf{R}),$$
$$\frac{\partial(\rho \mathbf{u})}{\partial t} - (\mathbf{u_r} + \boldsymbol{\Omega} \times \mathbf{R})\nabla \cdot (\rho \mathbf{u_r}) + (\rho \mathbf{u_r} \cdot \nabla)\mathbf{u_r} + \nabla p = -2\rho(\boldsymbol{\Omega} \times \mathbf{u_r}) - \rho\boldsymbol{\Omega} \times (\boldsymbol{\Omega} \times \mathbf{R}),$$
$$\frac{\partial(\rho \mathbf{u})}{\partial t} - \mathbf{u}\nabla \cdot (\rho \mathbf{u_r}) + (\rho \mathbf{u_r} \cdot \nabla)\mathbf{u_r} + \nabla p = -\rho(\boldsymbol{\Omega} \times \mathbf{u_r}) + \nabla(\boldsymbol{\Omega} \times \mathbf{R})\rho \mathbf{u_r} - \rho\boldsymbol{\Omega} \times (\boldsymbol{\Omega} \times \mathbf{R}),$$
$$\frac{\partial(\rho \mathbf{u})}{\partial t} - \mathbf{u}\nabla \cdot (\rho \mathbf{u_r}) + (\rho \mathbf{u_r} \cdot \nabla)\mathbf{u_r} + \nabla p = -\rho(\boldsymbol{\Omega} \times \mathbf{u_r}) + \nabla(\boldsymbol{\Omega} \times \mathbf{R})\rho \mathbf{u_r} - \rho\boldsymbol{\Omega} \times (\boldsymbol{\Omega} \times \mathbf{R}),$$
$$\frac{\partial(\rho \mathbf{u})}{\partial t} - \mathbf{u}\nabla \cdot (\rho \mathbf{u_r}) + (\rho \mathbf{u_r} \cdot \nabla)\mathbf{u} + (\rho \mathbf{u_r} \cdot \nabla)\boldsymbol{\Omega} \times \mathbf{R} + \nabla p = -\rho\boldsymbol{\Omega} \times \mathbf{u} - \rho\boldsymbol{\Omega} \times \mathbf{u_r},$$
$$\frac{\partial(\rho \mathbf{u})}{\partial t} - \nabla \cdot (\rho \mathbf{u_r} \otimes \mathbf{u}) - \rho\boldsymbol{\Omega} \times \mathbf{u_r} + \nabla p = -\rho\boldsymbol{\Omega} \times \mathbf{u} - \rho\boldsymbol{\Omega} \times \mathbf{u_r},$$

we obtain:

$$\frac{\partial(\rho \mathbf{u})}{\partial t} - \nabla \cdot (\rho \mathbf{u_r} \otimes \mathbf{u}) + \nabla p = -\rho\boldsymbol{\Omega} \times \mathbf{u}. \tag{2.8}$$

Finally, the energy equation:

$$\frac{\partial E_r}{\partial t} + \nabla \cdot [\mathbf{u_r}(E_r + p) + k\nabla T] = 0,$$
$$\frac{\partial E}{\partial t} - \frac{\partial(\rho \mathbf{u_r})}{\partial t} \cdot (\boldsymbol{\Omega} \times \mathbf{R}) + \nabla \cdot [\mathbf{u_r}(E - \rho \mathbf{u_r} \cdot (\boldsymbol{\Omega} \times \mathbf{R}) + p) + k\nabla T] = 0,$$
$$\frac{\partial E}{\partial t} - \frac{\partial(\rho \mathbf{u_r})}{\partial t} \cdot (\boldsymbol{\Omega} \times \mathbf{R})$$
$$+ \nabla \cdot [\mathbf{u_r}(E + p) + k\nabla T] - \nabla \cdot [\mathbf{u_r}(\rho \mathbf{u_r} \cdot (\boldsymbol{\Omega} \times \mathbf{R}))] = 0. \tag{2.9}$$

Multiplying the momentum equation 2.8 by $(\boldsymbol{\Omega} \times \mathbf{R})$ and substituting it into eq.(2.9), the energy equation becomes:

$$\frac{\partial E}{\partial t} + \nabla \cdot [(\mathbf{u} - \boldsymbol{\Omega} \times \mathbf{R})(E + p) + (\boldsymbol{\Omega} \times \mathbf{R})p + k\nabla T] = 0.$$

The governing equations, in terms of absolute velocity, in a rotating reference frame with constant angular velocity are:

$$\begin{aligned}
&\frac{\partial \rho}{\partial t} + \nabla \cdot [\rho(\mathbf{u} - \boldsymbol{\Omega} \times \mathbf{R})] = 0,\\
&\frac{\partial(\rho \mathbf{u})}{\partial t} - \nabla \cdot (\rho \mathbf{u_r} \otimes \mathbf{u}) + \nabla p = -\rho\boldsymbol{\Omega} \times \mathbf{u},\\
&\frac{\partial E}{\partial t} + \nabla \cdot [(\mathbf{u} - \boldsymbol{\Omega} \times \mathbf{R})(E + p) + (\boldsymbol{\Omega} \times \mathbf{R})p + k\nabla T] = 0.
\end{aligned} \tag{2.10}$$

Ref.[1] states that using absolute-velocity formulation allows for a more accurate evaluation of the fluxes in a finite-volume scheme. Using eqs.(2.10) for the absolute velocity requires no modification in the flow solver to either the far field reference state or the relation between conserved energy and pressure. Just a few simple modifications of the

code have to be made to solve problem with rotating bodies. Therefore, a single initial evaluation of $\boldsymbol{\Omega} \times \mathbf{R}$ throughout the field has to be carried out, without having to recompute face speeds and grid normals or volumes at each time step, as required in the moving-grid formulation. However, since the source terms are functions of the velocity field, they must be evaluated at each time step. Hence, using a non-inertial reference frame is the same as solving either Euler or Navier-Stokes for rotating applications.

It should be noted that within the assumptions of the specific non-inertial frame considered here (pure rotation with constant $\boldsymbol{\Omega}$), the far field conditions are not completely arbitrary. For example, consider a typical situation in which the absolute velocity at the far field is constant, $\mathbf{V}_\infty$, with corresponding constant condition ρ_∞ and p_∞. In that case, the continuity and energy equations are satisfied identically at the far field, but the momentum equation implies:

$$\boldsymbol{\Omega} \times \mathbf{V}_\infty = 0, \tag{2.11}$$

which requires that either

1. $\mathbf{V}_\infty = 0$;
2. $\mathbf{V}_\infty$ parallel to $\boldsymbol{\Omega}$.

In terms of an application scenario, if a helicopter blade rotates about (say) the vertical axis, then the non-inertial formulation above is only applicable for the hover (condition 1) and vertical flight (condition 2). The open rotor application studied in this work perfectly match the second case described, the translational motion, described by $\mathbf{V}_\infty$, being assumed to be perfectly aligned with the rotational velocity, $\boldsymbol{\Omega}$. This peculiarity is also useful to simplify the domain grid using **periodic boundary conditions** as explained in sec.(2.5).

2.1.2 Bernoulli Theorem for Rotating Flows

It can be demonstrated that the Bernoulli theorem cannot be formulated in a rotating reference frame. The assumption for using a non-inertial frame is that the grid|body is at rest, while the fluid velocity is the sum of a perturbed and rotational velocity, $\mathbf{u_r} + \boldsymbol{\Omega} \times \mathbf{R}$. The demonstration can start from either eq.(2.2) or eq.(2.10).

Beginning from the momentum equation with relative velocity, eq.(2.2),

$$\frac{\partial(\rho \mathbf{u_r})}{\partial t} + \nabla \cdot [\rho \mathbf{u_r} \otimes \mathbf{u_r} + p\mathbf{I}] = -2\rho(\boldsymbol{\Omega} \times \mathbf{u_r}) - \rho\boldsymbol{\Omega} \times (\boldsymbol{\Omega} \times \mathbf{R}),$$
$$\rho \frac{\partial \mathbf{u_r}}{\partial t} + (\rho \mathbf{u_r} \cdot \nabla)\mathbf{u_r} + \nabla p = -2\rho(\boldsymbol{\Omega} \times \mathbf{u_r}) - \rho\boldsymbol{\Omega} \times (\boldsymbol{\Omega} \times \mathbf{R}),$$

using the second identity of eq.(2.5) and defining the local vorticity, $\boldsymbol{\omega} = \nabla \times \mathbf{u_r}$, one obtains

$$\frac{\partial \mathbf{u_r}}{\partial t} + \frac{1}{2}\nabla(\mathbf{u_r} \cdot \mathbf{u_r}) + \frac{\nabla p}{\rho} = \mathbf{u_r} \times (\boldsymbol{\omega} + 2\boldsymbol{\Omega}) + \frac{1}{2}\nabla(\|\boldsymbol{\Omega} \times \mathbf{R}\|^2), \quad (2.12)$$

$$(2.13)$$

where the centrifugal force, $\boldsymbol{\Omega} \times (\boldsymbol{\Omega} \times \mathbf{R})$, can be rewritten as a centrifugal potential,

$$\boldsymbol{\Omega} \times (\boldsymbol{\Omega} \times \mathbf{R}) = -\frac{1}{2}\nabla(\|\boldsymbol{\Omega} \times \mathbf{R}\|^2). \quad (2.14)$$

With the hypothesis of $\mathbf{u_r} = \nabla\phi$ and of isentropic flow regime, $\nabla s = 0$, the above equation becomes

$$\nabla\left[\frac{\partial \phi}{\partial t} + \frac{1}{2}\|\nabla\phi\|^2 + h - \frac{1}{2}\nabla(\|\boldsymbol{\Omega} \times \mathbf{R}\|^2)\right] = \mathbf{u_r} \times (\boldsymbol{\omega} + 2\boldsymbol{\Omega}). \quad (2.15)$$

We can observe that the right hand side of the above equation is not zero as it is in the classical inertial formulation. There is not a closed loop where the quantity in the square bracket is conserved. In other words, the Bernoulli theorem cannot be expressed as a difference between its local and asymptotic values. Hence, the Bernoulli theorem cannot be expressed in a non-inertial reference frame.

The same result can be obtained by starting from the momentum equation in absolute velocity, eq.(2.10). In fact, using another vectorial identity,

$$\begin{aligned}\nabla \times (\boldsymbol{\Omega} \times \mathbf{R}) &= \boldsymbol{\Omega}(\nabla \cdot \mathbf{R}) - \cancelto{0}{\mathbf{R}(\nabla \cdot \boldsymbol{\Omega})} - (\boldsymbol{\Omega} \cdot \nabla)\mathbf{R} + \cancelto{0}{(\mathbf{R} \cdot \nabla)\boldsymbol{\Omega}} \\ &= 2\boldsymbol{\Omega} \neq 0,\end{aligned}$$

it is impossible to state $\mathbf{u} = \mathbf{u_r} + \boldsymbol{\Omega} \times \mathbf{R} = \nabla\Phi$ because the term, $\boldsymbol{\Omega} \times \mathbf{R}$, is rotational and so the fluid velocity cannot be described as gradient of a potential quantity.

From this analysis, it is shown that the Bernoulli theorem can be written only in an inertial reference frame. If a rotational motion with constant angular velocity has to be described, the Arbitrary Lagrangian Eulerian (ALE) formulation can be used [18]. Hence, the fluid is at rest and the grid moves with a arbitrary velocity, $\mathbf{V_G}$. It can be observed that the grid velocity $\mathbf{V_G}$ can be a combination of rotating and translating motion. In this way, the Bernoulli theorem is the usual

$$\frac{\partial \phi}{\partial t} + \frac{1}{2}|\nabla\phi|^2 + \frac{c_\infty^2}{\gamma - 1}\left(\left(\frac{\rho}{\rho_\infty}\right)^{\gamma-1} - 1\right) = 0, \quad (2.16)$$

where ϕ is the perturbed potential, $\nabla\phi = \mathbf{u_r}$. It is remarked that the potential ϕ is a variable attached to the moving grid. The perturbed velocity is calculated at each point of the mesh that moves with the arbitrary velocity $\mathbf{V_G}$. Eq.(2.16) can be restated in a more compact way

$$\frac{\partial \phi}{\partial t} + H - H_\infty = 0, \quad (2.17)$$

where H_∞ is the total specific enthalpy at the far field (at which $\nabla\phi$ is null because there is no perturbation motion). Now, the total time derivative is introduced

$$\frac{d*}{dt} = \frac{\partial *}{\partial t} + \mathbf{V}_G \cdot \nabla *, \tag{2.18}$$

where the transport term is related only to the moving grid, because there are no relative motions between the velocity potential ϕ and the computational mesh. In other words, the potential ϕ is attached to the moving grid. It can also be observed that the fluid density ρ and the potential ϕ are invariants for any rigid motion, so there is no need to recompute faces speeds, grid normals, volumes or grid coordinates at each time step (if mesh deformations are not included). In the next section, the formulation of the full potential solver used in this work is presented [53–55].

2.2 NON ISENTROPIC POTENTIAL ALE FLOW FORMULATION

2.2.1 Compressible Potential Flow Model

The aim is to model attached flows past aerodynamic bodies at high Reynolds numbers. These circumstances ensure thin boundary layer and narrow vortical regions. So the mathematical description of a flow system is obtained with the approximation of a non-viscous, irrotational flow. Thus, the condition of zero vorticity,

$$\boldsymbol{\omega}(\mathbf{x}, t) = \nabla \times \mathbf{V}(\mathbf{x}, t) = 0, \tag{2.19}$$

will be automatically satisfied if the three-dimensional velocity field can be described by a discontinuous scalar potential function ϕ, defined as,

$$\mathbf{V}(\mathbf{x}, t) = \nabla\phi(\mathbf{x}, t), \tag{2.20}$$

where the vorticity bounded to lines|surfaces is related to the jump of ϕ across them. This is the so-called quasi-potential flow [49]. Assuming the viscous stress and the heat sources to be negligible, the governing equations of the flow are [33]:

- The continuity equation,

$$\frac{\partial \rho}{\partial t} + \nabla \cdot (\rho \nabla \phi) = 0, \tag{2.21}$$

- The Bernoulli theorem,

$$\frac{\partial \phi}{\partial t} + H - H_\infty = 0. \tag{2.22}$$

Both the potential function ϕ and the density function ρ can be defined on a reference domain R_G moving according to an absolute velocity field $\boldsymbol{V}_G$ on a spatial domain R_g. Both these functions depends on the spatial position $\boldsymbol{x}$ and time. Hereafter, the dependencies $(\boldsymbol{x}, t)$ will be omitted to ease the reading.

Let us define the integral form of the continuity equation, *i.e.* eq.(2.21), in the fixed spatial domain R_g:

$$\int_{\mathcal{V}} \frac{\partial \rho}{\partial t} d\mathcal{V} + \int_{\mathcal{V}} \nabla \cdot (\rho \nabla \phi)\, d\mathcal{V} = 0. \tag{2.23}$$

As described in [18], we define the time derivative over moving volumes (respect to R_G) as:

$$\frac{d*}{dt} = \frac{\partial *}{\partial t} + \boldsymbol{V}_G \cdot \nabla *, \tag{2.24}$$

and appliyng the divergence theorem the continuity equation, eq.(2.23), becomes:

$$\int_{\mathcal{V}} \left(\frac{d\rho}{dt} - \boldsymbol{V}_G \cdot \nabla \rho \right) d\mathcal{V} + \int_{\Gamma} \rho \boldsymbol{V} \cdot \boldsymbol{n} d\gamma = 0, \tag{2.25}$$

which represents the proposed ALE formulation of [54].

We can go on with this demonstration in order to arrive at the usual ALE formulation that can be found in [18]. Recalling that [1] [33],

$$\frac{d(d\mathcal{V})}{dt} = \nabla \cdot \boldsymbol{V}_g \, d\mathcal{V}, \tag{2.26}$$

where $\boldsymbol{V}_G$ is the transport velocity of the elementary volume being followed; the time derivative of the generic mass element becomes:

$$\frac{d(\rho d\mathcal{V})}{dt} = \frac{d\rho}{dt} d\mathcal{V} + \rho \nabla \cdot \boldsymbol{V}_g \, d\mathcal{V}. \tag{2.27}$$

Using it in conbination with eq.(2.25), we obtain:

$$\begin{aligned} \int_{\mathcal{V}} \frac{d(\rho d\mathcal{V})}{dt} d\mathcal{V} - \int_{\mathcal{V}} \rho \nabla \cdot \boldsymbol{V}_G \, d\mathcal{V} - \int_{\mathcal{V}} \boldsymbol{V}_G \cdot \nabla \rho d\mathcal{V} + \int_{\Gamma} \rho \boldsymbol{V} \cdot \boldsymbol{n} d\gamma = \\ \frac{d}{dt} \int_{\mathcal{V}} \rho d\mathcal{V} - \int_{\mathcal{V}} \nabla \cdot (\rho \boldsymbol{V}_G)\, d\mathcal{V} + \int_{\Gamma} \rho \boldsymbol{V} \cdot \boldsymbol{n} d\gamma = 0, \end{aligned} \tag{2.28}$$

So, the usual ALE formulation is obtained,

$$\frac{d}{dt} \int_{\mathcal{V}} \rho d\mathcal{V} - \int_{\Gamma} \rho \left(\boldsymbol{V} - \boldsymbol{V}_G \right) \cdot \boldsymbol{n} d\gamma = 0. \tag{2.29}$$

The proposed ALE formulation, which leads to eq.(2.25), is indipendent from the time derivative of the control volume. The time derivative appears outside the integral operator in the usual ALE formulation, eq.(2.29), while remains inside in eq.(2.25). The drawback of the

1 In Cartesian coordinates: $d\mathcal{V} = dxdydz$ and $\boldsymbol{V} = \{V_x, V_y, V_z\}^T$; so $\frac{d(d\mathcal{V})}{dt} = \frac{d(dx)}{dt} dydz + dx \frac{d(dy)}{dt} dz + dxdy \frac{d(dz)}{dt} = \left(\frac{\partial V_x}{\partial x} + \frac{\partial V_y}{\partial y} + \frac{\partial V_z}{\partial z} \right) dxdydz = \nabla \cdot \boldsymbol{V}_g \, d\mathcal{V}$

proposed ALE formulation is the evaluation of the term $\nabla\rho$, which is not present in the usual ALE one.

The Bernoulli theorem, eq.(2.22), in the space domain R_g is:

$$\frac{\partial\phi}{\partial t}+\frac{1}{2}|\nabla\phi|^2+\frac{c_\infty^2}{\gamma-1}\left(\left(\frac{\rho}{\rho_\infty}\right)^{\gamma-1}-1\right)=0. \tag{2.30}$$

Applying the total time derivative, eq.(2.24), to the potential function the ALE form,

$$\frac{d\phi}{dt}-\nabla\phi\cdot\boldsymbol{V}_G+\frac{1}{2}|\nabla\phi|^2+\frac{c_\infty^2}{\gamma-1}\left(\left(\frac{\rho}{\rho_\infty}\right)^{\gamma-1}-1\right)=0. \tag{2.31}$$

The related integral form,

$$\int_{\mathcal{V}}\left(\frac{d\phi}{dt}-\nabla\phi\cdot\boldsymbol{V}_G+H-H_\infty\right)d\mathcal{V}=0, \tag{2.32}$$

is obtained, in which the convected reference frame is treated as for eq.(2.25). Using the time derivative of the elementary mass, eq.(2.27), the usual integral ALE form can be obtained,

$$\frac{d}{dt}\int_{\mathcal{V}}\phi d\mathcal{V}+\int_{\mathcal{V}}(H-H_\infty)\,d\mathcal{V}-\int_{\mathcal{V}}\nabla\cdot(\phi\boldsymbol{V}_G)\,d\mathcal{V}=0, \tag{2.33}$$

which is somewhat akin to eq.(2.29), even if it is not a balance equation.

Remark. Here, the ALE formulation proposed in [54] will be preferred because it provides the same scheme for accounting for a moving grid R_G and because it frees from any limitation imposed onto the mesh motion to satisfy the Geometric Conservation Law (GCL) [29]. So, in order to avoid any numerical complication related to the domain motion, the ALE formulation will be based on the form of eq.(2.25) and eq.(2.32).

2.2.2 Entropy Correction and Wake Equations

Starting from the ALE forms of the continuity equation, eq.(2.25), and Bernoulli theorem, eq.(2.32), an entropy correction model is now reported, as fully described in ref.[53]. The potential formulation does not admit non-homoentropic conditions. First, according to Crocco's theorem,

$$T\nabla s=\nabla H+\boldsymbol{\omega}\times\boldsymbol{V}, \tag{2.34}$$

where T is the temperature and H is the total enthalpy, an entropy gradient implies vorticity in the motion field and so prevents the existence of a velocity potential. In presence of discontinuities such as shock waves the Rankine-Hugoniot relations lead to an entropy increase through a shock. If the shock intensity is uniform, then the entropy will remain uniform downstream of the shock, but with a

value differing from its initial constant value. In this case, according to eq.(2.34), the flow remains irrotational. However, if the shock intensity is not constant, which is most likely to occur in practice, for curved shocks for instance, then eq.(2.34) shows that the flow is not irrotational any more and hence the mere existence of a potential downstream of the discontinuity cannot be justified rigorously. Therefore, the potential flow model in presence of shock discontinuities cannot be made fully compatible with the system of Euler equations, since the potential model implies constant entropy and has therefore no mechanisms to generate entropy variations across discontinuities. Moreover, the terms related to the entropy gradient and to the vorticity, which appear in the momentum equation, are not state functions and so they cannot be easily integrated through a generic path to obtain a scalar equation, i.e. they require a "special" Bernoulli theorem. To tackle such a problem, the motion field can be divided in two regions fig.(8): a layer covering the body-wake surface, in which the flow can be non-homoentropic, and a potential region which embeds the layer.

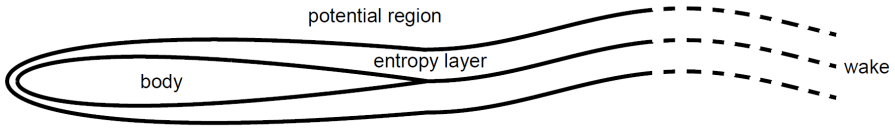

Figure 8: Domain Decomposition.

According to the above remarks, the Bernoulli theorem, eq.(2.22), is strictly applicable only in the potential region. However, for relatively thin entropy layers, the velocity potential can be used for the whole domain and the entropy gradient that appears in the momentum equation can be neglected. These assumptions lead to a non-isentropic approximation of the Bernoulli theorem,

$$\frac{d\phi}{dt} - \nabla\phi \cdot \boldsymbol{V}_G + \frac{1}{2}|\nabla\phi|^2 + \frac{c_\infty^2}{\gamma - 1}\left(\frac{K}{K_\infty}\left(\frac{\rho}{\rho_\infty}\right)^{\gamma-1} - 1\right) = 0, \quad (2.35)$$

where, thanks to thermodynamics, we have

$$K = \frac{p}{\rho^\gamma} = e^{s/c_v} = p_0^{1-\gamma}. \quad (2.36)$$

Then, the related ALE entropy transport equation is:

$$\frac{dK}{dt} - \boldsymbol{V}_G \cdot \nabla K + \nabla\phi \cdot \nabla K = 0, \quad (2.37)$$

which must be applied also within the entropy layer. Eq.(2.37) allows to convect the entropy produced by attached upstream shocks, so that the wake becomes also a discontinuity for the entropy function.

In order to freely satisfy the mass conservation across the wake, the pressure continuity between the lower (l) and the upper (u) side of this line | surface must be imposed,

$$\Delta\left(K\rho^{\gamma}\right) = 0, \tag{2.38}$$

where $\Delta* = *_u - *_l$ is the jump operator across the wake. Writing the above modified Bernoulli theorem, eq.(2.35), across the wake, the desired non-isentropic ALE wake equation is obtained:

$$\frac{d\Delta\phi}{dt} - \nabla\left(\Delta\phi\right)\cdot\boldsymbol{V}_G + \frac{1}{2}\Delta|\nabla\phi|^2 + \frac{c_\infty^2}{(\gamma-1)K_\infty\rho_\infty^{\gamma-1}}\Delta\left(K\rho^{\gamma-1}\right) = 0. \tag{2.39}$$

Eqs.(2.21),(2.35),(2.37),(2.38) and (2.39) do not imply dissipative phenomena, so, when a shock occurs, an entropy jump related to the shock strenght must be introduced in the entropy layer using an approximation of the Rankine-Hugoniot (R-H) relation [53].

All the above equations are then adimensionalized with respect to asymptotic values: $\rho_\infty, V_\infty \text{ and } K_\infty$, while keeping lengths as dimensional quantities. So, denoting the dimensional quantities with suffix d, we define the following non-dimensional terms: $\rho = \rho_d/\rho_\infty, \varphi = \phi_d/V_\infty, k = K_d/K_\infty, t = V_\infty t_d, \boldsymbol{V}_G = \boldsymbol{V}_{G\,d}/V_\infty$. Then eqs.(2.25),(2.35), (2.37),(2.38) and (2.39) become:

$$\frac{d\rho}{dt} - \boldsymbol{V}_G\cdot\nabla\rho + \nabla\cdot(\rho\nabla\varphi) = 0, \tag{2.40}$$

$$\frac{d\varphi}{dt} - \nabla\varphi\cdot\boldsymbol{V}_G + \frac{1}{2}|\nabla\varphi|^2 + \frac{M_\infty^{-2}}{\gamma-1}\left(k\rho^{\gamma-1}-1\right) = 0, \tag{2.41}$$

$$\frac{dk}{dt} - \boldsymbol{V}_G\cdot\nabla k + \nabla\varphi\cdot\nabla k = 0, \tag{2.42}$$

$$\Delta\left(k\rho^{\gamma}\right) = 0, \tag{2.43}$$

$$\frac{d\Delta\varphi}{dt} - \nabla\left(\Delta\varphi\right)\cdot\boldsymbol{V}_G + \frac{1}{2}\Delta|\nabla\varphi|^2 + \frac{M_\infty^{-2}}{\gamma-1}\Delta\left(k\rho^{\gamma-1}\right) = 0, \tag{2.44}$$

with $M = M_\infty|\nabla\varphi|/\sqrt{k\rho^{\gamma-1}}$ and $C_p = 2(k\rho^{\gamma}-1)/(\gamma M_\infty^2)$. The scalar equations (2.40), (2.41) and (2.42), the wake conditions, eqs.(2.43) and (2.44), and the shock condition (Rankine Hugoniot) combined with a shock velocity estimation in the independent unknowns ρ, φ and k, constitute the FP model.

Remark. the most common strategy adopted so far to solve potential flows is to evaluate the density using Bernoulli equation (2.22),

$$\rho = \left[1 - \frac{\gamma-1}{2}M_\infty^2\left(2\frac{d\varphi}{dt} + |\nabla\varphi|^2 - 1\right)\right]^{\frac{1}{\gamma-1}}, \tag{2.45}$$

and then to substitute it in the mass conservation, eq.(2.21). This results in a conservative second-order differential equation in the unknown φ only. With a mechanical analogy φ can be identified as

a degree of freedom function while the pair ρ-φ can be interpreted as state functions. So the two-fields approach corresponds to formulating the problem directly in state space form. As hinted at already, the use of two independent approximations for ρ and φ to solve eqs.(2.21) and (2.22) was likely first proposed by Chipman [16] for unsteady, non lifting, structured 2D profiles. Nonetheless, such a formulation seems to have been little used, till the recent appearance of the unsteady, unstructured finite volume implementations of [**parinello2010independent**, 53, 65]. The two-field approach considerably simplifies the development of a numerical approximation, leading to a robust resolution scheme. It is also fundamental for an easy application of the entropy layer based FP model just presented, making it closer to the physics of the problem, for both steady and unsteady flows. The entropy production alters the momentum equation, leading to a non isentropic Bernoulli equation, eq.(2.41), and consequently to a non isentropic wake condition, eq.(2.44), while preserving mass conservation, eq.(2.40). Moreover, the two-field approach simplifies the development of the numerical upwinding, needed to stabilize solution with shocks.

2.3 EXTERNAL BOUNDARY CONDITIONS

In aircraft application, there are mainly *external problems*. Such problems are analytically defined over an unbounded domain. In view of a numerical solution, an external fictitious boundary must be applied to the domain, so making viable numerical solutions related to some kind of "numerical wind tunnel". This new boundary needs special conditions to grant the proper influence of the asymptotic conditions. A non reflecting boundary is realized by mean of characteristic variables [61]. For hyperbolic equations, like those of an unsteady potential flow, the number of physical variables that can be imposed on the external far-field boundary is related to the propagation properties of the system perturbations. The characteristic theory [33] states that the number of boundary conditions must be equal to the number of the characteristic variables related to the incoming waves. These conditions can prevent the reflection of the internal waves on the external boundary. The mono-dimensional non-reflecting condition is given by:

$$w_i = (w_i)_\infty, \tag{2.46}$$

where w_i are the characteristic variables related to the incoming waves and ∞ identifies their asymptotic value. Subsonic asymptotic conditions involve just one incoming characteristic and just one boundary condition. The characteristic variables for monodimensional potential equations are the so-called *Riemann invariants* [33]:

$$w = u \pm \frac{2c}{\gamma - 1}, \tag{2.47}$$

where c is the speed of sound which can be expressed through the Bernoulli theorem:

$$\frac{c}{c_\infty} = \sqrt{1 - \frac{\gamma-1}{c_\infty^2}\left(\frac{\partial\phi}{\partial t} + \frac{1}{2}\left(\left(\frac{\partial\phi}{\partial x}\right)^2 - u_\infty^2\right)\right)}. \tag{2.48}$$

Then, the non-reflecting condition, eq.(2.46), becomes

$$u \pm \frac{2c}{\gamma-1} = u_\infty \pm \frac{2c_\infty}{\gamma-1}. \tag{2.49}$$

Eq.(2.49 needs a linearisation to be solved. Defining the perturbed potential φ:

$$\boldsymbol{v} = u_\infty \mathbf{i} + \nabla\varphi \rightarrow \varphi_x = u - u_\infty, \tag{2.50}$$

eq.(2.48) becomes:

$$\frac{c}{c_\infty} = 1 - \frac{\gamma-1}{2c_\infty^2}\left(\varphi_t + \frac{1}{2}\left((u_\infty + \varphi_x)^2 - u_\infty^2\right)\right) \simeq 1 - \frac{\gamma-1}{2c_\infty^2}\left(\varphi_t + u_\infty\varphi_x\right). \tag{2.51}$$

Combining eq.(2.51) with eq.(2.49), we obtain:

$$\varphi_x = \pm\frac{1}{c_\infty}(\varphi_t + u_\infty\varphi_x) \rightarrow \varphi_x = \pm\frac{\varphi_t}{c_\infty \mp u_\infty}. \tag{2.52}$$

Using eq.(2.50), the far-field normal inflow is obtained:

$$u = u_\infty \pm \frac{\varphi_t}{c_\infty \mp u_\infty}. \tag{2.53}$$

For a multi-dimensional domain, the non-reflecting condition, eq.(2.53), becomes:

$$\frac{\partial\phi}{\partial n} = V_\infty^n \pm \frac{\phi_t}{c_\infty \mp V_\infty^n}, \tag{2.54}$$

where V_∞^n is the normal component of the asymptotic speed on the boundary. This technique leads to a non reflecting condition that is exact for one dimensional cases but remains only an acceptable approximation for multi-dimensional cases, when applied normally to the boundary.

2.4 BOUNDARY CONDITIONS ON THE BODY

The tangential flow condition on the body surface,

$$V_{relative}^n = V_{flow}^n - V_{body}^n = \frac{\partial\phi}{\partial n} - (\boldsymbol{V}_G \cdot \mathbf{n})_{body} = 0, \tag{2.55}$$

where V_{body}^n is related to body motions, states the non-permeability of the solid boundary. Evaluating on the body boundary Γ_b the last

term of the integral continuity equation, eq.(2.25), and applying the boundary condition, eq.(2.55), a density flux appears at the boundary,

$$F_{body} = \int_{\Gamma_b} \rho \mathbf{V}_G \cdot \mathbf{n} d\Gamma_b. \tag{2.56}$$

On the other side, the boundary condition, eq.(2.55), has no effect on the ALE integral form [54] of the Bernoulli theorem, eq.(2.32), because no boundary integral appears.

A rigorous treatment of unsteady conditions needs a moving domain and so an ALE formulation. However, at each time step, the grid must be deformed on the fluid domain and the associated grid velocity $\mathbf{V}_G$ must be computed. So, the ALE formulation can involve an undue computational effort in some applications. For example, when the stability of a system around a reference configuration, i.e. the linearised flutter, must be analysed only small boundary motion can be considered. This allows to use *transpiration*: the domain is locked and the body motion is simulated by assigning the corresponding normal speed at the boundary. Thus, the grid velocity $\mathbf{V}_G$ can be neglected in the whole domain except at the solid boundary where the flux term, eq.(2.56), persists. The transpiration idea was first developed by Lighthill [39]. He used a method of equivalent sources to simulate changes in airfoil thickness. Instead of thickening the actual airfoil, an equivalent surface distribution of sources is used to simulate the boundary layer. Such an approach has proven to be an effective tool for reducing the time required for slightly perturbed aerodynamic calculations. A rigorous mathematical justification of the transpiration can be developed by writing the fluid problem in variational form at an actual configuration [24]. However, a qualitative explanations is proposed in chapter 4. Looking at the continuity equation, eq.(2.25), and the integral Bernoulli theorem, eq.(2.32), the transpiration leads to neglect the volume terms related to the gradient of the density and the velocity potential. Actually, such terms rapidly decrease away from the body, proving the effectiveness of the transpiration technique.

2.5 PERIODIC BOUNDARIES

Periodic boundary conditions arise from a particular type of symmetry, if a component repeats a pattern of a flow distribution more than twice, thus violating the mirror image requirements needed for symmetric boundary condition. In our case, the computational domain can be divided into N sectors, with N being the number of blades. For open rotors applications, the complete domain is a hollow cylinder: the hub is the inner surface, while the far field is the external surface. In order to reduce the computational effort, the base annulus is divided in N sections. This simplification is valid only if the asymptotic velocity $\mathbf{V}_\infty$ is aligned with the angular velocity vector $\vec{\Omega}$ as explained

in sec.(2.1). In fig.(14), it is represented the division of the base annulus in a common configuration of 8 bladed rotor. The internal radius corresponds to the hub, while the external radius is chosen so avoiding any problem due to a bounded domain, i.e. typically $R_{ext} \simeq 3 \div 4$ b, where b is the blade span.

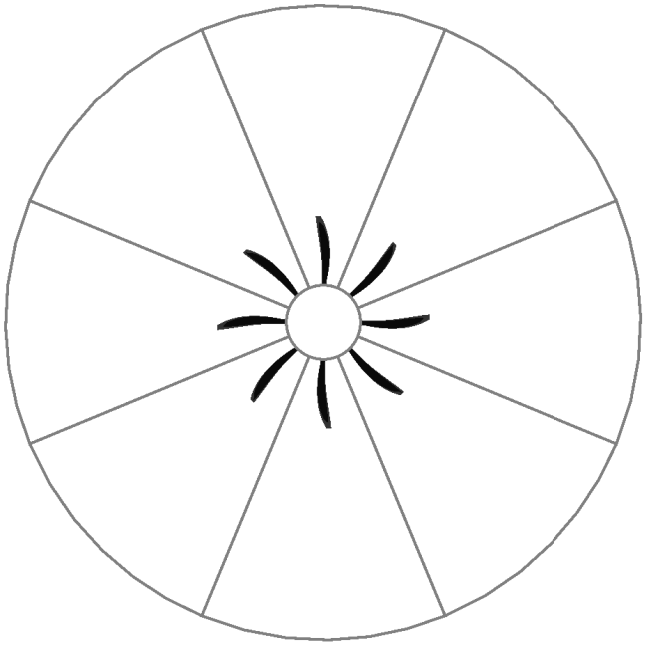

Figure 9: Periodic Domain XY view.

The periodic boundary condition is imposed onto the lateral surface of the reduced domain. These two surfaces are linked together, so that what leaves one surface is what gets into the other one. The angular velocity allows the distinction between "outflow" and "inflow" faces. Knowing that the domain is discretized, the simplest solution to relate the two faces implies the same mesh over lateral surfaces. So, a one to one relationship is achieved between the vertices of the two surfaces (blue and red ones in fig.(10)). In fig.(11), it is represented the lateral external mesh viewed along the wind direction. It can be inferred that the lateral surface grid is identical for the two periodic faces.
Having the same grid onto these faces is not so crucial because the solution can be represented by an interpolating scheme, so loosing the one to one relationship between the nodes of the outflow and of the inflow face. In this way, a rectangular interpolating matrix $[A_{ij}]$ is so created

$$\mathbf{u}^{inflow} = [A]\ \mathbf{u}^{outflow}, \tag{2.57}$$

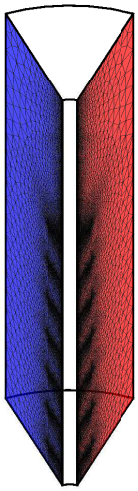

Figure 10: Periodic Faces.

where, $\mathbf{u}$ contains the values of the density ρ and velocity potential ϕ of the two surfaces. In this way, the unknowns onto the inflow face are recovered by those of the outflow face. The matrix $[A_{ij}]$ represents the linear operator which connects the unknowns of the two surfaces. However, this solution is not exploited in this work, so the same lateral grid is always needed.

The periodic boundary conditions are a valuable tool for reducing the computational effort needed to simulate the aerodynamics of such systems. They are also valid for steady (the case of a single rotating rotor) or unsteady simulations (the case of two contra-rotating rotors).

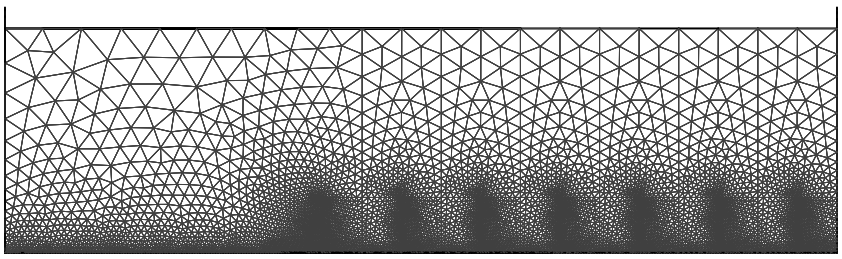

Figure 11: Lateral Surface Mesh.

The mesh generation for a full potential solver is not so easy because of the wake representation. As a clarification example, fig.(12) repre-

sents a 2D mesh around a $NACA-0012$ airfoil. It can be inferred that the wake (red points) spills out of the "outflow" face (green line) and gets into the "inflow" face (cyan line). Furthermore, the upwind "desymmetrization" bias, introduced for the treatment of supersonic regions and for the stability of the numerical schemes, imposes also a space causality between the periodic boundaries. In the example of fig 12, upwind triangles of the "inflow" line are the triangles of the "outflow" line.

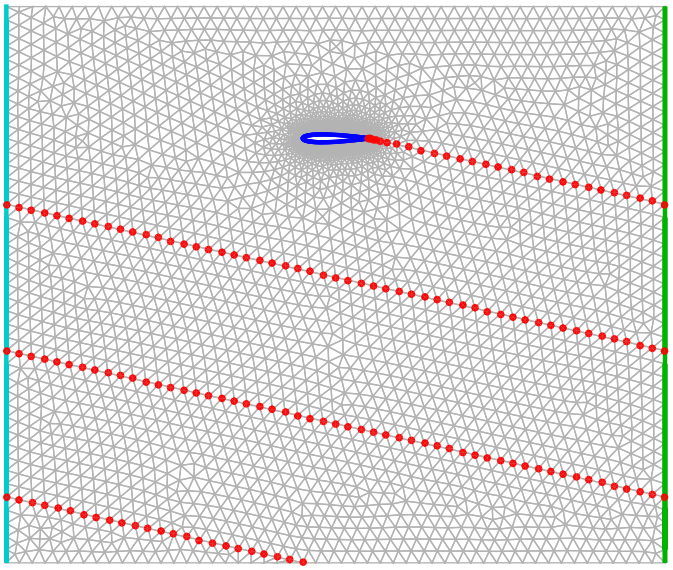

Figure 12: Example of the periodic boundary for a 2D application.

The next figures (13 and 14) show the computational domain of a single propeller prop-fan with 8 blades. The propeller wake geometry is a helicoid (in 3D), which can be expressed in Cartesian coordinates as

$$\begin{aligned} x &= \rho \cos(\Omega\, t), \\ y &= \rho \sin(\Omega\, t), \\ z &= V_\infty\, t, \end{aligned} \tag{2.58}$$

where $\mathbf{\Omega} = \{0; 0; \Omega\}$ is the angular velocity vector, $\mathbf{V}_\infty = \{0; 0; V_\infty\}$ is the asymptotic velocity and ρ is the radial position. Knowing $\mathbf{\Omega}$, $\mathbf{V}_\infty$ and the number of blades, it is possible to sketch the wake surface.

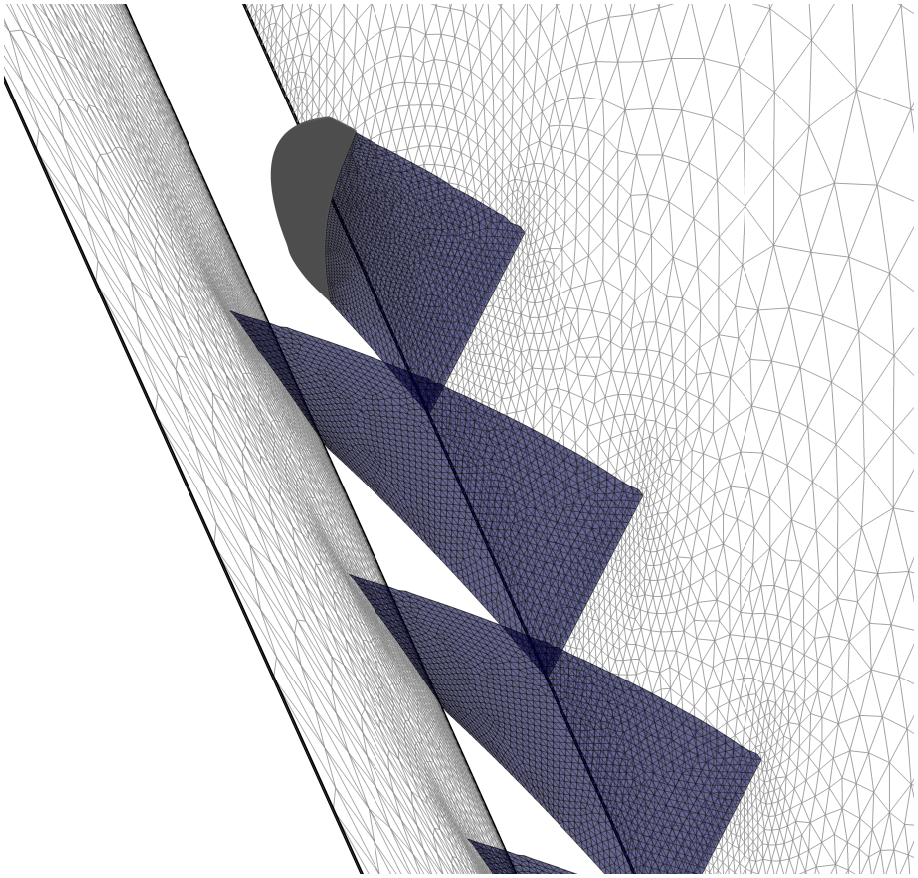

Figure 13: Periodic domain and wake representation for a 3D case - view 1.

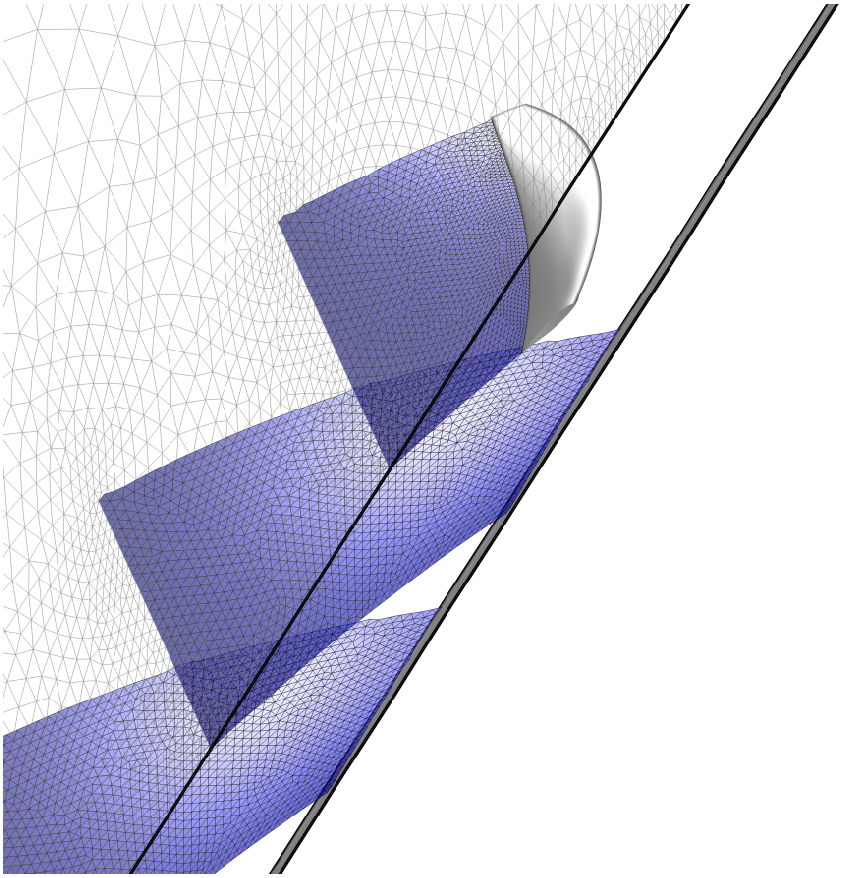

Figure 14: Periodic domain and wake representation for a 3D case - view 2.

2.6 WAKE INFLUENCE AND DOMAIN SIZE

In this section, the importance of the wake influence on the flow field around rotating bodies is discussed, remembering also that the domain size is a key issue to be dealt with when discretizing an infinite domain in external flows.

In a preliminary analysis, the momentum theory (MT) combined with the blade element theory (BET) can be used to evaluate the thrust, the torque and the inflow velocity of a lifting rotor in flight. As explained in ref.[38], each blade is divided into a number of independent sections along its span-wise direction. At each section a force balance is applied involving the 2D section lift and drag with the thrust and torque produced by the section (BET). At the same time a balance of axial and angular momentum is applied to evaluate the inflow ratio. This produces a set of non-linear equations that can be solved, at each section, through iterative methods. The resulting values of sections thrust and torque can then be summed up to predict the overall performance of the rotor.

As represented in fig.(15), the angle of attack α of a propeller section is

$$\alpha = \theta - \phi, \tag{2.59}$$

where θ is the geometric incidence and ϕ is the inflow angle, which is related to the wake and it is proportional to the thrust generated by the rotor T. If the induced velocity is uniform on the disk, then

$$v_{induced} = \sqrt{\frac{T}{2\rho A}}, \tag{2.60}$$

$$\phi = \tan\left(\frac{v_{induced}}{\Omega r}\right), \tag{2.61}$$

where A is the disk area, Ω is the angular velocity and r is the span position of the considered section. The primary influence of the wake is the reduction of the angle of attack which involves a reduction in thrust.

The influence of the wake has to be considered in our analyses and it must be included in the domain discretization. Since the grid has fixed dimensions and the wake cannot move freely, the asymptotic velocity, $\mathbf{V}_\infty$, has to be considered so allowing a small angle of attack along the wing-span. This constraint is related to the limits of a full potential analysis which gives good approximations of the real flow fields only at a low angles of attack, i.e. without large separated flows. After evaluating the asymptotic velocity, we are able to design the blade wake geometry which is a helicoid (in 3D).

Afterwards, a convergence study is performed in order to understand the number of "wakes" that have to be included in the mesh. It is clear that these wakes are those released by other blades during

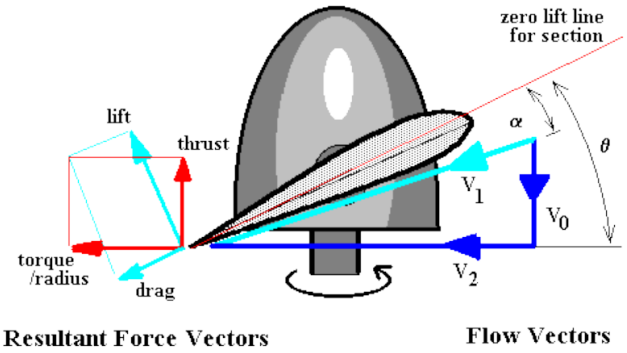

Figure 15: Blade Element Momentum Theory - `www.sites.google.com/site/aerodynamics4students/`

the rotation. Fig.(16) shows the results of such a convergence study. With a good approximations, it was decided that 9 "wake turns" behind the body are sufficient. If the rotor has 8 blades, this means that the computational domain contains the wakes released by a complete revolution of every blade. This is a property that does not change with the propeller setting angle and so with the asymptotic velocity V_∞. It must be emphasized that more wakes mean larger computational domains and so a higher computational effort to solve the system of eqs.(2.40,2.41,2.42,2.43,2.44). However, the total number of cells is always moderate because the periodic boundary conditions are exploited. Moreover, the increase of cells is not so predominant because the most dense region is around the aerodynamic body (and not far away from it).

Thanks to the domain periodicity, it is only required to set up a fine mesh around the body (in order to correctly represent its pressure distribution) and a medium size mesh onto the wake surfaces (in order to represent correctly the transport of velocity potential jump, $\Delta\phi$, across the wake).

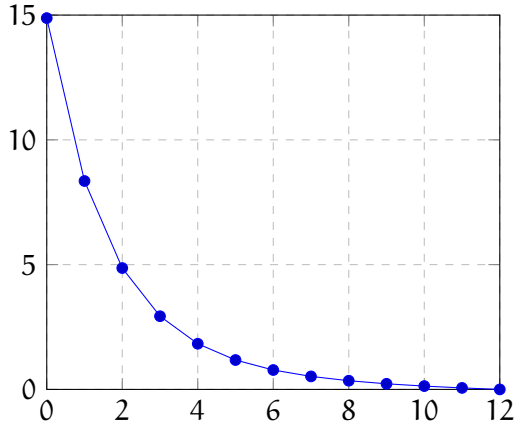

Figure 16: Number of "Wake Turns" VS Thrust Relative Error [%]

3

STRUCTURAL SUB-SYSTEM

This chapter provides an accurate description of the structural sub-system, in such a view, the choice of the reference frame and the description of the *centrifugal* and the *Coriolis* loads are not simple tasks, even if the periodicity of the domain can be used to simplify the geometry as for the aerodynamic analysis. Usually, the hub is not considered when modelling the rotor because it is stiffer than blades. So, blades can be considered structurally independent bodies that interact with each other through the aerodynamics.

In particular, a complete formulation for rotating bodies, including the rigid motions of the hub, is discussed, with a particular focus on the representation of inertial forces, i.e. the afore mentioned Coriolis and centrifugal ones.

3.1 REFERENCE FRAMES

The apparent forces acting on a steadily rotating structure are the *centrifugal* and the *Coriolis* loads, and the dynamic response of the blades is strongly affected by these actions. Often, the use of a rotating reference system is the simplest approach to formulate the dynamic equations. As explained in [26] and [74], the coordinates of a generic point of a rotating structure is defined using three different coordinates systems:

- An inertial reference system (to which relate accelerations and inertia forces);
- A reference system associated to the mean motion of the undeformed disk, which is defined by a new origin $\mathbf{x}_0$ and by a rotation matrix $[\boldsymbol{\alpha}]$;
- A reference system related to the perturbed motion of the disk, which is defined by a perturbation $\Delta\mathbf{x}_0$ of $\mathbf{x}_0$ and by a perturbation of rotation matrix $[\Delta\boldsymbol{\Gamma}]$.

Using the above description, the generic coordinates of a body point are:

$$\mathbf{x} = \mathbf{x}_0 + [\boldsymbol{\alpha}]\,\Delta\mathbf{x}_0 + [\boldsymbol{\alpha}]\,[\Delta\boldsymbol{\Gamma}]\,(\mathbf{r} + \mathbf{u} + \Delta\mathbf{u}) \tag{3.1}$$

Where the position $\mathbf{x}$ of each structural point is espressed in fixed coordinates using a moving reference frame:

- $\mathbf{x}_0$ is the origin of the moving reference system;
- $[\boldsymbol{\alpha}]$ is the rotation matrix of the moving reference frame;
- $\Delta\mathbf{x}_0$ is the variation of the moving frame origin;
- $[\Delta\boldsymbol{\Gamma}]$ is a pertubation of the orientation of moving reference;
- In the moving reference, the position is given by the undeformed location $\mathbf{r}$ plus a displacement, which is separated into a trimmed (steady condition) contribution $\mathbf{u}$ and a dynamic perturbation contribution $\Delta\mathbf{u}$.

3.2 KINEMATIC RELATIONS

After developing the second order matrix approximation of $[\Delta\boldsymbol{\Gamma}]$ as a function of rotation vector $\boldsymbol{\psi}$:

$$[\Delta\boldsymbol{\Gamma}] = \mathbf{I} + \boldsymbol{\Delta\psi}_\times + \frac{1}{2}\boldsymbol{\Delta\psi}_\times\boldsymbol{\Delta\psi}_\times, \tag{3.2}$$

and substituting it in eq.(3.1), one obtains:

$$\begin{aligned}\mathbf{x} = \mathbf{x}_0 &+ [\boldsymbol{\alpha}]\,\Delta\mathbf{x}_0 + [\boldsymbol{\alpha}]\,(\mathbf{r}+\mathbf{u}+\Delta\mathbf{u}) - [\boldsymbol{\alpha}]\,[(\mathbf{r}+\mathbf{u})_\times]\,\boldsymbol{\Delta\psi} \\ &+ \underbrace{\frac{1}{2}[\boldsymbol{\alpha}]\,\boldsymbol{\Delta\psi}_\times\boldsymbol{\Delta\psi}_\times\,(\mathbf{r}+\mathbf{u}) + [\boldsymbol{\alpha}]\,\boldsymbol{\Delta\psi}_\times\,\Delta\mathbf{u}}_{=\mathrm{A}} \\ &+ \underbrace{\frac{1}{2}[\boldsymbol{\alpha}]\,\boldsymbol{\Delta\psi}_\times\boldsymbol{\Delta\psi}_\times\,\Delta\mathbf{u}}_{=\mathrm{B}}.\end{aligned} \tag{3.3}$$

The term "B" of the previous expression can be neglected because it is a third order term, while the term "A" gives a not negligible contribution to the virtual displacement vector (but it will neglected for accelerations). In fact, the virtual work, obtained by multiplication between the virtual variation of "A" and constant acceleration terms, is not negligible.

Recalling the properties of $[\boldsymbol{\alpha}]$

$$[\boldsymbol{\alpha}]^\mathsf{T}[\boldsymbol{\alpha}] = \mathrm{I}, \tag{3.4}$$

$$\frac{\mathrm{d}}{\mathrm{d}t}\left([\boldsymbol{\alpha}]^\mathsf{T}[\boldsymbol{\alpha}]\right) = \mathbf{0},$$

$$[\boldsymbol{\alpha}]^\mathsf{T}[\dot{\boldsymbol{\alpha}}] = -[\dot{\boldsymbol{\alpha}}]^\mathsf{T}[\boldsymbol{\alpha}] = \bar{\boldsymbol{\omega}}, \tag{3.5}$$

In which $\bar{\boldsymbol{\omega}}$ is a skew matrix exspressing the body angular velocity in the moving frame:

$$\bar{\boldsymbol{\omega}} = \begin{bmatrix} 0 & -\omega_3 & \omega_2 \\ \omega_3 & 0 & -\omega_1 \\ -\omega_2 & \omega_1 & 0 \end{bmatrix}. \tag{3.6}$$

Differentiating eq.(3.5) with respect to time,

$$[\ddot{\alpha}] = \frac{d}{dt}([\alpha]\bar{\omega}) = [\alpha]\dot{\bar{\omega}} + [\alpha]\bar{\omega}\bar{\omega}. \tag{3.7}$$

The angular velocity remains constant in our problems so we can drop the terms with $\dot{\bar{\omega}}$.

Differentiating with respect to time eq.(3.3), one obtains the velocity vector

$$\begin{aligned}\dot{x} = {} & \dot{x}_0 + [\dot{\alpha}]\Delta x_0 + [\alpha]\Delta\dot{x_0} + [\dot{\alpha}](r+u) + [\alpha]\dot{u} \\ & - [\dot{\alpha}](r+u)_\times \Delta\psi - [\alpha](r+u)_\times \Delta\dot{\psi} \\ & - [\alpha]\dot{u}_\times \Delta\psi + [\dot{\alpha}]\Delta u + [\alpha]\Delta\dot{u}.\end{aligned} \tag{3.8}$$

Differentiating with respect to time eq.(3.8), the accelerations are obtained

$$\begin{aligned}\ddot{x} = {} & [\alpha]V_0 + [\alpha]\bar{\omega}V_0 + [\alpha]\bar{\omega}\bar{\omega}\Delta x_0 + [\alpha]\dot{\bar{\omega}}\Delta x_0 \\ & + 2[\alpha]\bar{\omega}\Delta\dot{x_0} + [\alpha]\Delta\ddot{x_0} + [\alpha]\bar{\omega}\bar{\omega}(r+u) + [\alpha]\dot{\bar{\omega}}(r+u) \\ & + 2[\alpha]\bar{\omega}\dot{u} + [\alpha]\ddot{u} - [\alpha](r+u)_\times \Delta\ddot{\psi} - 2\left([\alpha]\bar{\omega}[\alpha](r+u)_\times + [\alpha]\dot{u}_\times\right)\Delta\dot{\psi} \\ & - \left([\alpha]\bar{\omega}\bar{\omega}(r+u)_\times + [\alpha]\dot{\bar{\omega}}(r+u)_\times + 2[\alpha]\bar{\omega}\dot{\bar{\omega}} + [\alpha]\ddot{u}_\times\right)\Delta\psi \\ & + [\alpha](r+u)_\times \Delta\ddot{\psi} + [\alpha]\bar{\omega}\bar{\omega}\Delta u + [\alpha]\dot{\bar{\omega}}\Delta u \\ & + 2[\alpha]\bar{\omega}\Delta\dot{u} + [\alpha]\Delta\ddot{u}.\end{aligned} \tag{3.9}$$

Introducing the finite element approximation, the displacement vector can be viewed as the product of a matrix of shape functions and a vector of appropriate free coordinates:

$$u = Nq, \qquad \Delta u = N\Delta q. \tag{3.10}$$

Calling:

$$R = r + u = r + Nq, \qquad t = \begin{Bmatrix}\Delta x_0 \\ \Delta\psi \\ \Delta q\end{Bmatrix},$$

the expression of the accelerations, eq.(3.9), becomes:

$$\begin{aligned}\ddot{x} = {} & [\alpha]\left(\bar{\omega}V_0 + \dot{V}_0 + \bar{\omega}\bar{\omega}R + \dot{\bar{\omega}}R + 2\bar{\omega}N\dot{q} + N\ddot{q}\right) \\ & + [\alpha]\Big[\bar{\omega}\bar{\omega} + \dot{\bar{\omega}} \quad -\bar{\omega}\bar{\omega}R_\times - \dot{\bar{\omega}}R_\times - 2\bar{\omega}(N\dot{q})_\times + (N\ddot{q})_\times \\ & \bar{\omega}\bar{\omega}N + \dot{\bar{\omega}}N\Big]t + [\alpha]\Big[2\bar{\omega} \quad -2\bar{\omega}R_\times - 2(N\dot{q})_\times \quad 2\bar{\omega}N\Big]\dot{t} \\ & + [\alpha]\Big[I \quad -R_\times \quad N\Big]\ddot{t}.\end{aligned} \tag{3.11}$$

The same approach can be used for the virtual displacement of a generic material point:

$$\begin{aligned}\delta x = {} & [\alpha]\Big[I \quad -[R_\times] \quad N\Big]\delta t \\ & + [\alpha]\Big[0 \quad \frac{1}{2}R_\times\Delta\psi_\times - \Delta\psi_\times R_\times - (N\Delta q)_\times \quad \Delta\psi_\times N\Big]\delta t.\end{aligned} \tag{3.12}$$

3.3 VIRTUAL WORK PRINCIPLE OF INERTIA FORCES

The virtual work of the inertia forces is simply:

$$\delta W^i = \int_{\mathcal{V}} \delta \mathbf{x}^T \rho \ddot{\mathbf{x}} d\mathcal{V}. \tag{3.13}$$

Using eq.(3.11) and eq.(3.12) for accelerations and virtual displacement respectively, eq.(3.13) becomes:

$$\begin{aligned}
\delta W^i = {} & \delta \mathbf{t}^T \int_{\mathcal{V}} \begin{bmatrix} \mathbf{I} \\ \mathbf{R}_\times \\ \mathbf{N}^T \end{bmatrix} \left(\bar{\boldsymbol{\omega}} \mathbf{V}_0 + \dot{V}_0 + \bar{\boldsymbol{\omega}} \bar{\boldsymbol{\omega}} \mathbf{R} + \dot{\bar{\boldsymbol{\omega}}} \mathbf{R} + 2 \bar{\boldsymbol{\omega}} \mathbf{N} \dot{\mathbf{q}} + \mathbf{N} \ddot{\mathbf{q}} \right) \rho d\mathcal{V} \\
& + \delta \mathbf{t}^T \int_{\mathcal{V}} \begin{bmatrix} \mathbf{I} \\ \mathbf{R}_\times \\ \mathbf{N}^T \end{bmatrix} \Big[\bar{\boldsymbol{\omega}} \bar{\boldsymbol{\omega}} + \dot{\bar{\boldsymbol{\omega}}} \quad - \bar{\boldsymbol{\omega}} \bar{\boldsymbol{\omega}} \mathbf{R}_\times - \dot{\bar{\boldsymbol{\omega}}} \mathbf{R}_\times - \\
& 2 \bar{\boldsymbol{\omega}} (\mathbf{N} \dot{\mathbf{q}})_\times + (\mathbf{N} \ddot{\mathbf{q}})_\times \bar{\boldsymbol{\omega}} \bar{\boldsymbol{\omega}} \mathbf{N} + \dot{\bar{\boldsymbol{\omega}}} \mathbf{N} \Big] \rho d\mathcal{V} \, \mathbf{t} \\
& + \delta \mathbf{t}^T \int_{\mathcal{V}} \begin{bmatrix} \mathbf{0} \\ \frac{1}{2} \Delta \boldsymbol{\psi}_\times \mathbf{R}_\times - \mathbf{R}_\times \Delta \boldsymbol{\psi}_\times + (\mathbf{N} \Delta \mathbf{q})_\times \\ \mathbf{N}^T \Delta \boldsymbol{\psi}_\times{}^T \end{bmatrix} \left(\bar{\boldsymbol{\omega}} \mathbf{V}_0 + \dot{V}_0 \right. \\
& \left. + \bar{\boldsymbol{\omega}} \bar{\boldsymbol{\omega}} \mathbf{R} + \dot{\bar{\boldsymbol{\omega}}} \mathbf{R} + 2 \bar{\boldsymbol{\omega}} \mathbf{N} \dot{\mathbf{q}} + \mathbf{N} \ddot{\mathbf{q}} \right) \rho d\mathcal{V} \\
& + \delta \mathbf{t}^T \int_{\mathcal{V}} \begin{bmatrix} \mathbf{I} \\ \mathbf{R}_\times \\ \mathbf{N}^T \end{bmatrix} 2 \Big[\bar{\boldsymbol{\omega}} \quad - \bar{\boldsymbol{\omega}} \mathbf{R}_\times - (\mathbf{N} \dot{\mathbf{q}})_\times \quad \bar{\boldsymbol{\omega}} \mathbf{N} \Big] \rho d\mathcal{V} \, \dot{\mathbf{t}} \\
& + \delta \mathbf{t}^T \int_{\mathcal{V}} \begin{bmatrix} \mathbf{I} \\ \mathbf{R}_\times \\ \mathbf{N}^T \end{bmatrix} \Big[\mathbf{I} \quad - \mathbf{R}_\times \quad \mathbf{N} \Big] \rho d\mathcal{V} \ddot{\mathbf{t}}.
\end{aligned} \tag{3.14}$$

After some calculations, this compact form for the virtual work of inertia forces is achieved:

$$\delta W^i = \delta \mathbf{t}^T \left(\mathbf{M} \ddot{\mathbf{t}} + \mathbf{C_c} \dot{\mathbf{t}} + \mathbf{K_c} \mathbf{t} + \mathbf{F_c} \right), \tag{3.15}$$

whose terms are reported in the next page.

$$\mathbf{F_c} = \begin{Bmatrix} \mathrm{diag}[\mathrm{m}]\bar{\boldsymbol{\omega}}\mathbf{V}_0 + \mathrm{diag}[\mathrm{m}]\dot{\mathbf{V}}_0 - \bar{\boldsymbol{\omega}}\mathbf{S}\bar{\boldsymbol{\omega}} - \mathbf{S}\dot{\bar{\boldsymbol{\omega}}} + \int_{\mathcal{V}} (2\bar{\boldsymbol{\omega}}\mathbf{N}\dot{\mathbf{q}} + \mathbf{N}\ddot{\mathbf{q}})\,\rho d\mathcal{V} \\ \mathbf{S}\bar{\boldsymbol{\omega}}\mathbf{V}_0 + \mathbf{S}\dot{\mathbf{V}}_0 + \bar{\boldsymbol{\omega}}\mathbf{J}\bar{\boldsymbol{\omega}} + \mathbf{J}\dot{\bar{\boldsymbol{\omega}}} + \int_{\mathcal{V}} (2\mathbf{R}_\times\bar{\boldsymbol{\omega}}\mathbf{N}\dot{\mathbf{q}} + \mathbf{N}\ddot{\mathbf{q}})\,\rho d\mathcal{V} \\ \int_{\mathcal{V}} \left(\mathbf{N}^T\bar{\boldsymbol{\omega}}\mathbf{V}_0 + \mathbf{N}^T\dot{\mathbf{V}}_0 + \mathbf{N}^T\bar{\boldsymbol{\omega}}\bar{\boldsymbol{\omega}}\mathbf{R} + \mathbf{N}^T\dot{\bar{\boldsymbol{\omega}}}\mathbf{R} + 2\mathbf{N}^T\bar{\boldsymbol{\omega}}\mathbf{N}\dot{\mathbf{q}} + \mathbf{N}^T\mathbf{N}\ddot{\mathbf{q}}\right)\rho d\mathcal{V} \end{Bmatrix}; \tag{3.16}$$

$$\mathbf{K_c} = \begin{bmatrix} \mathrm{diag}[\mathrm{m}]\bar{\boldsymbol{\omega}}\bar{\boldsymbol{\omega}} + \mathrm{diag}[\mathrm{m}]\dot{\bar{\boldsymbol{\omega}}} & \mathbf{A} & \int_{\mathcal{V}} \left(\bar{\boldsymbol{\omega}}\bar{\boldsymbol{\omega}}\mathbf{N} + \dot{\bar{\boldsymbol{\omega}}}\mathbf{N}\right)\rho d\mathcal{V} \\ \left(\bar{\boldsymbol{\omega}}\bar{\boldsymbol{\omega}}\mathbf{S}^T\right)^T - \left(\dot{\bar{\boldsymbol{\omega}}}\mathbf{S}^T\right)^T & \mathbf{B} & \mathbf{D} \\ \int_{\mathcal{V}} \left(\mathbf{N}^T\bar{\boldsymbol{\omega}}\bar{\boldsymbol{\omega}} + \mathbf{N}^T\dot{\bar{\boldsymbol{\omega}}}\right)\rho d\mathcal{V} & \mathbf{C} & \int_{\mathcal{V}} \left(\mathbf{N}^T\bar{\boldsymbol{\omega}}\bar{\boldsymbol{\omega}}\mathbf{N} + \mathbf{N}^T\dot{\bar{\boldsymbol{\omega}}}\mathbf{N}\right)\rho d\mathcal{V} \end{bmatrix}; \tag{3.17}$$

$$\mathbf{C_c} = 2\begin{bmatrix} \mathrm{diag}[\mathrm{m}]\bar{\boldsymbol{\omega}} & \bar{\boldsymbol{\omega}}\mathbf{S}^T - \int_{\mathcal{V}} (\mathbf{N}\dot{\mathbf{q}})_\times \rho d\mathcal{V} & \int_{\mathcal{V}} \bar{\boldsymbol{\omega}}\mathbf{N}\rho d\mathcal{V} \\ -\left(\bar{\boldsymbol{\omega}}\mathbf{S}^T\right)^T & -\frac{1}{2}(\mathbf{J}\bar{\boldsymbol{\omega}})_\times + \frac{1}{2}\mathbf{J}\bar{\boldsymbol{\omega}} + \frac{1}{2}\bar{\boldsymbol{\omega}}\mathbf{J} - \int_{\mathcal{V}} \mathbf{R}_\times (\mathbf{N}\dot{\mathbf{q}})_\times \rho d\mathcal{V} & \int_{\mathcal{V}} \mathbf{R}_\times\bar{\boldsymbol{\omega}}\mathbf{N}\rho d\mathcal{V} \\ \int_{\mathcal{V}} \mathbf{N}^T\bar{\boldsymbol{\omega}}\rho d\mathcal{V} & \int_{\mathcal{V}} \left(-\mathbf{N}^T\bar{\boldsymbol{\omega}}\mathbf{R}_\times - \mathbf{N}^T(\mathbf{N}\dot{\mathbf{q}})_\times\right)\rho d\mathcal{V} & \int_{\mathcal{V}} \mathbf{N}^T\bar{\boldsymbol{\omega}}\mathbf{N}\rho d\mathcal{V} \end{bmatrix}; \tag{3.18}$$

$$\mathbf{M} = \begin{bmatrix} \mathrm{diag}[\mathrm{m}] & \mathbf{S}^T & \int_{\mathcal{V}} \mathbf{N}\rho d\mathcal{V} \\ \mathbf{S} & \mathbf{J} & \int_{\mathcal{V}} \mathbf{R}_\times\mathbf{N}\rho d\mathcal{V} \\ \int_{\mathcal{V}} \mathbf{N}^T\rho d\mathcal{V} & \int_{\mathcal{V}} \mathbf{N}^T{\mathbf{R}_\times}^T\rho d\mathcal{V} & \int_{\mathcal{V}} \mathbf{N}^T\mathbf{N}\rho d\mathcal{V} \end{bmatrix}; \tag{3.19}$$

$$\mathbf{A} = \bar{\boldsymbol{\omega}}\bar{\boldsymbol{\omega}}\mathbf{S}^{\mathsf{T}} + \dot{\bar{\boldsymbol{\omega}}}\mathbf{S}^{\mathsf{T}} - \int_{\mathcal{V}} \left(\bar{\boldsymbol{\omega}}\bar{\boldsymbol{\omega}}(\mathbf{N}\dot{\mathbf{q}})_{\times} + \dot{\bar{\boldsymbol{\omega}}}(\mathbf{N}\ddot{\mathbf{q}})_{\times}\right) \rho \mathrm{d}\mathcal{V}; \tag{3.20}$$

$$\begin{aligned}\mathbf{B} = {} & \frac{1}{2}\mathbf{S}(\mathbf{N}\mathbf{V}_0)_{\times} + \frac{1}{2}(\mathbf{N}\mathbf{V}_0)_{\times}\mathbf{S} + \frac{1}{2}\mathbf{S}\dot{\mathbf{V}}_{0\times} + \frac{1}{2}\dot{\mathbf{V}}_{0\times}\mathbf{S} - \frac{1}{2}\left(\mathbf{J}\dot{\bar{\boldsymbol{\omega}}}\right)_{\times} + \mathbf{J}\dot{\bar{\boldsymbol{\omega}}} - \frac{1}{2}(\mathbf{J}\bar{\boldsymbol{\omega}})_{\times}\bar{\boldsymbol{\omega}} - \frac{1}{2}\bar{\boldsymbol{\omega}}(\mathbf{J}\bar{\boldsymbol{\omega}})_{\times} \\ & + \bar{\boldsymbol{\omega}}\mathbf{J}\bar{\boldsymbol{\omega}} + \int_{\mathcal{V}} \left(\mathbf{R}_{\times}(\bar{\boldsymbol{\omega}}\mathbf{N}\dot{\mathbf{q}})_{\times} + (\bar{\boldsymbol{\omega}}\mathbf{N}\dot{\mathbf{q}})_{\times}\mathbf{R}_{\times} + 2\mathbf{R}_{\times}\bar{\boldsymbol{\omega}}\mathbf{N}\dot{\mathbf{q}})_{\times} - \frac{1}{2}\mathbf{R}_{\times}\mathbf{N}\ddot{\mathbf{q}})_{\times} + \frac{1}{2}\mathbf{N}\ddot{\mathbf{q}})_{\times}\mathbf{R}_{\times}\right) \rho \mathrm{d}\mathcal{V};\end{aligned} \tag{3.21}$$

$$\begin{aligned}\mathbf{C} = {} & \int_{\mathcal{V}} \Big(2\mathbf{N}^{\mathsf{T}}(\bar{\boldsymbol{\omega}}\mathbf{V}_0)_{\times} + 2\mathbf{N}^{\mathsf{T}}\bar{\boldsymbol{\omega}}\dot{\mathbf{V}}_{0\times} + \mathbf{N}^{\mathsf{T}}(\bar{\boldsymbol{\omega}}\bar{\boldsymbol{\omega}}\mathbf{R})_{\times} - \mathbf{N}^{\mathsf{T}}\bar{\boldsymbol{\omega}}\bar{\boldsymbol{\omega}}\mathbf{R}_{\times} \\ & - \mathbf{N}^{\mathsf{T}}\mathbf{R}_{\times}\dot{\bar{\boldsymbol{\omega}}} - 2\mathbf{N}^{\mathsf{T}}\mathbf{N}\dot{\mathbf{q}})_{\times}\bar{\boldsymbol{\omega}} + 2\mathbf{N}^{\mathsf{T}}\mathbf{N}\ddot{\mathbf{q}})_{\times}\Big)\rho \mathrm{d}\mathcal{V};\end{aligned} \tag{3.22}$$

$$\begin{aligned}\mathbf{D} = {} & \int_{\mathcal{V}} \Big(\mathbf{R}_{\times}\bar{\boldsymbol{\omega}}\bar{\boldsymbol{\omega}}\mathbf{N} + \mathbf{R}_{\times}\dot{\bar{\boldsymbol{\omega}}}\mathbf{N} - (\bar{\boldsymbol{\omega}}\mathbf{V}_0)_{\times}\mathbf{N} - \dot{\mathbf{V}}_{0\times}\mathbf{N} - (\bar{\boldsymbol{\omega}}\bar{\boldsymbol{\omega}}\mathbf{R})_{\times}\mathbf{N} \\ & - \left(\dot{\bar{\boldsymbol{\omega}}}\mathbf{R}\right)_{\times}\mathbf{N} - 2\bar{\boldsymbol{\omega}}\mathbf{N}\dot{\mathbf{q}})_{\times}\mathbf{N} - \mathbf{N}\ddot{\mathbf{q}})_{\times}\mathbf{N}\Big)\rho \mathrm{d}\mathcal{V}.\end{aligned} \tag{3.23}$$

The vector $\mathbf{F_c}$ represents the generalized inertia forces related to the mean motion of the structure. These forces are in equilibrium with the elastic ones and with external loads related to the mean motion. In this way, the elastic trim of a rotating structure is computed, and, after it, one can drop these terms from the dynamic equations in order to study the linear stability of the system.

The matrix $\mathbf{K_c}$ introduces the so called *spin softening* effect. The existence of this matrix is related to the approach used to describe the displacements. Thus, adopting a Lagrangian approach, the centrifugal inertia forces depend on the deformed configuration of the structure, and so there is a stiffness contribution proportional to the square of angular velocity.

The matrix $\mathbf{C_c}$ represents the effect of Coriolis forces. Indeed, it is an apparent damping because Coriolis forces do not work for a virtual displacement. The contribution to damping of the Coriolis forces is always negligible if a constant angular velocity with no rigid motions of the hub are considered. In this way, the natural frequencies remain imaginary and eigenvectors become real (always if there are not other form of dissipation). Ref.[25] presents a detailed dissertation onto the effects of centrifugal and Coriolis forces on the mode shapes and frequencies of a rotating system. The Coriolis effect has an influence on the eigenfrequencies when rigid motion of the hub is accounted; this is important in structural redesigns where the frequencies must be adjusted.

3.4 VIRTUAL WORK PRINCIPLE OF ELASTIC FORCES

The virtual work of the generalized internal forces will generate a stiffness matrix. For a general analysis, such a matrix can be partitioned as,

$$\mathbf{K} = \begin{bmatrix} \mathbf{K}_{x_0x_0} & \mathbf{K}_{x_0\psi} & \mathbf{K}_{x_0q} \\ \mathbf{K}_{\psi x_0} & \mathbf{K}_{\psi\psi} & \mathbf{K}_{\psi q} \\ \mathbf{K}_{qx_0} & \mathbf{K}_{q\psi} & \mathbf{K}_{qq} \end{bmatrix} \tag{3.24}$$

where there are the coupling terms between rigid motion and deformable displacements. As already mentioned, our concern is mainly related to $\mathbf{K}_{qq}$, because the other terms are mainly related to the support compliances. In this work, the support is supposed to be perfectly rigid without any relative motion respect to the rotating frame, so only the term $\mathbf{K}_{qq}$ is modelled here.

In this application, the hypothesis of small displacement-rotation must be removed but we can hold the hypothesis of small strains. A *"Total Lagragian"* (T.L.) or an *"Updated Lagragian"* (U.L.) approach - used here - can be equally used to update the pre-stress terms. In the first approach, all the variables (static and kinematic) are referred to the *initial* condition (undeformed shape), while in the second one, the variables are referred to the last balanced configuration.

In the *Total* Lagrangian approach, strains and stresses can be splitted in a reference condition term and a perturbation term:

$$\begin{array}{ll} \text{Stresses} & \text{Strains} \\ S_{ij} = S^0_{ij} + \Delta S_{ij} & \varepsilon_{ij} = \varepsilon^0_{ij} + \Delta\varepsilon_{ij}, \end{array} \tag{3.25}$$

with

$$\Delta\varepsilon_{ij} = \Delta e_{ij} + \Delta\eta_{ij}, \tag{3.26}$$

$$\Delta e_{ij} = \frac{1}{2}\left(\Delta\bar{u}_{i,j} + \Delta\bar{u}_{j,i} + \bar{u}_{k,i}\Delta\bar{u}_{k,j} + \Delta\bar{u}_{k,i}\bar{u}_{k,j}\right), \tag{3.27}$$

$$\Delta\eta_{ij} = \frac{1}{2}\Delta\bar{u}_{k,i}\Delta\bar{u}_{k,j}. \tag{3.28}$$

The suffix "i,j" express the differentiation with respect to the jth coordinates of the ith coordinates; furthermore, the linear term and the non-linear term of the strain tensor are separated.

Remembering, the expression of the *Internal Virtual Work* (IVW),

$$\delta W_d = \int_{\mathcal{V}} S_{ij}\delta\varepsilon_{ij}\,d\mathcal{V} \tag{3.29}$$

$$= \int_{\mathcal{V}} (S^0_{ij} + \Delta S_{ij})(\varepsilon^0_{ij} + \Delta\varepsilon_{ij})\,d\mathcal{V}, \tag{3.30}$$

introducing a simple stress-strain relationship,

$$S_{ij} = C_{ijrs}\varepsilon_{rs}, \tag{3.31}$$

one obtain the linearized expression of the IVW (*tensorial form*)

$$\delta W_d = \int_{\mathcal{V}} S^0_{ij}\delta\varepsilon^0_{ij}d\mathcal{V} + \int_{\mathcal{V}} C_{ijrs}\Delta\varepsilon_{rs}\delta\Delta\varepsilon_{ij}d\mathcal{V} + \int_{\mathcal{V}} S^0_{ij}\delta\Delta\eta_{ij}d\mathcal{V}. \quad (3.32)$$

Developing displacements with proper shape functions and performing products between various terms, one obtain the *matrix form* of IVW

$$\delta W_d = \int_{\mathcal{V}} \boldsymbol{\varepsilon}^{0\mathsf{T}}\mathbf{S}^0 d\mathcal{V} + \delta\mathbf{q}^{\mathsf{T}}\left(\int_{\mathcal{V}} \mathbf{B_L}^{\mathsf{T}}\mathbf{D}\mathbf{B_L}d\mathcal{V} + \int_{\mathcal{V}} \mathbf{B_{NL}}^{\mathsf{T}}\mathbf{D}\mathbf{B_{NL}}d\mathcal{V}\right)\mathbf{q}. \quad (3.33)$$

The matrix $\mathbf{B_L}$ is the linear trasformation matrix between displacement-strain, and it can be splitted in $\mathbf{B_{L0}}$, indipendent from pre-deformation, and $\mathbf{B_{L1}}$, linear dipendent from deformation. So,

$$\mathbf{B_L} = \mathbf{B_{L0}} + \mathbf{B_{L1}}, \quad (3.34)$$

eq.(3.33) becomes

$$\delta W_d = \delta W_d^0 + \delta\mathbf{q}^{\mathsf{T}}\bar{\mathbf{K}}\mathbf{q}, \quad (3.35)$$

where

$$\delta W_d^0 = \int_{\mathcal{V}} \boldsymbol{\varepsilon}^{0\mathsf{T}}\mathbf{S}^0 d\mathcal{V}, \quad (3.36)$$

$$\bar{\mathbf{K}} = \mathbf{K} + \mathbf{K_L} + \mathbf{K_G}, \quad (3.37)$$

$$\mathbf{K} = \int_{\mathcal{V}} \mathbf{B_{L0}}^{\mathsf{T}}\mathbf{D}\mathbf{B_{L0}}d\mathcal{V}, \quad (3.38)$$

$$\mathbf{K_L} = \int_{\mathcal{V}} \left(\mathbf{B_{L0}}^{\mathsf{T}}\mathbf{D}\mathbf{B_{L1}} + \mathbf{B_{L1}}^{\mathsf{T}}\mathbf{D}\mathbf{B_{L0}} + \mathbf{B_{L1}}^{\mathsf{T}}\mathbf{D}\mathbf{B_{L1}}\right)d\mathcal{V}, \quad (3.39)$$

$$\mathbf{K_G} = \int_{\mathcal{V}} \mathbf{B_{NL}}^{\mathsf{T}}\mathbf{D}\mathbf{B_{NL}}d\mathcal{V}. \quad (3.40)$$

and

$$\mathbf{S}^0 = \begin{bmatrix} \tilde{S}^0 & \tilde{0} & \tilde{0} \\ \tilde{0} & \tilde{S}^0 & \tilde{0} \\ \tilde{0} & \tilde{0} & \tilde{S}^0 \end{bmatrix} \qquad \tilde{0} = \begin{bmatrix} 0 & 0 & 0 \\ 0 & 0 & 0 \\ 0 & 0 & 0 \end{bmatrix}$$

$$\tilde{S}^0 = \begin{bmatrix} S^0_{11} & S^0_{12} & S^0_{13} \\ S^0_{21} & S^0_{22} & S^0_{23} \\ S^0_{31} & S^0_{32} & S^0_{33} \end{bmatrix}$$

One can refer to [8] for matrices $\mathbf{B}$ because they are related to the chosen finite element interpolation.

As already stated, there are three contributions to the internal work: the *linear stiffness* $\mathbf{K}$, which is the common stiffness in small deformation and small displacement problems, the so-called *geometric stiffness* $\mathbf{K_L}$, which is related to the deformed shape in the reference condition, and the *prestress stiffness* $\mathbf{K_G}$, which is related to the stress field in the reference configuration.

3.5 NUMERICAL PROCEDURES

The main solver work-flow is:

1. Assembly and factorization of various matrices;
2. Trim with centrifugal loads;
3. Compute the *prestrain and stress stiffness* matrix (with the displacement field just calculated);
4. Solve the eigenproblem (frequencies and modes) with and without the Coriolis damping matrix;
5. Build the reduced system;

The first four points will be carried out in a commercial software, i.e. *NASTRAN®* and *ANSYS®*. The approach of the two commercial software is documented in [62] and [3] respectively. Examples of a proper use of various parameters are reported in chapter 6.

3.5.1 Building, assembly and factorization of various matrices

The solver has to build these matrices to perform calculations:

$$\text{Mass matrix : } \mathbf{M} = \int_{\mathcal{V}} \mathbf{N}^{\mathrm{T}} \rho \mathbf{N} \mathrm{d}\mathcal{V}, \tag{3.41}$$

$$\text{Elastic stiffness matrix : } \mathbf{K_e} = \mathbf{K} + \mathbf{K_L} = \int_{\mathcal{V}} \left(\mathbf{B_{L0}} + \mathbf{B_{L1}}\right)^{\mathrm{T}} \mathbf{D} \left(\mathbf{B_{L0}} + \mathbf{B_{L1}}\right) \mathrm{d}\mathcal{V}, \tag{3.42}$$

$$\text{Centrifugal stiffness matrix : } \mathbf{K_C} = \int_{\mathcal{V}} \mathbf{N}^{\mathrm{T}} \rho \left(\bar{\boldsymbol{\omega}} \bar{\boldsymbol{\omega}} \mathbf{N}\right) \mathrm{d}\mathcal{V}, \tag{3.43}$$

$$\text{Coriolis damping matrix : } \mathbf{C_C} = \int_{\mathcal{V}} \mathbf{N}^{\mathrm{T}} \rho \bar{\boldsymbol{\omega}} \mathbf{N} \mathrm{d}\mathcal{V}, \tag{3.44}$$

and this vector

$$\text{Steady centrifugal load vector : } \mathbf{F_C} = \int_{\mathcal{V}} \mathbf{N}^{\mathrm{T}} \rho \bar{\boldsymbol{\omega}} \bar{\boldsymbol{\omega}} \mathbf{R} \mathrm{d}\mathcal{V}$$

Ref.[74] reports a simple form of some terms if a lumped mass matrix is used. The rigorous definition of eq.(3.41) produces a *coupled* mass matrix, but the *lumped* (diagonal) mass matrix can be obtained by appropriately distributing the elements mass to each node.

In particular, one can redefine:

$$\begin{aligned} \mathbf{K_C} &= \tilde{\boldsymbol{\Omega}} \mathbf{M} \tilde{\boldsymbol{\Omega}}, \\ \mathbf{C_C} &= 2 \tilde{\boldsymbol{\Omega}} \mathbf{M}, \\ \mathbf{F_C} &= \tilde{\boldsymbol{\Omega}} \mathbf{M} \tilde{\boldsymbol{\Omega}} \{x_n\}, \end{aligned} \tag{3.45}$$

where

$$\tilde{\Omega} = \begin{bmatrix} \bar{\omega} & & & 0 \\ & \bar{\omega} & & \\ & & \ddots & \\ 0 & & & \bar{\omega} \end{bmatrix}$$

and $\{x_n\}$ contains the nodal coordinates.

3.5.2 Trim with centrifugal loads

The trim determines the static deformed shape due to centrifugal loads, obtained by eq.(3.45). This implies the resolution of system

$$\tilde{K}(u)\, u = F_C, \tag{3.46}$$

to establish nodal displacements u due to applied loads. The matrix $\tilde{K}$ depends on the approach chosen between *Updated* or *Total* Lagrangian. Only the treatment of the former approach is here provided.

The small displacement approximation is well acceptable for open rotors dynamics; the blades being quite rigid (specially those in composite materials) and angular velocities not so high. So, the deformed shape does not differ significantly from the undeformed one. From trim analyses conducted, it can be observed that the blade stretches itself along the radial direction in order to minimize the distance of any material point from the plane of rotation.

Even if the small displacement assumption is legitimated, the trim calculation is performed as non linear static analysis (i.e. SOL 106 in NASTRAN or NON-LINEAR ANALYSIS in ANSYS) in order to be conservative. The procedure depends on the chosen approach because that implies different representations for strains and stresses. In the case of the *Updated* Lagrangian approach, tab.(1) reports the tensors employed for representing the strain and stress fields.

	U.L.
Stress	Cauchy Stress Tensor (τ)
Strain	Cauchy Strain Tensor (ε)

Table 1: U.L. strain and stress tensors

Using a variable "t" to identify the different body configurations, in [8] is reported

$$\left({}^{t}_{t}K_L + {}^{t}_{t}K_N L\right) \Delta U = {}^{t+\Delta t}\, Res - {}^{t+\Delta t}_{t}\, F, \tag{3.47}$$

where

$$
\begin{aligned}
{}^{t}_{t}\mathbf{K_L} &= \int_{{}^{t}V} {}^{t}_{t}\mathbf{B_L}^{T}\, {}_{t}\mathbf{D}\, {}^{t}_{t}\mathbf{B_L}\, {}^{t}d\mathcal{V}, \\
{}^{t}_{t}\mathbf{K_{NL}} &= \int_{{}^{t}V} {}^{t}_{t}\mathbf{B_{NL}}^{T}\, {}^{t}_{t}\mathbf{S}\, {}^{t}_{t}\mathbf{B_{NL}}\, {}^{t}d\mathcal{V}, \\
{}^{t}_{t}\mathbf{F} &= \int_{{}^{t}V} {}^{t}_{t}\mathbf{B_L}^{T}\, {}^{t}_{t}\hat{\boldsymbol{\tau}}\, {}^{t}d\mathcal{V}.
\end{aligned}
$$

So, eq.(3.46) becomes an iterative problem as

$$
\tilde{\mathbf{K}}\Delta\mathbf{U}^{(i)} = \mathbf{Res} - \mathbf{F}^{(i-1)}, \tag{3.48}
$$

in which displacements are obtained when the right-hand-side is lower of a user-defined tolerance.

3.5.3 Building the *prestress stiffness* matrix

With the displacement field just calculated, the matrix of eq.(3.40) is

$$
\mathbf{K_G} = \int_{\mathcal{V}} \mathbf{B_{NL}}^{T}\mathbf{D}\mathbf{B_{NL}}\, d\mathcal{V}. \tag{3.49}
$$

3.5.4 Eigenproblem: frequencies and modes

The eigenproblem solved for this analysis is

$$
-\omega^2\mathbf{M}\Delta\mathbf{q} + (\mathbf{K_e} + \mathbf{K_G} + \mathbf{K_c})\,\Delta\mathbf{q} = 0, \tag{3.50}
$$

where appear both centrifugal stiffness $\mathbf{K_G}$ and centrifugal softening $\mathbf{K_C}$ terms.

3.5.5 Building the reduced system

With modes just calculated, the complete reduced system is

$$
\mathfrak{M}\ddot{\boldsymbol{\beta}} + \mathfrak{C}\dot{\boldsymbol{\beta}} + \mathfrak{K}\boldsymbol{\beta} = 0, \tag{3.51}
$$

where

$$
\begin{aligned}
\mathfrak{M} &= \mathbf{X}^{T}\mathbf{M}\mathbf{X} \\
\mathfrak{C} &= \mathbf{X}^{T}\mathbf{C_c}\mathbf{X} \\
\mathfrak{K} &= \mathbf{X}^{T}\mathbf{K}\mathbf{X}.
\end{aligned}
$$

The size of the reduced model depend on the level of approximation required. In aeroelastic analysis, few modes can often describe the structural subsystem fairly well. This model condensation is very useful to efficiently conduct flutter calculations.

4

INTERFACE

4.1 BACKGROUND

Given a fluid and structural system, in principle one can directly write down the system of Partial Differential Equations (PDEs) governing the coupled FSI problem and then try to discretize it as a whole. However, this approach, usually denominated *monolithic* is hardly ever used because the numerical model attaining each physical domain has different mathematical and numerical properties, along with quite peculiar software implementation requirements. The other approach, called *partitioned* and often followed in practice, is based on the Domain Decomposition paradigm. The basic idea is to develop specialized methods to solve each field independently, or better to resort to existing, well-established numerical techniques for each discipline. So, to solve a coupled fluid structure problem it is not sufficient to be able to compute the solution of the structural and of the aerodynamic model separately, it is also necessary to exchange information between them: the modification of boundary conditions must be transferred from the deformable structure to the aerodynamic boundary, and conversely, the loads developed by the aerodynamic field must be applied to the discrete structural model. The way of using the information exchange during a time integration or a frequency domain simulation gives rise to further distinctions in the class of partitioned methods among explicit or implicit coupling, *loose* or *strong* coupling.

In addition, to exploiting the large experience gained in the development of solvers for each field, the partitioned approach allows another important freedom: the possibility of using *non-compatible* discretizations, such as different discretization size and element types, e.g. beam elements for structures and flat lifting surfaces for the aerodynamics, fig.(**??**). Of course in all these cases the responsibility of a correct information transfer is left to an *interface scheme*, which must interpolate/extrapolate the data in an appropriate manner. The problem of building a methodology to couple fluid and structure has always been a key aspect of aeroelastic methods.

The main properties that must be ideally satisfied by an interface algorithm are:

- the possibility of interfacing both non-matching surfaces and/or topologies;

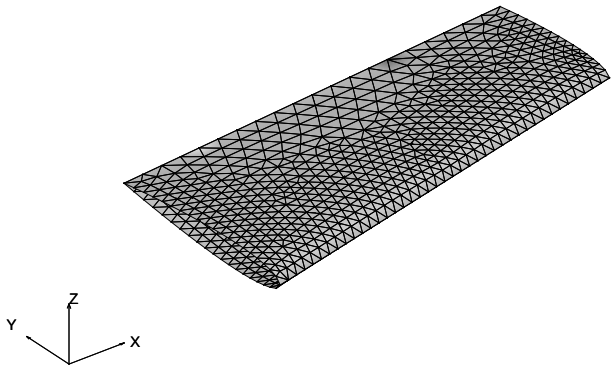

(a) Body Surface Mesh of a Wing for Euler Calculation.

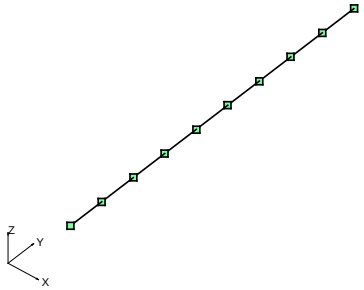

(b) Lifting Line.

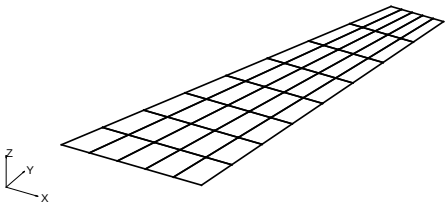

(c) Vortex Lattice.

Figure 17: fig:Different Aerodynamic Models

- the capability of dealing with situations where a control point falls outside the range of the source mesh (extrapolation);
- the efficiency of the interface operator computation and use;
- the exact treatment of rigid translations and rotations;

- the capability to correctly deal with situations presenting widely differing node densities;
- the independence from the numerical formulation of the Computational Fluid Dynamics (CFD) and Computational Structural Dynamics (CSD) solvers;
- the conservation of appropriate exchanged physical quantities (in particular momentum and energy);
- the possibility of controlling the smoothness of the resulting surface;
- an easy evaluation of the new interface operator in case of mesh adaptation, either in the source or target grids.

4.2 STRUCTURAL SUB-SYSTEM

In the framework of Ritz's like numerical methods, the unknown deformable structural displacement field $\mathbf{s}(x,t)$ is represented as a function of a complete set of space dependent shape functions $N_i(x)$ and a set of time dependent generalized displacements $q_i(t)$,

$$\mathbf{s}(x,t) \simeq \sum_{i=1}^{n_s} N_i(x) q_i(t) = \mathbf{N}(\mathbf{x})\ \mathbf{q}(\mathbf{t}). \tag{4.1}$$

Such an approach translate the structural problem to a system of ODEs, eq.(3.51),

$$\mathcal{M}\ddot{\mathbf{q}}(t) + \mathcal{C}\dot{\mathbf{q}}(t) + \mathcal{K}\mathbf{q}(t) = \mathcal{Q}_a(t) \tag{4.2}$$

where $\mathcal{M}$, $\mathcal{C}$ and $\mathcal{K}$ are the generalized mass, damping and stiffness matrices. The array of the Generalized Aerodynamic Forces (GAFs) $\mathcal{Q}_a(t)$ is assembled by projecting the aerodynamic pressure field acting on the body surface S onto the structural shape functions,

$$\mathcal{Q}_a(t) = q_\infty \int_S C_P(\mathbf{x},t)\, \mathbf{N}(\mathbf{x})^T\, \vec{n}\ dS \tag{4.3}$$

To solve the structural problem the set of shape functions $N_i(x)$ and the number of structural degree of freedom n_s must be chosen. The compact support Lagrange polynomial shape functions of the Finite Element Method (FEM) can be used. So, the generalized displacements $q_i(t)$ become the nodal displacements $\vec{u}_s$. However, for such a formulation, the number of degrees of freedom n_s needed to obtain an acceptable accuracy is generally too large. Alternatively, the set of shape functions can be obtained by means of an appropriate modal condensation, be it through static or vibration modes, often validated through Ground Vibration Tests (GVTs). Because of the favourable convergence properties of such shape functions a relatively limited number of degrees of freedom is often sufficient to build an accurate and efficient condensed numerical model of the structural sub-system.

4.3 FLUID–STRUCTURE COUPLING

The aeroelastic interface scheme can be represented by means of a linear operator $\mathbf{L}$ which suitably interpolates the structural displacements $\mathbf{u}_s$ onto the aerodynamic boundary nodes displacements $\mathbf{u}_a$,

$$\mathbf{u}_s = \mathbf{L}\,\mathbf{u}_a \tag{4.4}$$

As said, a successful aeroelastic interface scheme must link models with non-matching spatial domains and numerical grids, while ensure the conservation of the momentum and energy exchanged between the two sub-systems. The introduction or removal of spurious values through the interface scheme may affect the overall stability properties of the aeroelastic system.

Such a property can be translated on the equivalence of the virtual work made by the aerodynamic forces $\mathbf{F}^{aero}$ on the two sub-systems,

$$\delta\mathcal{L} = \delta\mathbf{u}_a\,\mathbf{F}_a^{aero} = \delta\mathbf{u}_s\,\mathbf{F}_s^{aero}. \tag{4.5}$$

Substituting eq.(4.4) in eq.(4.5) we obtain the linear operator which interpolates the aerodynamic forces from the aerodynamic to the structural system,

$$\mathbf{F}_s^{aero} = \mathbf{L}^T\,\mathbf{F}_a^{aero} \tag{4.6}$$

4.3.1 Moving Least Squares

The aeroelastic interface operator of eq.(4.4) is here built by means of an interpolation scheme based on a Moving Least Squares (MLS) technique [14, 56]. Such a scheme is able to deal with complex configurations and extremely different structural and aerodynamic meshes. A local approximation of the structural displacement field must be built by means of a sum of n polynomial basis functions,

$$\tilde{u}_s(\mathbf{x}) = \sum_{k=1}^{n} f_k(\mathbf{x})\,a_k, \tag{4.7}$$

where $f_k(\mathbf{x})$ is the k-th basis function while a_k is the k-th unknown coefficient. The coefficients a_k are obtained by performing a weighted least square fit for the approximation:

$$\text{Minimize} \qquad J(\mathbf{x}) = \int_\Omega W(\mathbf{x}-\bar{\mathbf{x}})\,(\tilde{u}_s(\mathbf{x}) - u_s(\bar{\mathbf{x}}))\,d\Omega(\bar{\mathbf{x}}) \tag{4.8}$$

The problem can be localized by choosing compact support weight functions $W(\mathbf{x})$ such as smooth non-negative Radial Basis Functions (RBF). The type of function and the support radius must be chosen to obtain a smooth interpolation and to cover enough structural nodes. As an example of the robustness and quality of the MLS scheme, the reconstruction onto the aerodynamic boundary mesh of a deformable

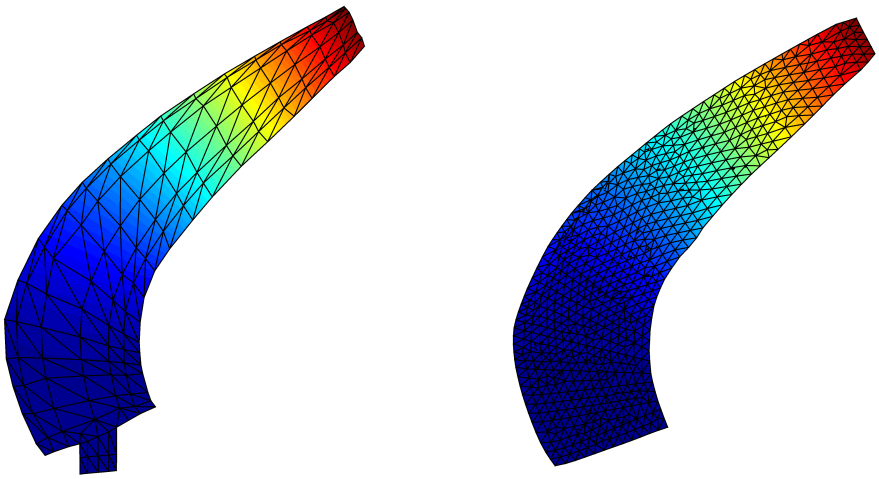

Figure 18: MLS interface for SR-3 propfan blade. The left-hand image is the structural mesh for FEM analysis (SHELL elements). The right-hand image is the aerodynamic mesh for FV analysis.

modal shapes of the FE structural model of SR-3 propfan blade [21] is shown in fig(18).

The first modal shape is shown in fig.(18). It can be observed a good representation of the modal displacement onto the aerodynamic boundary mesh.

4.4 TRANSPIRATION BOUNDARY CONDITION

By using an appropriate interface scheme, the displacement and velocity vector of the structural points, $\mathbf{u}_s(t)$ and $\dot{\mathbf{u}}_s(t)$, can be interpolated onto the aerodynamic points of the body surface, $\mathbf{u}_a(t)$ and $\dot{\mathbf{u}}_a(t)$. There are various way to impose a variation of boundary conditions on the body surface. The most expensive, but conceptually exact method, consists in deforming the aerodynamic mesh. The *Arbitrary Lagrangian-Eulerian* (ALE) formulation allows this approach. The grid can be seen as a deformable continuum, with its own stiffness matrix, where an imposed displacement field is given onto its boundaries. In particular, the far field boundary is constrained with no motion while its part adjacent to the the body one reproduces the desired deformed shape. At each time step, the numerical fluxes vector is updated with its interface velocity contributions [50].

A simpler technique can be exploited after remembering that flutter analyses corresponds to studying the stability properties of a time invariant linearised aeroelastic system, assuming small displacements around a steady equilibrium condition. A more efficient strategy consists in modifying the boundary conditions on the body without deforming the aerodynamic mesh. The normal speed V_n, called *tran-*

spiration velocity, is added to the non penetration boundary condition onto the body in order to include geometric and kinematic effects of moving boundaries.

4.4.1 Linearised Formulation

Referring to sec.(2.4), the condition of non penetration $(\boldsymbol{v} \cdot \vec{n})\big|_{S^b} = 0$, where S^b is the body surface, has to be imposed. Thus, the local velocity and the surface normal vector in the deformed configuration have to be found. The non-penetration condition can be linearised as

$$\begin{aligned}(\boldsymbol{v} \cdot \vec{n})|_{S^b} &= (-\boldsymbol{V}_\infty + \dot{\boldsymbol{s}}) \cdot (\vec{n}_0 + \Delta\vec{n}) \\ &= -\boldsymbol{V}_\infty \cdot \vec{n}_0 - \boldsymbol{V}_\infty \cdot \Delta\vec{n} + \dot{\boldsymbol{s}} \cdot \vec{n}_0 + \mathcal{O}(\boldsymbol{s}^2),\end{aligned} \tag{4.9}$$

where $\boldsymbol{V}_\infty$ is the asymptotic velocity, $\dot{\boldsymbol{s}}$ is the deformation velocity of the body surface, $\vec{n}_0$ is the undeformed normal vector and $\Delta\vec{n}$ is the variation of the normal vector due to body deformation. At each time step, the variation of the normal vector $\Delta\vec{n}$ is calculated with a finite difference between the undeformed and the deformed normal vectors.

In eq.4.9, there are 3 contributions:

1. The equilibrium contribution $\boldsymbol{V}_\infty \cdot \vec{n}_0$;
2. The *geometric* contribution proportional to the surface displacement (related to $\Delta\vec{n}$);
3. The *kinematic* contribution proportional to the displacement velocity $\dot{\boldsymbol{s}}$ on the body surface.

So, the normal velocity V_n that modify the body boundary condition is

$$V_n = -\boldsymbol{V}_\infty \cdot \Delta\vec{n} + \dot{\boldsymbol{s}} \cdot \vec{n}_0. \tag{4.10}$$

The additional contribution to fluxes vector, $\mathbf{F}^{tra}$, is:

$$\mathbf{F}^{tra} = \int_{S_b} \rho V_n \, dS_b. \tag{4.11}$$

The previous equation exploits the *superposition principle*, so the geometric contribution can be considered separately from the kinematic one. It can be observed that the geometric contribution is predominant at regime, while the kinematic one has effect only during the transient. As explained in [47], the aerodynamic transfer matrix can also be separated in its geometric part $[H^G_{am}(k)]$ and in its kinematic part $[H^C_{am}(k)]$ (both matrices are complex):

$$[H_{am}(k)] = [H^G_{am}(k)] + jk\,[H^C_{am}(k)]. \tag{4.12}$$

4.4.2 Non Linear Formulation

Keeping the second order terms of eq.(4.9), the non linear expression of the normal transpiration velocity, V_n, is

$$V_n = -\boldsymbol{V}_\infty \cdot \Delta\vec{n} + \dot{\boldsymbol{s}} \cdot \vec{n}_0 + \dot{\boldsymbol{s}} \cdot \Delta\vec{n}. \tag{4.13}$$

If structural velocities are small, then the normal transpiration velocity, V_n, becomes linear because the term $\dot{\boldsymbol{s}}$ is smaller than the *geometric* contribution related to $\boldsymbol{V}_\infty$.

Although eq.(4.13) is not consistent with the linearised formulation presented in sec.(4.4.1), the non linear expression of V_n, eq.(4.13), has an improved range of application in terms of Mach M_∞, angle of attack α and thickness t/c respect to the linear formulation of eq.(4.9) [58].

4.5 BOUNDARY CONDITION FOR CONTRA ROTATING BLADE ROWS

This section explains the numerical technique needed to simulate the flow field around two contra-rotating bodies. The formulation of eq.s (2.40),(2.41),(2.42),(2.43) and (2.44) closes the mathematical problem related to the simulation of the flow field around a single rotor. A slight extension of the code is required to deal with two contra-rotating rotor.

The most common strategy so far adopted to simulate the flow field around different bodies with relative motion is the *Chimera* method [15]. However, the implementation of such technique is far away from the scope in this work.

An alternative strategy consists in simulating the flow field with non-inertial Multiple Reference of Frame (MRF) combined with ALE scheme for the translational motion [10]. Given the rotor angular velocity of a particular domain region, the centrifugal and Coriolis forces can be directly added to the right hand side of the Navier-Stokes or Euler equations, as explained in sec.(2.1). Moreover, Mixing Planes (MPs) are required at the interfaces between regions with different angular velocities. Nevertheless, the MP approach cannot be exploited for a full potential solver because the discontinuity of the potential function (i.e. the wake vorticity) cannot be rigorously transferred through the interfaces between various regions. In particular, within the frame of CROR, the second rotor may run into the wake surfaces generated by the first one. Thus, the mesh generation may become a very hard issue if wake-wake or body-wake intersections have to be accounted for. Obviously, these complications make it difficult a correct mesh generation. Fig.(19) shows the various vortex interactions in CRORs.

In order to overcome these issues, an *ad hoc* technique is developed and it is based on *ghost bodies* and transpiration boundary conditions.

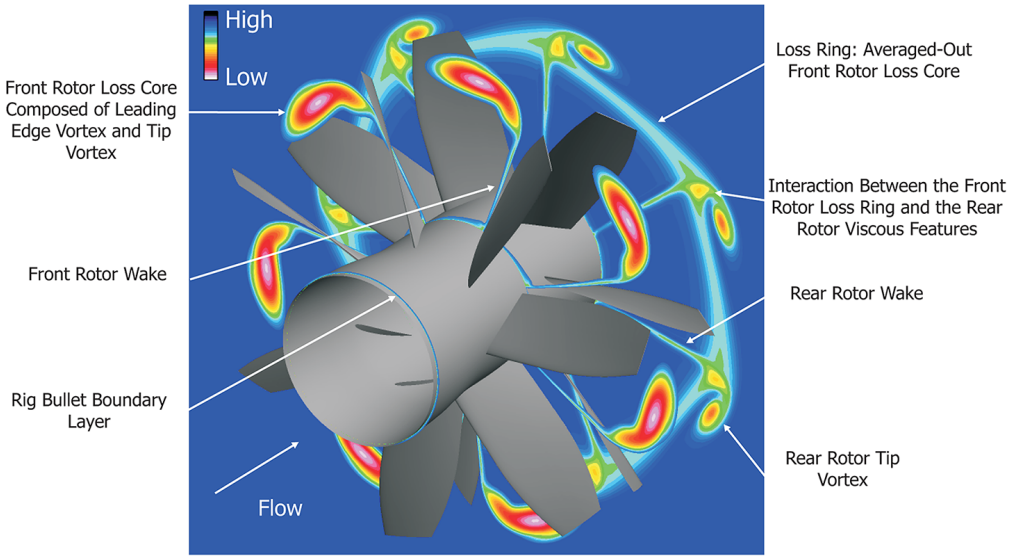

Figure 19: Vortexes interaction in CRORs. [73]

Such a technique simplifies the regions interfacing and prevents the difficulties related to the mesh generation related to the wake-wake or body-wake intersections.
It has to be noted that most of the designed CROR are provided with a different number of blades and different blade shapes between the two stages. The blades often differ only in size: the forward rotor has a bigger diameter than the aft rotor, so that tip vortexes generated by the first stage do not impact onto the blades of the second stage. The number of blades differs in order to reduce aerodynamic load oscillations; in common configurations, the front rotor has 10 blades, while the rear rotor has 8. Actually, for the sake of simplicity, two hypothesis are made:

- The two rotor stages have the same number of blades;
- The blades geometry of the two stages is identical.

Both assumptions allow to re-use the grid for a single blade (with its own wake discretization) for contra-rotating simulations.

The time-marching simulation is replicated in the same number as the propeller stages. In particular, two simulations connected by the the transpiration boundary condition are processed in parallel. When simulating the front rotor, the location of the downstream stage in the primary grid is represented by the rear ghost. The velocity potential $\phi(\mathbf{x}, t)$ and density $\rho(\mathbf{x}, t)$ fields are evaluated onto the rear ghost contour. Such fields are used to alter the boundary conditions onto the rear stage of the other simulation with a technique very similar to the transpiration boundary condition (see next section). Vice-versa, when simulating the rear rotor, the location of the upstream stage in the primary grid is represented by the front ghost. The velocity potential

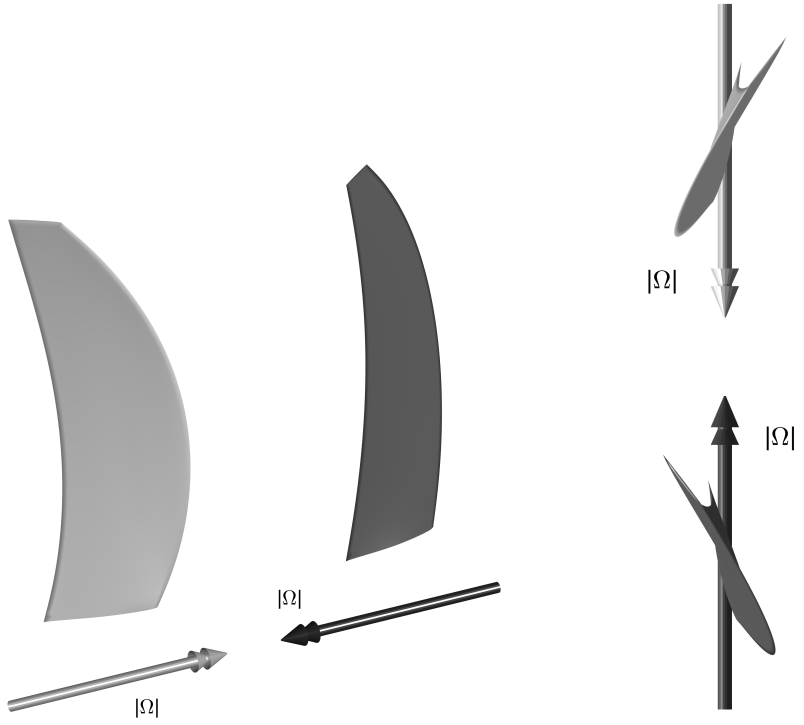

Figure 20: Relative motion between the two rotor blades. In the first simulation, the meshed blade is the black one, while the ghost (gray) is located downstream.

$\phi(\mathbf{x}, t)$ and density $\rho(\mathbf{x}, t)$ fields are evaluated onto the front ghost contour. Such fields are used to alter the boundary conditions onto the front stage of the other simulation.

Since the the ALE scheme is exploited and the two rotors counter rotate, the real body (black) is fixed while the ghost (gray) rotates with a doubled angular velocity which have opposite versus in the two parallel simulations. Thus, it is possible to define the angle

$$\Psi = \mathrm{reminder}\left(\frac{2\,|\Omega|\,t}{\frac{2\pi}{N_b}}\right), \tag{4.14}$$

as depicted in fig(21). The angle Ψ is constrained between $0\ \mathrm{rad}$ and $\frac{2\pi}{N_b}\ \mathrm{rad}$, where N_b is the number of blades of both stages, in order to employ periodic boundary conditions. Thus, the gray blade starts its rotation behind|above the black one (i.e. $0\ \mathrm{rad}$) and come back in this position after a rotation of $\frac{2\pi}{N_b}\ \mathrm{rad}$, fig.(21).
The solution of each simulations is replicated as shown in fig.(21) so to evaluate the density and velocity potential fields at the ghost location even when the ghost go through the periodic boundary.

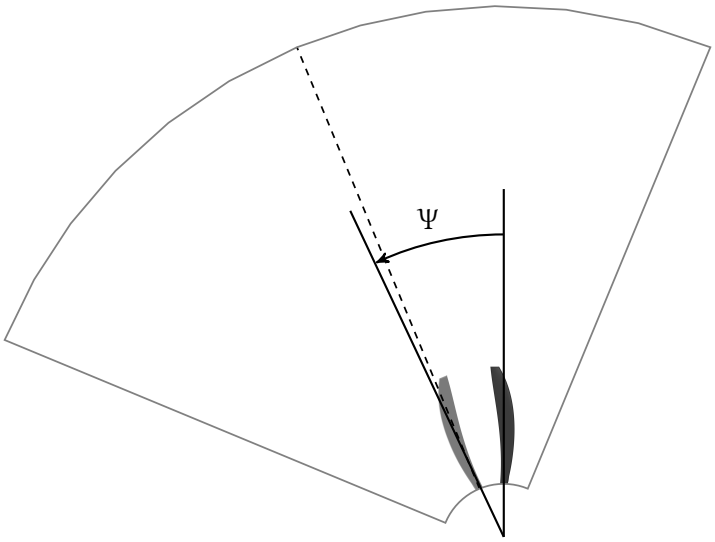

(a) Ψ angle in the first simulation.

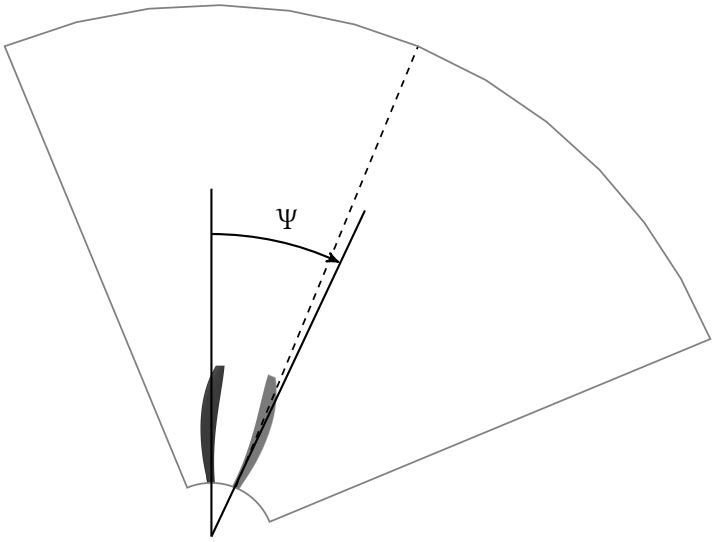

(b) Ψ angle in the second simulation.

Figure 21: Visualization of the Ψ angle in both cases.

The superposition of the solutions of the two simulations provides the real flow field around the two lifting bodies at a particular time step. The validity of this technique relies upon the *superposition principle*. Unfortunately, the compressible aerodynamics is not linear but the (ab)use of the superposition principle gives good results if the coupling between the two lifting bodies can be described as a linear function. Appendix A shows also the range of validity and the limitations of this technique for a simple 2D case.

4.5.1 Boundary Conditions on the Real Body

The boundary conditions on the real body (i.e. the black one in previous figures) is slightly different from the simple case because another contribution has to be added. The condition of non-permeability of solid boundaries is always correct but the perturbation introduced by the *ghost* has to be taken into account. Now, the density flux at the solid boundaries of eq.(2.56) counts for another term:

$$F_{body} = \int_{\Gamma_b} (\rho_0 + \Delta\rho)\mathbf{V}_G \cdot \vec{n} d\Gamma_b. \tag{4.15}$$

Where $\rho_0(\mathbf{x}, \bar{t})$ is the density field evaluated onto the real body at time $\bar{t}$, while $\Delta\rho(\mathbf{x}, \bar{t} - dt)$ is the perturbation of the density field calculated onto the *ghost* body at the previous time step. This new term is useful to accelerate the convergence of the solution when using the so called *ghost* technique. In this way, a better representation of the density field around the body can be obtained.

4.5.2 Transpiration Boundary Condition

The transpiration technique can still be used when simulating the flow field around contra-rotating open rotors with small blades deformations. Obviously, the normal velocity contribution is the same as eq.(4.13) but a *perturbed* density field has to be considered when calculating the boundary condition onto the body surface. So, eq.(4.11) becomes

$$F^{tra} = \int_{\Gamma_b} (\rho_0 + \Delta\rho)V_n d\Gamma_b. \tag{4.16}$$

It should be immediately observed that the front and aft rotor can have different motions, e.g. when the aerodynamic transfer functions are calculated (see cap.(5)).

5

FLUTTER ANALYSIS

A flutter analysis is the study of the stability properties of an aeroelastic system linearized around a reference condition. Thus, the flutter analysis concerns the study of the system eigenvalues. In particular, a flutter occurs when a structural eigenvalue reaches a zero-damping condition due to the interaction with the surrounding fluid, the linearization around a reference condition being the key to the study of the stability properties. The hypothesis of linearity (locally at least) of the aeroelastic system is crucial to reduce the computational costs. In transonic flow aerodynamic non-linearities tend to be the most important. Indeed, it is often observed that the transonic flow regime is inherently non-linear in the governing field equations. Performing a flutter analysis in these circumstances is not a simple task.

This chapter provides the theoretical background for rotor flutter analysis. Sec.(5.1) introduces the main features of the rotor aeroelasticity. Sec.(5.2) is focused onto the identification of the aerodynamic transfer functions $\mathbf{H_{am}}(k, M_\infty)$ with a time-based aerodynamic solver so performing the stability analyses in the frame of classical aeroelasticity. Various methods for calculating the eigenvalues of the aeroelastic system are described in sec.(5.3).

5.1 ROTOR AEROLEASTICITY

The simplest (and most physical) way to represent the aero-structural behaviour of a rotor is to describe the motions of all blades, especially when (as it usually happens) the disk is assumed to be rigid and blades are thus independent single structures which interact with each other due to aerodynamic loads. The motion of one blade generates unsteady loads on the neighbouring blades and these in turn affect the reference one with a linear superposition (for small perturbation theory) of forces which arise from the same kind of motion. Ref.[37] exploited the inherent cyclic symmetry of the problem to prove that a dramatic reduction in the number of system variables is rigorous for linear analysis and actually the same approach is effective even for non-linear phenomena (e.g. stall flutter).
It can be inferred that the perturbations affecting the reference blade (i.e. "0" in fig.(22)) do not act simultaneously but with a precisely shift in time. So, in the field of aeroelastic analysis, more complex periodic boundary conditions must be introduced in order to correctly

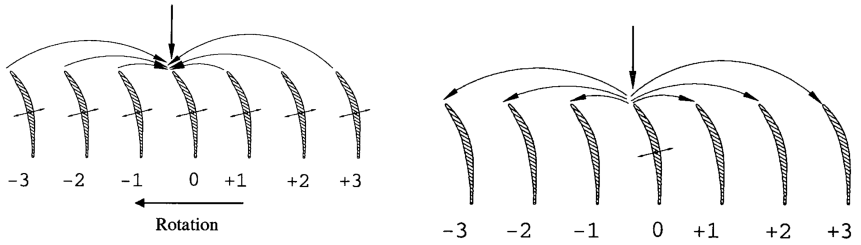

Figure 22: Physical explanation of influence coefficients [71]

represent the lag of the perturbations coming from the motion of other blades if a reduced aerodynamic sub-system is modelled. Thus, ref.[37] introduced the concept of the *Inter Blade Phase Angle* (IBPA), defined as

$$\sigma = \frac{2\,\pi}{N_b}, \tag{5.1}$$

which is an important parameter in rotor aeroelasticity (along with the more traditional reduced frequency $k = \frac{\omega\, L_a}{V_\infty}$). The IBPA is the non-dimensional spatial frequency of a periodic disturbance that travels circumferentially down-rotor or up-rotor from blade to blade. The allowable N_b discrete IBPA values are:

$$\sigma_n = \frac{2\pi\, n}{N_b}, \qquad \text{with} \quad n = 0, 1...N_b - 1 \tag{5.2}$$

or alternatively from $-\pi$ to $\pi - \frac{2\pi}{N_b}$ and the positive values are associated to forward (in the direction of rotation) travelling waves, while the negative values are associated to backward travelling waves. In this way, all blades are equal to each other due to cyclic symmetry and they vibrate harmonically with the same frequency but with a time-lag phase angle σ which is constant and uniform from blade to blade. Thus, the phase angle divided by the angular speed of the perturbation is the characteristic time lag of the disturbance in a blade passage

$$\Delta T = \frac{\sigma_n}{\Omega}. \tag{5.3}$$

In this way, the simulations for different phase angles σ_n require phase-lagged periodic boundary conditions exploiting the reduction of the computational domain to a single blade passage only.
The implementation of this phase lag is actually complex and computationally expensive if the simulations are done in the time domain. The simplest solution is to transform the simulations in the frequency domain because the time shift can be applied easily and it is not constrained to assume the discrete values of σ_n. Such a solution is not exploited in this work but it is a future development to be adopted for a better flutter analysis of CROR.

Another solution consists in modelling more blade passages by exploiting the fact that the blade-to-blade phase angle is constant and

uniform and therefore after a certain number of passages the total time-shift (with respect to a reference blade) returns to zero and a perfect spatial periodicity is recovered. For example if the blades are assumed to vibrate at a given frequency but are 180° out of phase the computational domain requires two blades (or passages); four blades allow to model $\sigma = \pm 90°$, eight blades for $\sigma = \pm 45°$ or $\sigma = \pm 135°$ and so on.

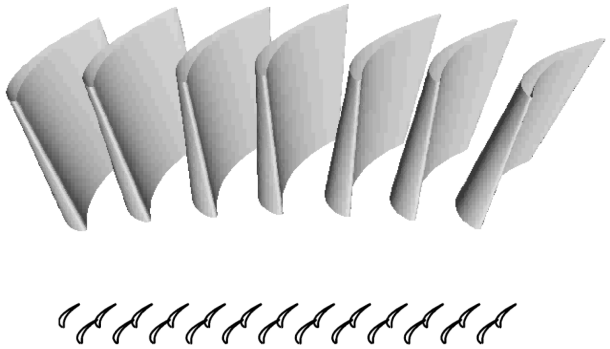

Figure 23: A bending vibration with $\sigma_n = 180°$ of turbomachines blades is here represented. It can be inferred that the perturbations are periodic every two blade passages. [68]

This still decreases the size of the mesh compared to modelling the whole rotor but it does not allow to rigorously treat flows featuring a generic time-lag which is not associated to a specific phase angle σ_n. However, this solution cannot be of help because the modelling of more blade passages requires computational capabilities that cannot be reached with the resources available for the present work.
In conclusion, the flutter analysis here carried out are done only for a 0° IBPA. Although the analysis are not complete, the partial results obtained can give a basic idea of the stability of the studied systems.

For further details and for an improved treatment of rotor aeroelasticity, ref.[19] presents an overall vision on the various techniques adopted in the linearised flutter analysis of turbomachines (which are very similar to those of a CROR).

5.2 AERODYNAMIC TRANSFER FUNCTION

The definition of the aerodynamic forces acting on the structural sub-system is crucial for aeroelastic analyses. As said with a proper representation of the unsteady boundary condition, the aerodynamic transfer functions matrix $\mathbf{H_{am}}(k, M_\infty)$ can be evaluated directly in the Laplace domain. However, such an approach can involve undue computational costs using non-linear aerodynamic models because a precise evaluation of the aerodynamic Jacobian matrix must be performed at each desired steady state. So, the matrix $\mathbf{H_{am}}(k, M_\infty)$ is here obtained through numerical time marching simulations. At first, the

steady solution for the aeroelastic system, i.e. the trimmed deformed condition representing the reference trim condition for the linearization, must be reached. Now the vector of the generalized aerodynamic forces $\mathbf{Q}_a(t)$ due to a prescribed law of motion of the i-th generalized displacement $\mathbf{q}_i(t)$ can be computed. The i-th column of the aerodynamic transfer functions matrix $\mathbf{H_{am}}(k, M_\infty)\big|_i$ is the ratio between the Fourier transform of the output and input signal of the aerodynamic system,

$$\mathbf{H}_{am}(k, M_\infty)|_i = \frac{\mathcal{F}(\mathbf{Q}^a(t))}{\mathcal{F}(\mathbf{q}^i(t))} \tag{5.4}$$

where the operator $\mathcal{F}(\circ)$ can be efficiently implemented by the Fast Fourier Transform (FFT) algorithm. Performing such an operation for each structural degree of freedom the whole aerodynamic transfer functions matrix $\mathbf{H_{am}}(k, M_\infty)$ is obtained. It is worthwhile to remark that each column of the aerodynamic transfer functions matrix can be computed independently.

The procedure is computationally efficient due to the use of the transpiration to impose the unsteady boundary conditions. The law of motion for the i-th generalized displacement $q^i(t)$ must excite the desired reduced frequency range $[0, k_{max}]$. Defining ω as the frequency of the vibrational motion of the structure, c as a reference length and V_∞ as the asymptotic velocity, the definition of the reduced frequency k is:

$$k = \frac{\omega\, c}{V_\infty}, \tag{5.5}$$

and k_{max} can be safely assumed to be five, at most. Moreover, the amplitude of the displacement must be large enough to overcome the numerical noise but not too large to preserve the small perturbation hypothesis. Moreover the programming effort and computational overhead associated with the numerical implementation of such an input signal must be taken into account. The most widely used options are: harmonic, impulse, step. The characterization through harmonic input seems the most natural but it is extremely expensive in terms of computational costs, because each degree of freedom needs to be tested for a set of imposed frequency. The other two cases, at least ideally, require just one test for each input to characterize completely the system in the whole range of frequencies of interest. The better choice is likely a blended step input, namely:

$$q^i(\tau) = \begin{cases} \frac{A_q}{2}\Big(1 - \cos(k_q \tau)\Big) & \text{if } \tau < \tau_q, \\ A_q & \text{if } \tau \geqslant \tau_q, \end{cases} \tag{5.6}$$

where the non-dimensional time $\tau = \frac{t\, V_\infty}{c}$ can be interpreted as the number of aerodynamic reference lengths travelled per unit time at

the flight velocity V_∞. Remembering this substitution of variables, the corresponding time derivative $\dot{q}^i(\tau)$ can be written

$$\dot{q}^i(t) = \frac{dq^i(\tau)}{d\tau}\frac{d\tau}{dt} = \begin{cases} \frac{A_q\, k_q}{2}\frac{V_\infty}{L_a}\sin(k_q\tau) & \text{if } \tau < \tau_q, \\ 0 & \text{if } \tau \geqslant \tau_q. \end{cases} \tag{5.7}$$

The reduced frequency k_q and equally the adimensional time constant τ_q are suitably chosen so to excite the frequency interval of interest $k \in [0, k_{max}]$ and do not depend on the particular coordinate under consideration, namely: $k_q = \pi/\tau_q$ and $\tau_q = 2\pi/k_{max}$. The maxi-

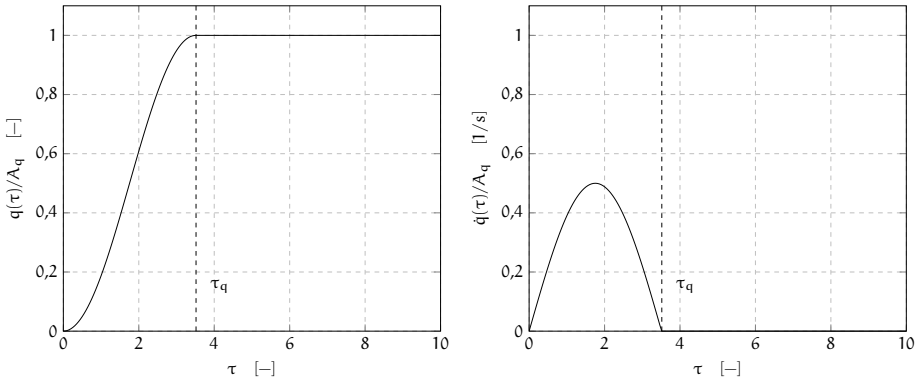

Figure 24: Blendend step input $q(\tau)$ and its derivative $\dot{q}(\tau)$ as a function of time τ.

mum amplitude A_q is chosen with the aim of exciting the aerodynamic sub-system with an input signal signal well above the numerical error threshold but without jeopardizing the hypothesis of small perturbations. Suppose that we are dealing with a detailed Finite Element (FE) structural model suitably condensed by means of an efficient modal basis as follows: $\{u_s\} = [U]\ \mathbf{q}$, where the matrix $[U] \in \mathbb{R}^{N_{FEM} \times N_q}$ stores the modal shapes. Within such a framework the maximum nodal velocity should be suitably small if compared with the flight velocity, e.g. $max(\{\dot{u}_s\})/V_\infty = \varepsilon$ with $\varepsilon = tan(1°)$. Carrying out all the computations it is possible to write the following relation for the maximum amplitude A_q, dependent on the particular coordinate under consideration:

$$A_q = \frac{4\ \varepsilon\ L_a}{max([U_i])\ k_{max}} \tag{5.8}$$

The blended step is computationally efficient because it does not require excessive time resolution to be described, and prevents Gibbs phenomena in the transient, typical of a not blended step. Typically, the number of time steps needed to correctly define the junction is $30 \div 40$, roughly. To avoid the singularity related to the asymptotic value $(1/jk)$, the *deficiency* function must be used and eq.(5.4) becomes,

$$\mathbf{H}_{am}(k)|_i = \frac{\mathbf{Q}^a_\infty(t) + jk\ \mathcal{F}\big(\mathbf{Q}^a(t) - \mathbf{Q}^a_\infty(t)\big)}{q^i_\infty(t) + jk\ \mathcal{F}\big(q^i(t) - q^i_\infty(t)\big)}. \tag{5.9}$$

which it is added to the denominator the contribution of the Fourier transform of the deficiency of the input signal $q^i(t)$.

5.3 FLUTTER CALCULATION

Moving to the Laplace domain and recalling the expression of the GAFs, eq.(4.3), the structural problem, eq.(4.2), falls in the framework of classical aeroelasticity as an algebraic homogeneous system,

$$\left[s^2\mathbf{M} + s\mathbf{C} + \mathbf{K} - q_\infty \mathbf{H}_{am}(p, M_\infty)\right] \mathbf{q}(s) = 0. \tag{5.10}$$

Such a system admits non-trivial solutions if the matrix $[A(s, V_\infty)]$ is singular and is closed in the complex unknown s for a given velocity V_∞. Starting from $V_\infty = 0$, the roots loci can be builded for the whole flight envelope. The so-called $V_\infty - \omega$ and $V_\infty - g$ diagrams, where $g = 2\sigma/\sqrt{\sigma^2 + \omega^2}$ (i.e. σ and ω are the real and imaginary parts of a complex number respectively), suitably represent the stability properties of the system. The first intersection in the $V_\infty - g$ diagram with the g axis identifies the flutter velocity, i.e. the zero damping condition.

As already said, the most difficult part of the aeroelastic analyses concerns the definition of the aerodynamic transfer functions matrix $\mathbf{H_{am}(p, M_\infty)}$. Usually, it is known for a set of discrete values of p and M_∞ and, generally, for purely harmonic boundary conditions only, i.e. with $p = jk$. Thus, common eigenvalue methods cannot be applied to solve the coupled problem, eq.(5.10), and ad hoc methods must be used.

The complex eigenvalue problem to be solved depends on the way in which the aerodynamic loads are included in the equations of motion or whether certain damping terms are included.
The two methods for flutter analysis used in this work are summarized in next sections. First, the K-E method is used just to follow the flutter analysis already provided in the literature. In this way, the validation of the procedures before described can be proved. Then, a variation of the well-known $p - k$ method [32] is exploited. The develop of a modified $p - k$ method is mandatory because it can involve some difficulties in tracking intersecting eigenvalues. The approach used here prevents such a drawback because each mode is tracked separately from the others.

5.3.1 K-E(fficient) Method

This method is a simplification of *K-method* in which are neglected all viscous sources of the structure or of the control system. The basic equation for modal flutter analysis by the *K-method* is

$$\left[-\omega^2 \mathbf{M} + j\omega \mathbf{C} + (1+jg)\mathbf{K} - \left(\frac{1}{2}\rho V^2\right) \mathbf{H_{am}}(k, \mathbf{M}_\infty) \right] \mathbf{q}(\omega) = 0, \tag{5.11}$$

where g is an artificial structural damping. Note that k, V_∞ and ω are not independent. For the K-method of solution, the aerodynamic term is converted to an equivalent aerodynamic mass,

$$\left[-\left[\mathbf{M} + \frac{\rho}{2}\left(\frac{c}{2k}\right)^2 \mathbf{H_{am}}(k, \mathbf{M}_\infty)\right] \frac{\omega^2}{1+jg} + \mathbf{C}\frac{j\omega}{\sqrt{1+jg}} + \mathbf{K} \right] \mathbf{q}(\omega) = 0, \tag{5.12}$$

or, using the relation $k = \frac{\omega c}{2V_\infty}$,

$$\left[\left[\left(\frac{2k}{c}\right)^2 \mathbf{M} + \frac{\rho}{2}\mathbf{H_{am}}(k, \mathbf{M}_\infty)\right] \left(\frac{-V_\infty^2}{1+jg}\right) + \left(\frac{2k}{c}\right) \mathbf{C} \left(\frac{jV_\infty}{\sqrt{1+jg}}\right) + \mathbf{K} \right] \mathbf{q}(\omega) = 0. \tag{5.13}$$

In the *K-E method*, the equation to be solved becomes eq.(5.13) with the term containing $\mathbf{C}$ deleted; note that complex structural damping may still be included in $\mathbf{K}$. The solutions are not valid except when $g = 0$, since the aerodynamic force terms are valid only for oscillating motion and g is not a physical damping. The values of g, V_∞, and f ([Hz]) are solved for various values of M_∞, k, and ρ. Plots of V_∞ versus g can be used to determine the flutter speed(s) (where g goes through zero to positive values).

Thus, the square of eigenvalues is

$$\lambda^2 = \frac{-V_\infty^2}{1+jg} = -V_\infty^2 \frac{1-jg}{1+g^2} = a + jb, \tag{5.14}$$

so that

$$g = -b/a, \tag{5.15}$$

$$V_\infty = \sqrt{-\frac{a^2+b^2}{a}}, \tag{5.16}$$

$$f = \frac{kV_\infty}{\pi c}. \tag{5.17}$$

Ref.[22] uses this method to predict flutter boundaries and so it is a useful test case for validating the formulation proposed to carry out the aerodynamic transfer function $\mathbf{H_{am}}$. The results obtained are reported in next chapter. For this case, the K-E method is used but the next method will be preferred for all other cases.

5.3.2 Flutter Eigensolution as a Nonlinear Problem

The aeroelastic problem, eq.(5.10), can be seen as a linear homogeneous system in $\mathbf{q}(s)$ and nonlinear in s [45, 46]. So, a normalization rule for the generalized coordinates vector $\mathbf{q}(s)$ can be added to close the problem,

$$\begin{cases} \mathbf{A}(s, V_\infty)\mathbf{q} = 0 \\ \frac{1}{2}\mathbf{q}^T\mathbf{W}\mathbf{q} = 1. \end{cases} \tag{5.18}$$

where $\mathbf{W} = diag(W_i)$ for $i = 1, \ldots, n$ (in which n =length($\mathbf{q}$)) are arbitrary weights. The obtained nonlinear system can be solved through the *Newton-Raphson* method. Linearizing around a reference solution $\mathbf{q}_0$ and s_0 we obtain,

$$\begin{bmatrix} \mathbf{A}(s_0, V_\infty) & \frac{\partial \mathbf{A}(s, V_\infty)}{\partial s}\Big|_{s_0} \mathbf{q}_0 \\ \mathbf{q}_0^T\mathbf{W} & 0 \end{bmatrix} \begin{Bmatrix} \Delta\mathbf{q} \\ \Delta s \end{Bmatrix} = \begin{Bmatrix} -\mathbf{A}(s_0, V_\infty)\mathbf{q}_0 \\ 1 - \frac{1}{2}\mathbf{q}_0^T\mathbf{W}\mathbf{q}_0 \end{Bmatrix}. \tag{5.19}$$

Such an approach allows to compute the eigenvalue and the eigenvector all at once. Starting from $V_\infty = 0$ with $\mathbf{q} = \mathbf{q}_0$ and $s = s_0$, i.e the structural solution, $V_\infty - \omega$ and $V_\infty - g$ diagrams can be plotted. The procedure must be repeated starting from each structural eigenvalue avoiding any problem with intersecting curves. In this way, the whole eigensolution is tracked with a very simple task and without the drawback of intersecting eigenvalues. Since the aerodynamic transfer functions matrix $\mathbf{H}_{am}(k, M_\infty)$ is known for a set of reduced frequencies only a proper interpolation technique must also be implemented. A linear interpolation will be used here.

Numerical Procedures

The aerodynamic transfer functions are known at particular reference conditions and for discrete values of Mach M_∞ and reduced frequencies k. As already stated, the frequencies resolution and the maximum excited frequencies depend on the blended step input chosen, while the asymptotic Mach M_∞ depends on the flight condition considered. This procedure will be employed in test case of sec.(6.3) and sec.(6.4), while in sec.(6.2) the K-E method is used just to follow the literature.
A trial transport jet is identified in order to prevent flutter in its flight envelope. In this way, an high fidelity polar is built using the preliminary design methods of [59]. Once Penaud diagrams are obtained, the condition $T = D$ is imposed for a steady rectilinear flight at a discrete number of blades pitch and various altitudes. At the end of the trim calculations, every selected pitch angle is matched with an asymptotic velocities V_∞. In particular, the blade pitch angle is referred to the plane of rotation of the rotor disk.
In the next figures, Penaud diagrams of the test case of sec.(6.3) are reported for three different altitudes (i.e. 0 m, 5000 m and 10000

m). Then, the aerodynamic transfer function are calculated at every trimmed condition (i.e. red squares of figs.(25a,25b,25c)). Finally, the $V-g$ and $V-\omega$ diagrams are obtained by a flutter calculation as a solution of a non linear problem (5.3.2). Obviously, one cannot start from null asymptotic velocity, $V_\infty = 0$, but, thanks to experience, the frequencies and eigenvectors should not change completely from the structural ones ($V_\infty = 0$), even if V_∞ is not null.

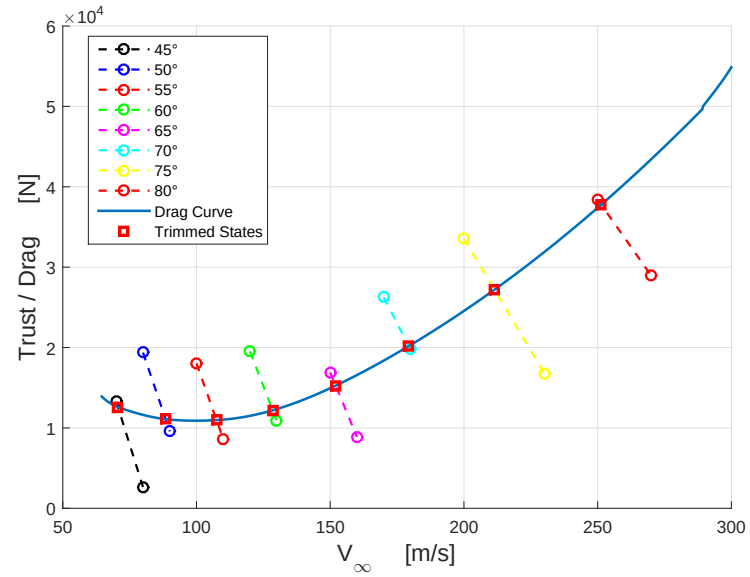

(a) Penaud Diagram at $h = 0$ m.

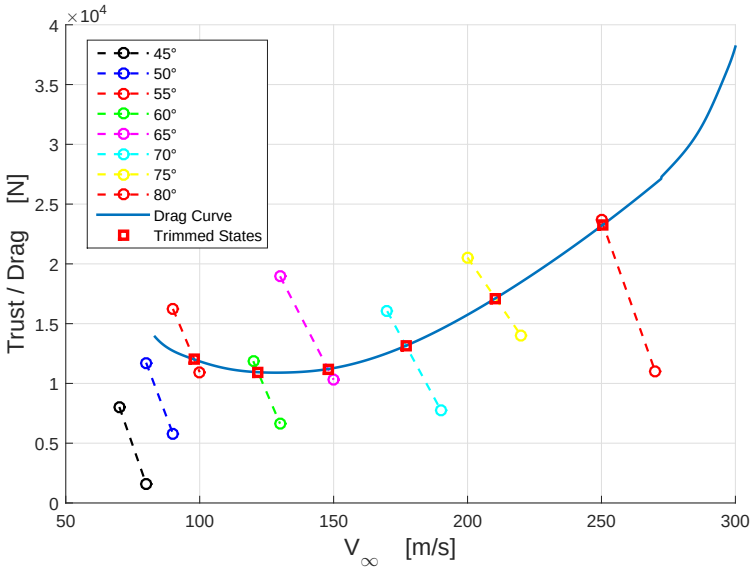

(b) Penaud Diagram at $h = 5$ km.

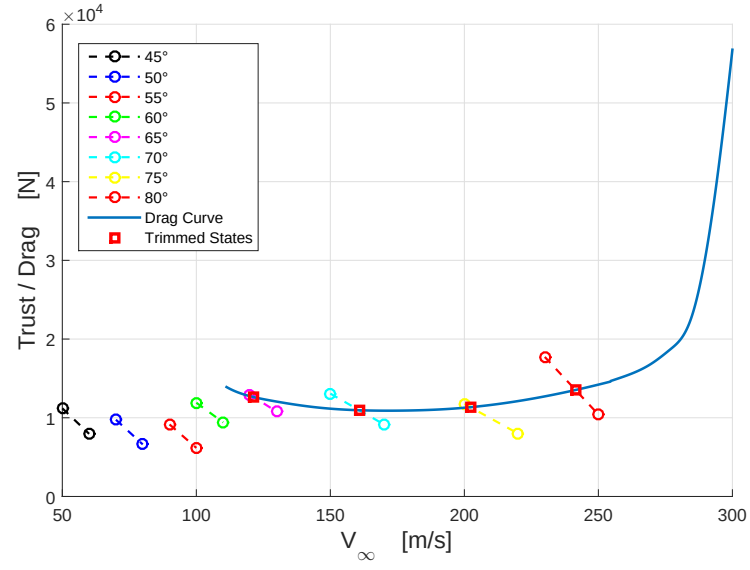

(c) Penaud Diagram at $h = 10$ km.

Figure 25

6

RESULTS

This chapter is aimed at assessing the effectiveness of the proposed techniques for the aeroelastic analysis of open rotor by comparing the results -based on our full potential formulation- with reference data available in the literature and with those obtained through the Euler flow solver AeroX [44, 58]. In particular, the formulation adopted in AeroX for simulating rotating flows is briefly presented in sec.(2.1). Moreover, the aerodynamic analyses performed with both S^T and AeroX are carried out with the same grids because the Eulerian solver can use the same periodic boundary conditions implemented in our full-potential formulation.

Four different test cases are investigated. Sec.(6.1) is dedicated at assessing the potentialities of the full-potential solver S^T with aerodynamic analyses of single and contra-rotating open rotors. Sec.(6.2) presents a complete aeroelastic analysis in accordance with ref.[22]. More precisely, after providing an overview of the structural and aerodynamic models, the aerodynamic transfer matrices $\mathbf{H_{am}}(k, M_\infty)$ are computed as explained in sec.(5.2). Successively, the K-E method is used for calculating the eigenvalues of the aeroelastic system and finally the so-called $V-g$ and V_ω diagrams show the obtained results. These two test cases represents the validation|verification benchmarks of the here proposed aeroelastic analysis techniques.
In sec.(6.3) and in sec.(6.4) the aeroelastic analyses are conducted without reference to any result available from the literature, but with the awareness gained from previous benchmarks. In particular, a first analysis is focused onto single rotating propfan while a following one discusses the stability of a contra-rotating open rotor. As explained in sec.(5.1), the flutter analyses are conducted only for a $0°$ IBPA. Moreover, the CROR, whose responses are time-periodic, is treated as a *small varying system* so studying its *frozen stability* [67].

6.1 TEST CASE 1

In this case, only aerodynamic calculation are performed to validate the solver S^T for rotating problems in fluid dynamics. The blade geometry is taken from [63]. The blade characteristic are reported in fig.(26), which shows the radial distributions of the thickness normalized by the chord t/c, the blade mean-line sweep angle Φ as well as the twist distribution β. The selection of the blade airfoils is set in accordance to

the approach of the SR-7L high-speed propeller reported in [64]. The blade features NACA65-series airfoils near the root to the radial position of $r/R = 0.4$ then transitioning to NACA16-series airfoils from $r/R = 0.55$ outward. The mean line tip sweep is $\Phi = 35°$. The rotor diameter is $D = 4.2672m$ $(14ft)$ and the hub-to-tip ratio is $d/D = 0.355$. The blade shape is so shown in fig.(27).

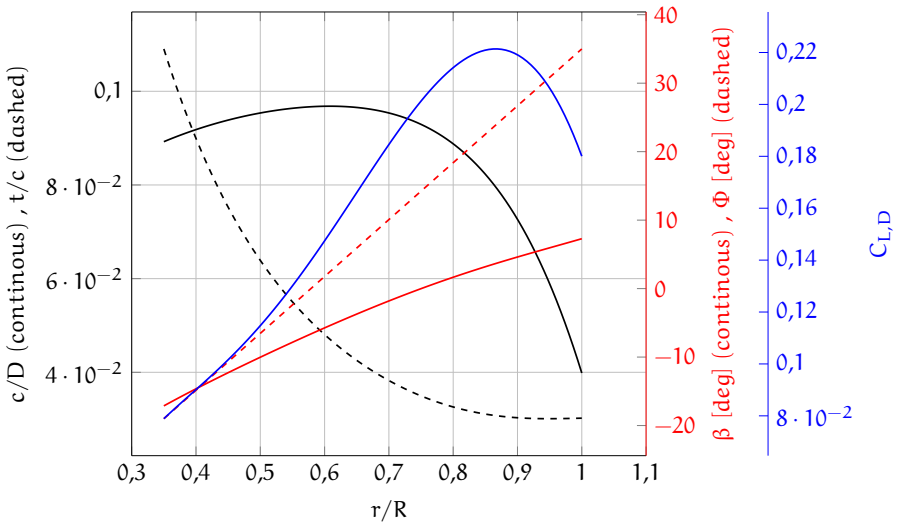

Figure 26: Generic Blade Design Characteristic.

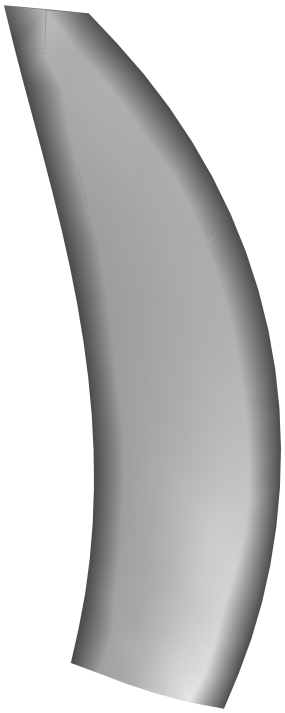

Figure 27: Blade shape available on [63]

6.1.1 Aerodynamic Analyses of a Single Rotating Propeller (SRP)

This first analyses are performed to verify the reliability and the accuracy of the full-potential results, so the simple case of an 8-blade SRP is investigated. Ref.[63] performs the simulations using the DLR-TAU-code, [27], with all its simulations carried out using the Spalart-Allmaras turbulence model. Ref.[63] fully exploits the Chimera functionality [42], so to enable a variation of the blade pitch settings without any re-meshing. The full rotor is discretized with a structured Euler HEXA mesh. Such an approach deemed appropriate, as the blade aerodynamics are properly modelled in such a computation for the axis-symmetric geometry and no unsteady flow phenomena (save for separation regions) occur for an SRP in a rotating frame of reference, in which an inviscid hub rotates at the same rotational speed as the propeller itself.

The simulations are carried out at the design cruise case with a propeller rotational speed of $\Omega = 895$ RPM. The pitch angle at 75% of the blade span, $\beta_{75\%}$, varies from 56° to 63° without changing the flight condition reported in tab.(2). This flight condition leads to a helical tip Mach number of $M_{tip} = 1.0068$, so that weak shocks are expected on the blade surface. The geometric angle of attack remains always under 5° at the 75% of the blade span, so separated flow is no expected. Actually, a small flow separation is generated by the weak shock onto the outer surface.
For such an application, S^T gives very acceptable results even if the entropy correction is turned off. The aerodynamic mesh for the S^T solver is generated as explained in sections 2.5 and 2.6 with the commercial mesh generator, *GAMBIT®*. In particular, the discretization adopted consist of nearly 160k nodes (i.e. 850K tetrahedrons).

M_∞	0.75
h	10668 m
ρ_∞	0.4135 Kg/m^3
P_∞	26500 Pa

Table 2: Flight Conditions

Fig.(28) reports comparisons of the thrust coefficient C_T, the torque coefficient C_l, the power coefficient C_P and propeller efficiency η, defined as

$$C_T = \frac{T}{\rho n^2 D^4}, \qquad C_l = \frac{\mathcal{C}}{\rho n^2 D^5},$$
$$C_P = 2\pi\, C_l, \qquad \eta = \frac{C_T}{C_l}\frac{J}{2\pi}. \tag{6.1}$$

where:

$$n = \Omega/2\pi, \qquad [1/s] \rightarrow \text{Propeller Rotational Speed}$$
$$J = V_\infty/(nD), \qquad [-] \rightarrow \text{Advance Ratio}$$
$$\mathcal{C} = \rho n^2 D^5 C_l, \qquad [\text{N m}] \rightarrow \text{Torque}$$

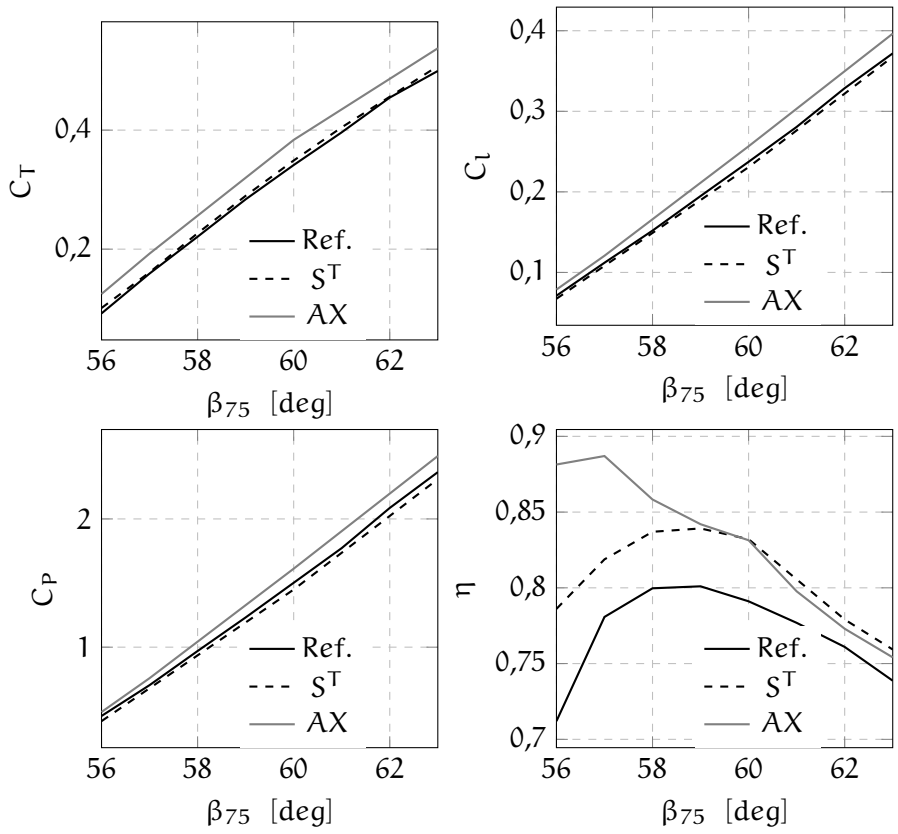

Figure 28: Comparison between the results obtained by the reference [63], S^T and AX.

As it can be seen from the previous figures, the uRANS results show a good accordance to those obtained with S^T while the Eulerian solver AeroX provides worse somewhat correspondences, in particular for the efficiency η. As it can be noted, the potential solution is in the middle between those obtained with uRANS and Euler solvers, so it is proved another time that full-potential solvers can be a valuable tool for the preliminary analyses in the frame of Computational Fluid Dynamics. The differences can be imputed to the effects of the boundary layer that are not modelled in an Euler|potential solution. The approximations introduced by S^T leads our calculation to more realistic results, i.e. closer to uRANS simulations, but, obviously, this is not a desirable effect. Other differences can be attributed to different numerical schemes adopted.

Fig.(29) and fig.(30) shows the Mach and Cp distributions respectively onto the upper surface of the blade for the steady state obtained

with $\beta_{75\%} = 60°$. As said, the local Mach number reaches transonic values and a weak shock extending from the tip to the root of the blade can be noted. These solutions are obtained without the activation of the entropy correction but the potential solution is very similar to the Eulerian one. Probably, a better representation of the Cp|Mach distributions can be obtained with a finer grid onto the blade surface. This fact will also help to better estimate the position and the intensity of the shock.

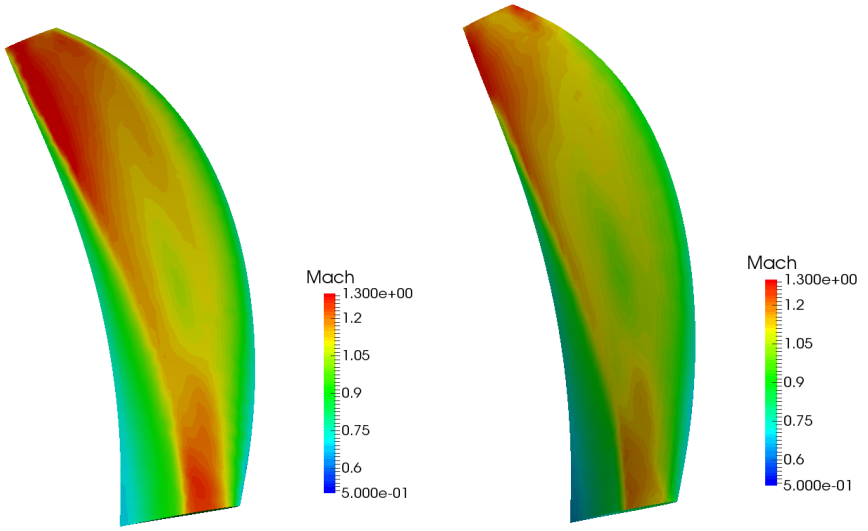

(a) Mach Distribution obtained by S^T. **(b)** Mach Distribution obtained by AX.

Figure 29: Comparison between Mach distributions.

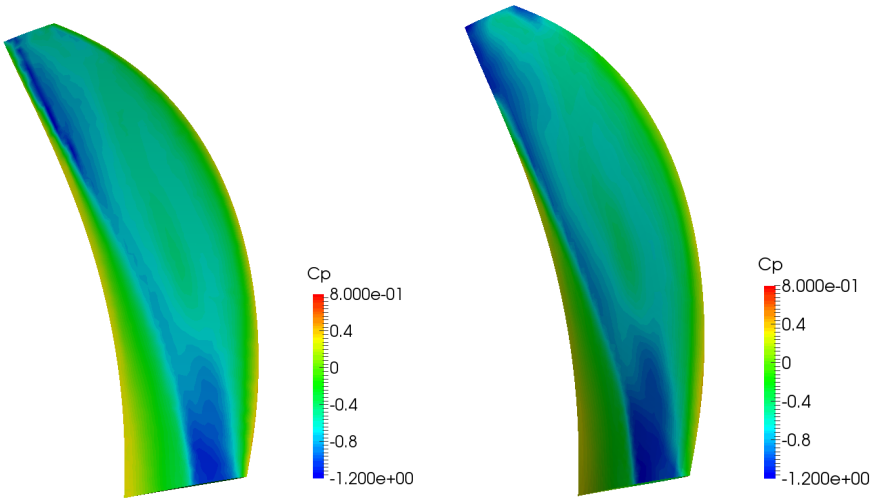

(a) Cp Distribution obtained by S^T. **(b)** Cp Distribution obtained by AX.

Figure 30: Comparison between Cp distributions.

6.1.2 Aerodynamic Analyses of a Contra-Rotating Open Rotor (CROR)

The mesh for the isolated CROR configuration of [63] consists of a total of 20 Chimera blocks representing the complete engine (comprehending the core engine air intake and exhaust). The complete 20-block Chimera mesh which was used for the uRANS computations consists of 40.8M nodes with a total of 25 hexahedral layers placed on all surfaces of the nacelle and of the blades.

The assumption of equally partitioned thrust between both rotors is used for the case of axis-symmetric flight condition. Furthermore, the interaction between the blades of the forward and aft rotors have a significant effect on the individual blade performance, leading to strongly modified characteristics respect with the SRP condition. The operating conditions are the same as the SRP case, as reported in tab.(2). The "ghost technique", explained in sec.(4.5), is here verified to work reasonably.
Tab.(3) shows a good accordance for the pitch angles at 75% of blade span. The differences in the set angles are lower than 1°. This error can be imputed to the different approaches used to describe such a periodic system. Moreover, the details modelled in our mesh are significantly less than those of the grid of ref.[63], which models the whole engine.

	Ref.[63]	S^T
Front Rotor $\beta_{75\%}$	61 °	60.5 °
After Rotor $\beta_{75\%}$	57.9 °	57 °

Table 3: Blade Pitch Angle at 75% of span-wise direction for equally partitioned thrust between both rotors at an angular velocity of $\Omega = 895$ RPM and at an altitude of 35.000 ft

The flow field exhibits unsteady phenomena which are periodic in nature, linked to the rotational speed and the number of blades of the rotor. In particular, the period of an oscillation for $\Omega = 895$ RPM and $N_b = 8$ is equal to

$$T = \frac{1}{2N_b}\,\frac{60}{\Omega} \simeq 4.19 \cdot 10^{-3}\ \text{s}. \tag{6.2}$$

Fig.(31) shows the trend of the thrust coefficient of the separated rotors. It can be inferred that the amplitude of the second stage C_T is greater than the one of the first stage because of the interactions of the second stage with the wake surfaces released by the first propeller. The amplitudes of the oscillations of both stage are slightly smaller with respect to those reported in ref.[63]. In particular, the front rotor seems to be less affected from the oscillating loads of the second propeller.

Tab.(4) reports the comparison of the mean values of the C_T, C_P and η at regime. It can be inferred that the thrust coefficient is well

approximated by S^T (i.e. the relative errors are about 4% and 3% for the first and the second stage respectively).

Of course, the values of C_P and η differ. In fact, the potential solver underestimates the torque on the rotating axis because it does not comprehend the effects of the viscous drag forces of the blade. This fact involves lower power coefficients, and so greater efficiencies with respect to those calculated with a uRANS simulation.

	Front Rotor			Rear Rotor		
	C_T	C_p	η	C_T	C_p	η
Ref.	0.3372	1.5956	73.85%	0.3379	1.4838	79.58%
S^T	0.3507	1.4544	83.33%	0.3486	1.2649	95.26%

Table 4: Comparison of the most important parameter of CROR.

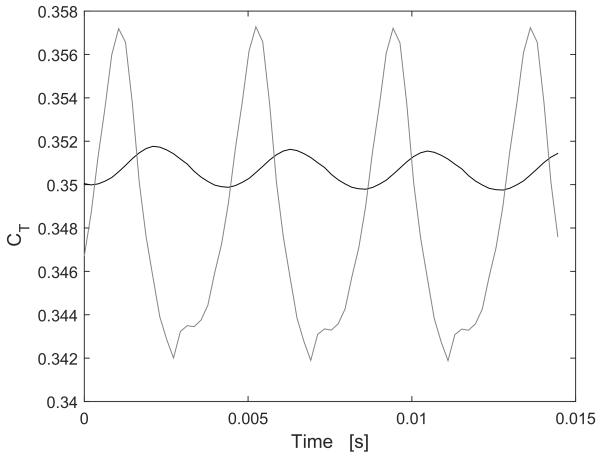

Figure 31: Trend of the C_T of the front (black) and after (gray) rotors.

6.2 TEST CASE 2

In this section, the flutter analysis of the $SR-5$ propfan, a 10-blade wind tunnel model designed by Hamilton Standard in early '80s, is carried out. This model was designed during the so-called "Advanced Turboprop Project" as described in cap.(1). This blade has a tip sweep of 60°, the maximum value allowed for a metal blade without excessive stresses, a medium chord of 7.67 cm and a span of about 30 cm. During performance testing in the Lewis transonic wind tunnel, the $SR-5$ propeller encountered classical flutter above $M_\infty = 0.7$ and thus could not achieve its design point.

6.2.1 FE Analyses

The structural grid is taken from [21] where the coordinates of the grid points, the connection matrices and the material properties are translated to a *NASTRAN*® bulk input file. The blade is discretized only with shell elements so, it will not be carried out a comparison with solid elements. Only NASTRAN will be used and the so obtained results are compared with those of the experimental and numerical data available in the literature. Fig.(32) shows the structural model available from [21], which consists of both CQUAD8 and CTRIA6 elements. The blade is fully constrained at its base.

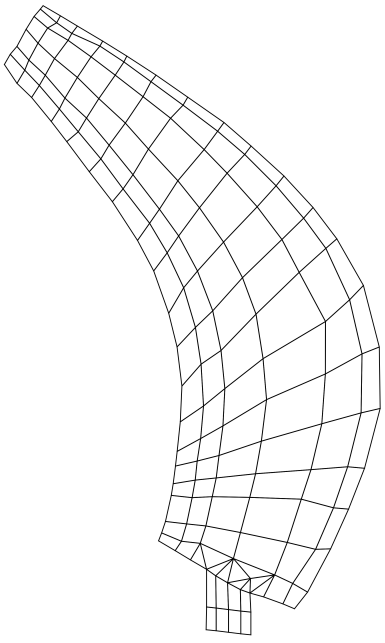

Figure 32: SR-5 *NASTRAN*® structural model

Modal Analysis

First, the normal modes of the simply clamped blade are calculated. The material properties are the same as those reported in tab.(9). In this case, it has been decided to use the same model available from ref.[21] but with the CQUAD4 and CTRIA3 elements of NASTRAN libraries. In this way, the models with linear and parabolic elements are compared. The eigenvalues obtained with linear shell elements are very close to those obtained with parabolic ones. For this analysis, the measured experimental frequencies are available.

	Ref.[23]			Ref.[74]
		NASTRAN		
mode	Exper.	CQUAD8	CQUAD4	HEXA
1st	112.0	114.0	109.4	113.8
2nd	278.0	285.0	281.0	284.0
3rd	483.0	562.0	517.0	558.1
4th	630.0	650.0	647.7	654.3
5th		807.0	720.2	818.4
6th		966.0	970.9	1003.2

Table 5: Non Rotating Normal Frequencies [Hz] of the SR-5 blade

Since the small thickness distribution and the well modelled joint, there are acceptably small differences among the various models.

Modal Analysis of Rotating Blades

Tab.(6) reports the first 6 normal frequencies for the rotating blade at an angular velocity of 6800 RPM. The displacement constraint is the same as above, i.e. a simply clamped plate at its base.

	Ref.[23]		Ref.[74]
	NASTRAN		
mode	CQUAD8	CQUAD4	HEXA
1st	187.9	160.9	173.7
2nd	292.8	287.0	285.4
3rd	612.6	595.9	598.4
4th	666.9	670.7	647.2
5th	822.3	863.2	816.8
6th	1008.5	1013.4	970.0

Table 6: Rotating Normal Frequencies [Hz] of the SR-5 blade

The errors committed using the CQUAD4 elements are greater when calculating the rotating normal modes with respect to those of the non rotating frequencies, probably because the less precise representation of the trim with centrifugal forces. Fig.(33) shows the first 4 normal

shapes. It can be inferred that the first two modes are mainly in bending while the third is mainly torsional.

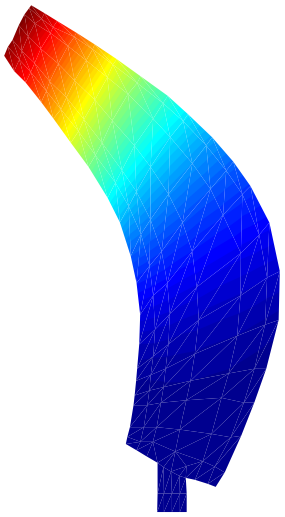

(a) *Rotating 1st Mode*, 160.9 Hz.

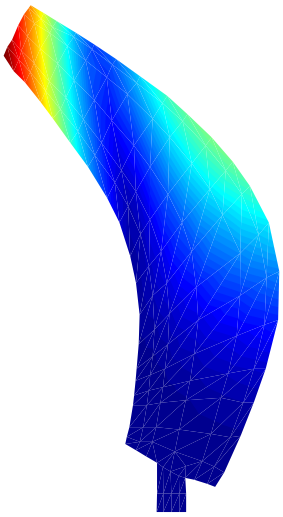

(b) *Rotating 2nd Mode*, 287.0 Hz.

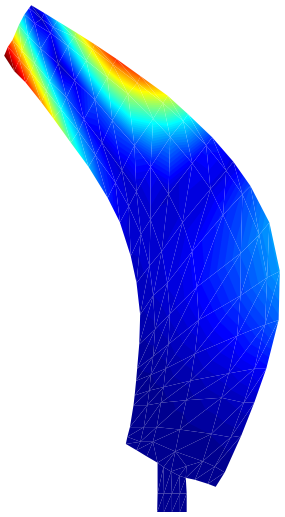

(c) *Rotating 3rd Mode*, 595.9 Hz.

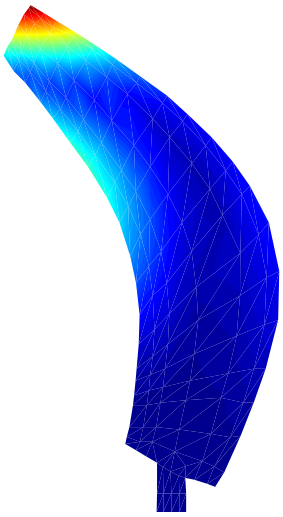

(d) *Rotating 4th Mode*, 670.7 Hz.

Figure 33: Rotating Mode Shapes of the SR-5 blade.

6.2.2 Aerodynamic Analysis

Tab.(7) reports the 4 wind tunnel test conditions for the SR-5 propfan taken from [23]. Since the too high asymptotic Mach number M_∞ and

Case No.	RPM	No. of Blades	Blade Setting Angle $\beta_{75\%}$	V_∞ [m/s]	Density [Kg/m^3]	Mach No. M_∞
1	6900	5	69.0°	277.88	0.9488	0.85
2	6000	10	69.0°	263.86	1.0067	0.80
3	6800	10	69.0°	237.13	1.0433	0.70
4	6200	10	69.0°	280.90	0.9151	0.85

Table 7: SR-5 Operating Conditions

mean angle of attack, the cases 1 and 4 cannot be investigated. In all the cases, the local Mach number at the blade tip always reaches transonic values, e.g. fig.(34) which refers to the operating condition of case 3. In the cases 1 and 4, S^T has serious problem to converge at a steady solution because the angle of attack is too high (about 15°) in relation to the asymptotic Mach number $M_\infty = 0.85$. Thus, only the results from cases 2 and 3 are compared with those available from the literature and from AeroX.

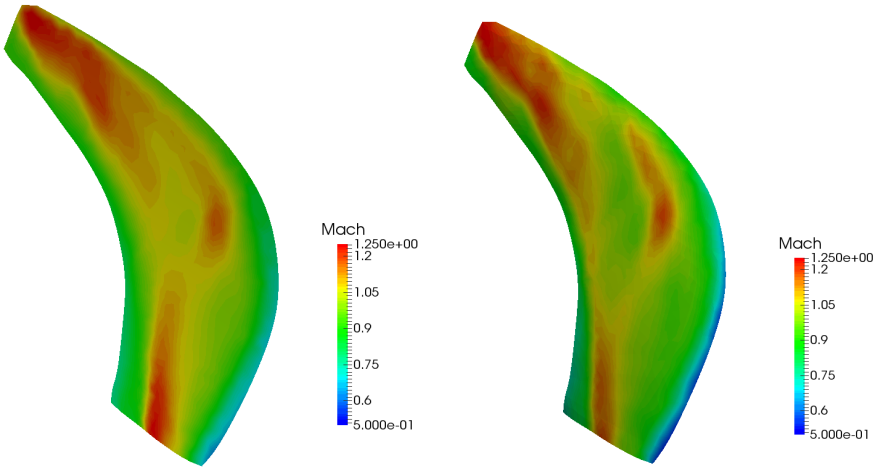

(a) Mach distribution obtained by S^T **(b)** Mach distribution obtained by AX

Figure 34: Comparison between Mach distributions.

The cases 2 and 3 are more "friendly" to S^T, so that appropriate comparisons can be carried out. The maximum local Mach number is about 1.2 at the tip of the blade and the angle of attack at 75% of the span is 8° and 14°, respectively for case 2 and case 3.

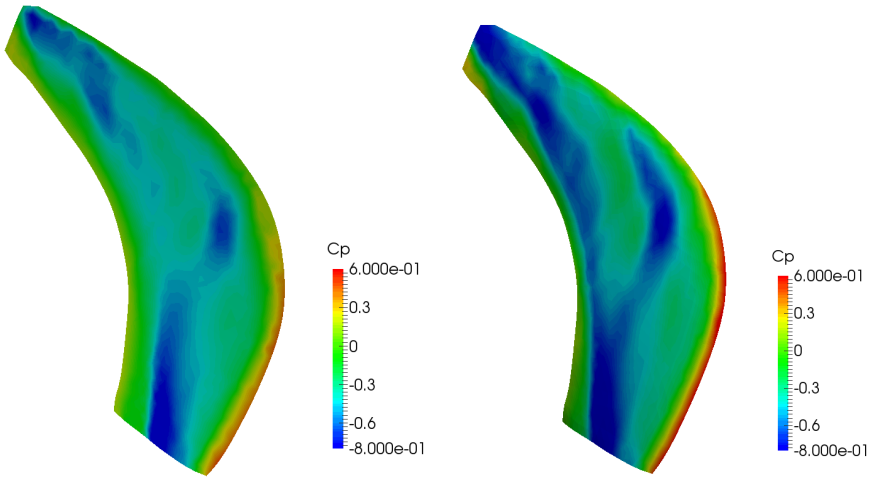

(a) Cp distribution obtained by S^T **(b)** Cp distribution obtained by AX

Figure 35: Comparison between Cp distributions.

6.2.3 Flutter Analysis

Tab.(8) reports the reference chords and the mean sweep of the blade. The latter is used to plot the $V-g$ and $V-\omega$ diagrams because $V_S = V_\infty \cdot \cos(\Lambda)$. The amplitudes of the blended step input are calculated using eq.(5.8), so remaining within a linear aerodynamic regime. Since the maximum value of the excited frequency is $k = 1.5$, the value $k_{max} = 3$ is chosen to evaluate the length of the transient of the blended step input. As already said, k_{max} must be almost the double of the value of the maximum excited frequency k, in order to have a good frequency resolution for the aerodynamic transfer matrices $\mathbf{H_{am}}(k, M_\infty)$.

Case No.	Chord c [m]	Sweep Angle Λ [deg]
1	0.07367	50.140
2	0.07366	50.109
3	0.07367	50.138
4	0.07366	50.117

Table 8: Unsteady Aerodynamics Data

The KE method, presented in sec.(5.3.1), is used for these flutter analyses. The damping g and the modified eigenvalues ω of the system are calculated with eq.(5.13) setting the discrete values of reduced frequencies as 0.1, 0.2, 0.3, 0.6, 0.9, 1.2, 1.5. The aeroelastic system is reduced to the first 6 modes coming from the structural analysis of the blade subjected to centrifugal loads only. Fig.(36) and fig.(37) show the aerodynamic response to the blended step input and the aerodynamic transfer matrix of the first 2 modes. The related figures compare the

results obtained with S^T (black) and AeroX (gray) for case 2. Although the asymptotic value is not equal, the frequency content of the aerodynamic transfer matrices obtained with the two solvers is very similar. On one side, the differences are caused by the high transonic regime over the outward surface of the blade, in fact the local Mach number reaches nearly supersonic values (i.e. 1.25 in case 2). The range of applicability of the potential solver is at its limits because the entropy released by the shock is badly approximated even if the entropy correction implemented is turned on. A more precise solution can be obtained by using a finer grid, so to predict in a better way the position and the intensity of the shock onto the outward surface for both case 2 and case 3.
On the other side, the values of the amplitudes of the blended step input are chosen with the aim of exciting the aerodynamic sub-system with an input signal well above the numerical error threshold but without jeopardizing the hypothesis of small perturbations. In this way, the aerodynamic forces and shock motion will be linear for small deformation of the blade.

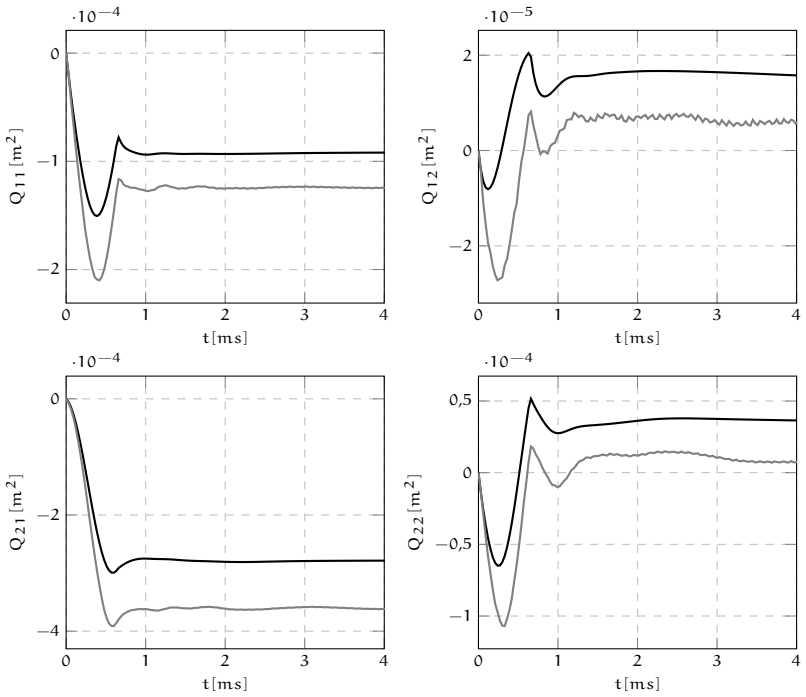

Figure 36: Aerodynamic Modal Responses of Case 2. Only the first two rows and columns are reported. (●) for S^T and (●) for AeroX.

The quality of the images of [23] is poor so only a qualitative accordance can be proven. It can be inferred that the S^T solver provides results very similar to those obtained with the modified strip theory proposed in [51]. In this way, the results obtained within the framework of Computational Aeroelasticity are justified. Moreover, it is proved that the modified strip theory proposed in [51] is an appropriate method

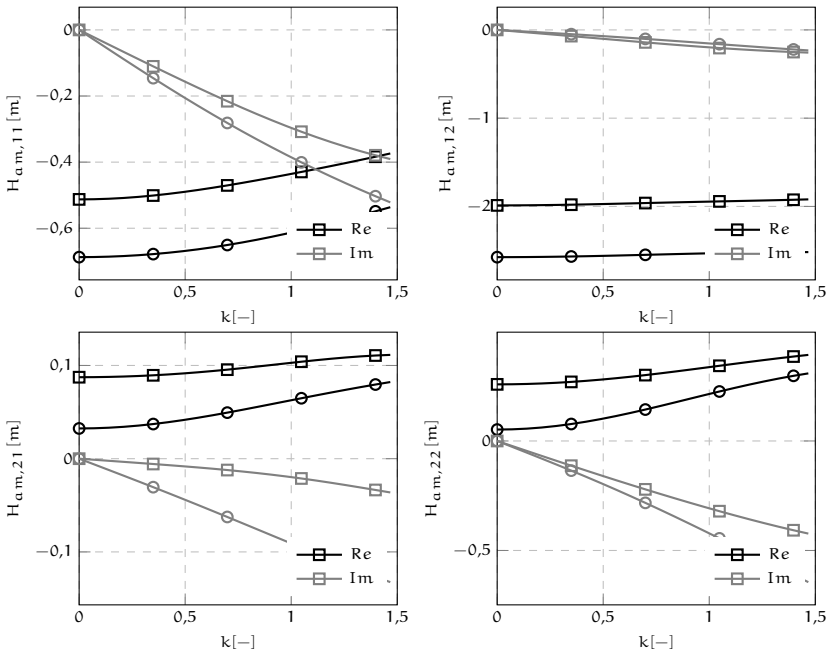

Figure 37: Aerodynamic Modal Responses of Case 2. Only the first two rows and columns are reported. (●) for S^T and (●) for *AeroX*.

for computing the aerodynamic solution around a rotating blade.
For both cases there is a flutter of the second mode (i.e. the second bending one) at the asymptotic velocity of 190 m/s and 179 m/s for case 2 and case 3 respectively and for critical reduced frequencies between 0.2 and 0.3. From $V-g$ and V_ω diagrams, it can be inferred that the flutter instability is a coupled bending-torsional one because the frequencies ω of the second and third normal modes tend to get closer. This test case proves acceptable reliability of:

- The aerodynamic solvers S^T and *AeroX*;
- The numerical procedures for carrying out the aerodynamic transfer function $\mathbf{H_{am}}(k, M_\infty)$.

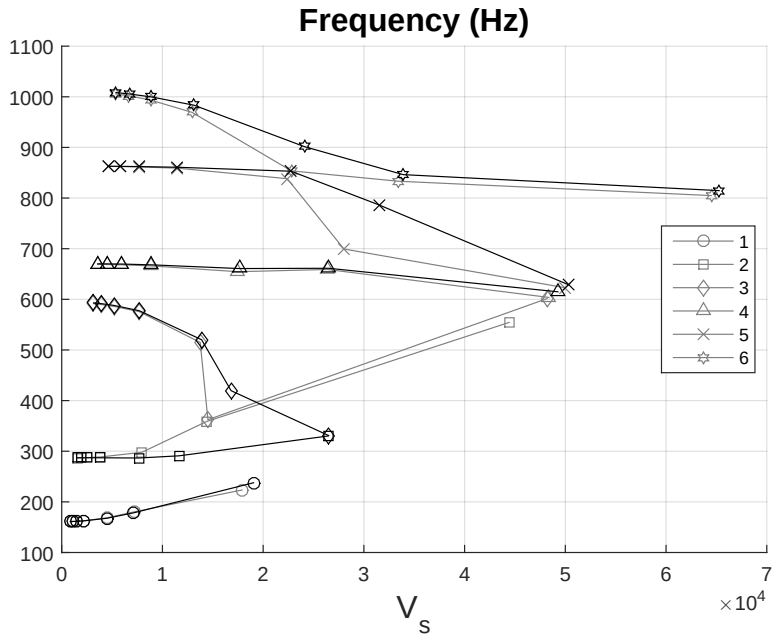

Figure 38: V-f of Case 2. (●) for S^T and (●) for AeroX.

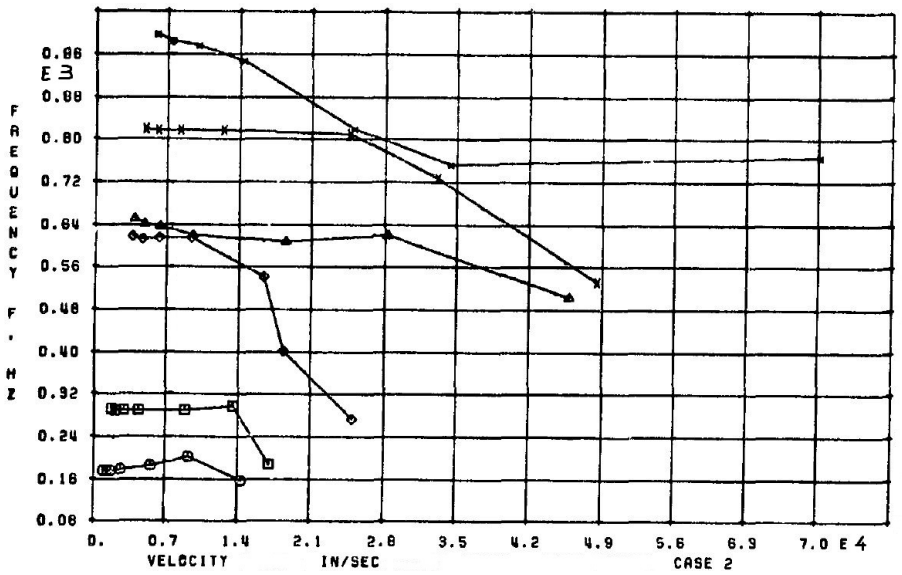

Figure 39: Reference V-f of Case 2.

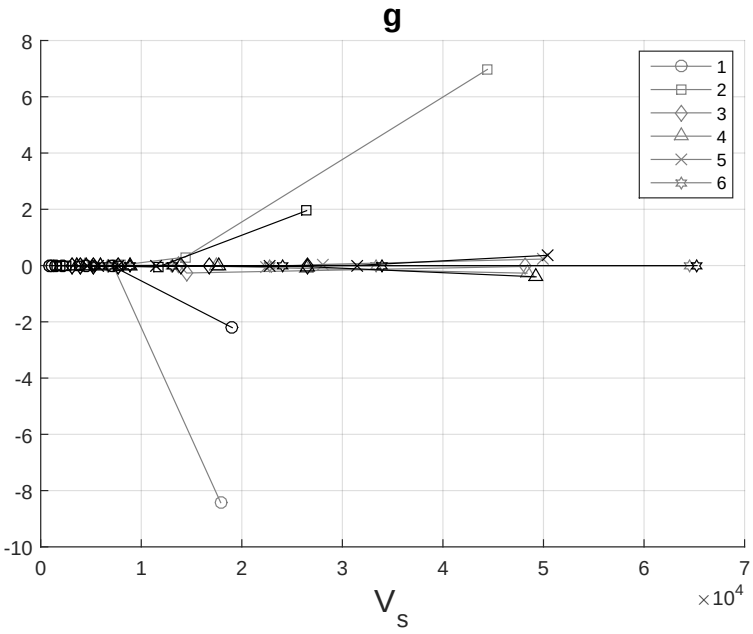

Figure 40: V-g of Case 2. (●) for S^T and (●) for AeroX.

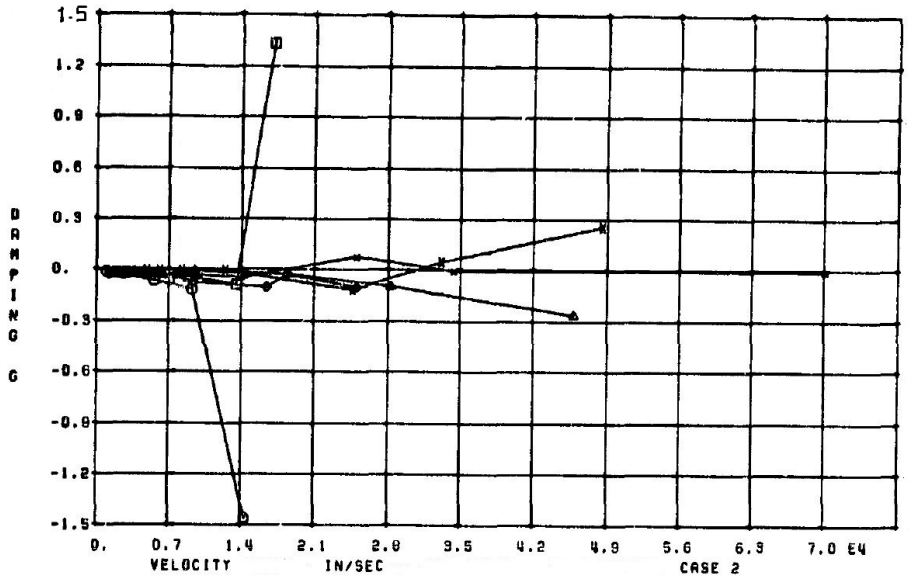

Figure 41: Reference V-g of Case 2.

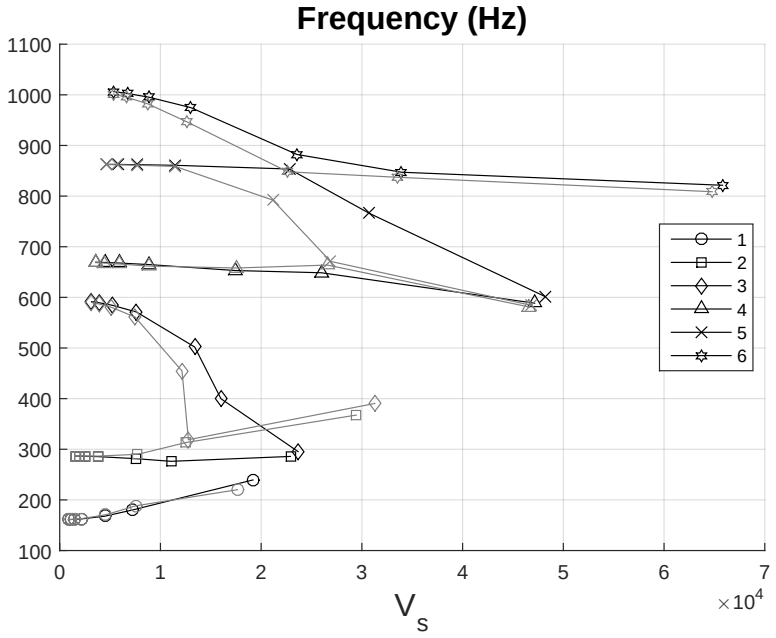

Figure 42: V-f of Case 2. (●) for S^T and (●) for AeroX.

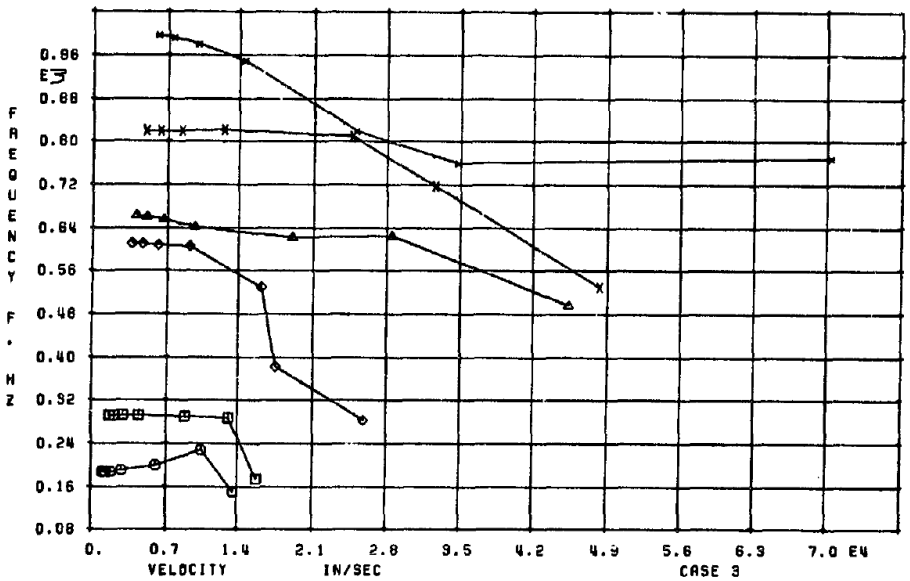

Figure 43: Reference V-f of Case 2.

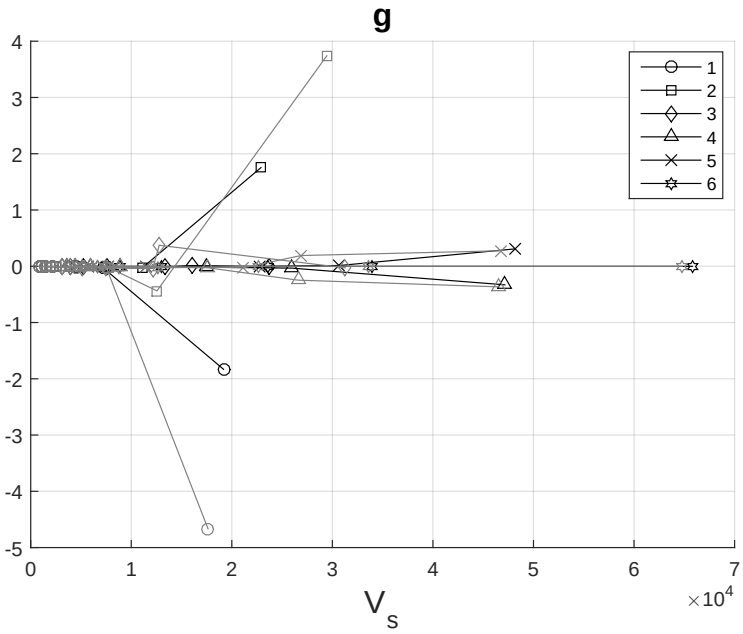

Figure 44: V-g of Case 2. (●) for S^T and (●) for AeroX.

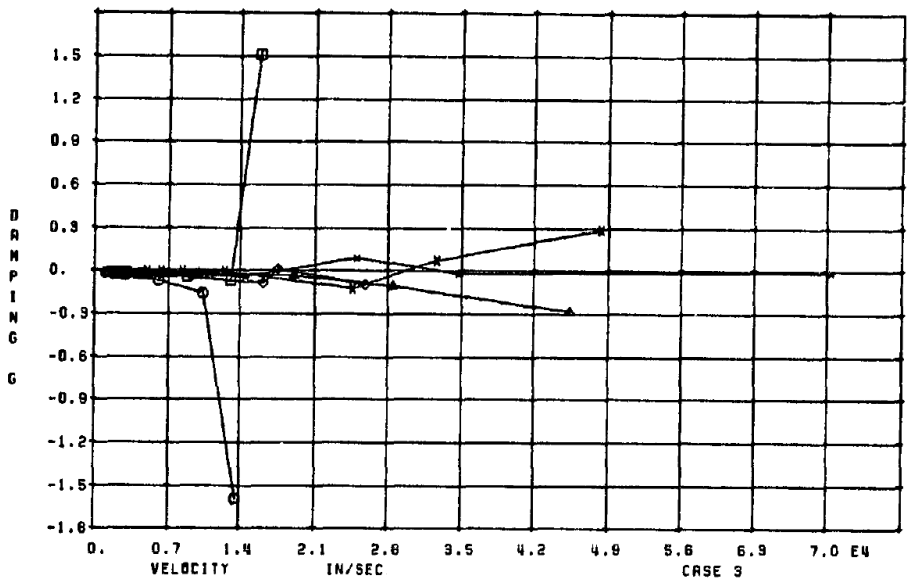

Figure 45: Reference V-g of Case 2.

6.3 TEST CASE 3

The blade shape is taken from US Patent [60], which provides the coordinates of various sections of the blade as sec.(6.1). A CAD model of the blade is then created with *SolidWorks*®, as shown in fig.(46):

Figure 46: CAD of the blade [60]

The blade height is about 1.15 meters with a mid chord of 40 centimetres. The blade twist and sweep are aerodynamically optimized so improving the range of the blade operational flight condition. Ref.[60] guarantees no flutter instabilities for a common transport jet flight envelope. Once more, the procedures described in sec.(5.3.2) is used to study the flutter boundaries in this case.
As in sec.(6.2), the structural analyses are conducted first. Various finite elements models are created to assess the best solution for representing its structural dynamics. In particular, shell and solid models are employed. Then, the static aeroelastic problem computing the reference equilibrium, or "trim", configuration of this blade is presented. Eventually, after computing the reference equilibrium for the (numerical) linearization of the generalized aerodynamic forces, the aerodynamic transfer matrices are built and the root-tracking non-linear method for computing the $V-g$ and $V-\omega$ diagrams is used. Such procedures is repeated for different altitudes and asymptotic velocities, as explained in sec.(5.3.2).

6.3.1 FE Analyses

A comparison between two FEM commercial solvers (i.e. *Ansys*® and *MSC NASTRAN*®) is carried out to better understand their capabilities

to represent a rotating structural element. For both solver a detailed solid element model with about 30K tetrahedrons has been developed.

Since the blade has an irregular geometry, the tetrahedral element is preferred to the hexahedral one. It is well known that 4-node tetrahedron can only give a constant stress state so it is better to abound with this TETRA-element to overcome this issue. Thus, both linear (4 nodes) and parabolic (10 nodes) tetrahedrons are used to model the blade. It is stressed that only a good approximation of the normal frequencies and mode shapes is needed to built a reduced aeroelastic model. It is important to underline that there are small variations of the eigenvalues and mode shapes with respect to the blade pitch angle β.

Eventually, a convergence study of normal frequencies is carried out with a shell elements model so validating the results obtained with solid elements. For the regression to shell element representation, the body is approximated with its mid surface and with a function representing its thickness distribution.

Modal Analysis

As said previously, two different mesh are created but the element type is always a tetrahedron (linear or parabolic). The material properties are reported in tab.(9). As suggested by ref.[60], the blade is modelled as a single piece of Titanium, whose properties are reported in tab.(9).

Material	Titanium alloy
Young Modulus [GPa]	111
ν	0.34
ρ [Kg/m^3]	4425.2

Table 9: Material Properties

Ref.[19] demonstrates that the hub is substantially stiffer than the blades, so it is acceptable to model only a clamped blade. Thus, all its root degrees of freedom are fully constrained.

A first analysis with the non-rotating blade is performed with a classical SOL 103 with *NASTRAN*® and with *Normal Modes Calculation* with *Ansys*®, the related first normal frequencies are reported in tab.(10).

It is difficult to distinguish bending and torsional modes, since they are always coupled because of blade twist and sweep. We can observe that the first two modes are mainly in bending while the third mode is mainly torsional. From tab.(10), it can be inferred that the model with linear tetrahedron is not yet converged.

	ANSYS	NASTRAN	
mode	TET10	TET10	TET4
1st	43.54	43.53	58.20
2nd	110.83	110.78	163.95
3rd	178.12	178.07	265.71
4th	216.65	216.45	341.53
5th	340.56	340.45	485.20
6th	353.03	352.48	543.72

Table 10: Non Rotating Normal Frequencies [Hz].

Modal Analysis of the Rotating Blade

A second analysis is performed to evaluate the deformed shape and the eigenvalues under the centrifugal load. Tab.(11) reports the first 6 normal frequencies for an angular velocity of 1900 RPM.

	ANSYS	NASTRAN	
mode	TET10	TET10	TET4
1st	56.90	57.25	63.46
2nd	127.70	127.92	166.64
3rd	195.21	195.54	268.29
4th	235.41	235.50	344.08
5th	356.93	357.31	485.72
6th	371.66	371.48	544.99

Table 11: Rotating Normal Frequencies [Hz] with $\Omega = 1900\text{RPM}$.

Fig.(47) shows the first 4 mode shapes under a centrifugal load related to an angular velocity of 1900 RPM. It is confirmed that that bending and torsional modes are coupled because of the complex blade geometry (i.e. mostly caused by the blade sweep).

Tab.(10) and tab.(11) show a good accordance between the normal frequencies obtained from *Ansys*® and *NASTRAN*® when a TET10 element is used. The results obtained with a linear tetrahedron TET4 are always worse than the former ones, not only in the prediction of eigenvalues but also in the displacement field resulting from the static analysis with the centrifugal load. Fig.(48) shows the error between the deformed shape of TET4 and TET10 models, defined as

$$err = \frac{||\mathbf{u}_s^{TET10}(\mathbf{x}) - \mathbf{u}_s^{TET4}(\mathbf{x})||}{max\left(||\mathbf{u}_s^{TET10}(\mathbf{x})||\right)}, \tag{6.3}$$

where $\mathbf{u}_s^{TET10}(\mathbf{x})$ and $\mathbf{u}_s^{TET4}(\mathbf{x})$ are the displacement fields obtained from the static analysis of the two different solid model. It is also stressed that the grid differs only in the typology of TET element and not in the number of them.

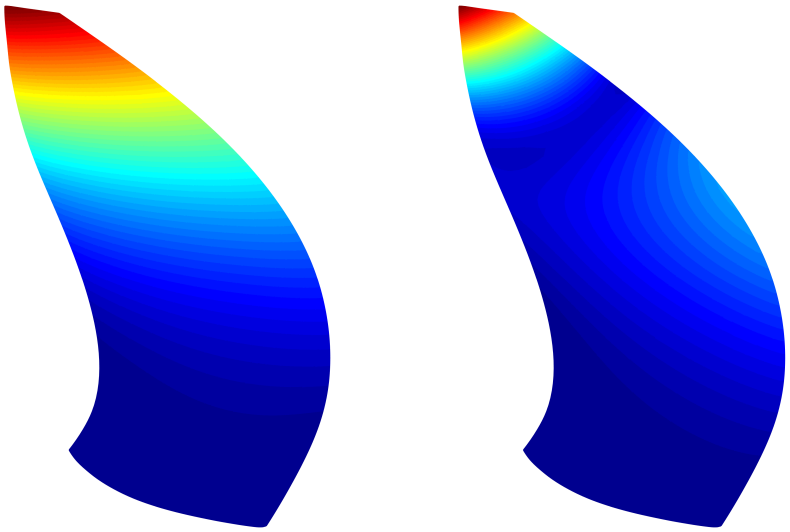

(a) *1st Mode.*

(b) *2nd Mode.*

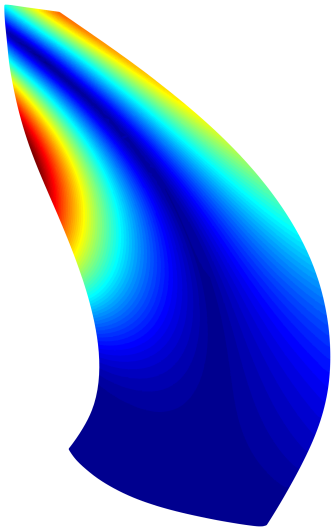

(c) *3rd Mode.*

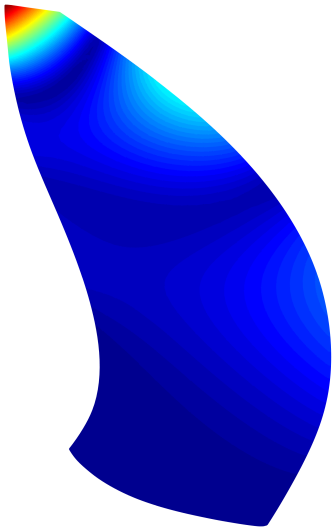

(d) *4th Mode.*

Figure 47

Dependency of Eigenvalues from Pitch Angle

Here the comparison of frequencies between different pitch angles of the blade is carried out as reported in fig.(12). The eigenvalues change

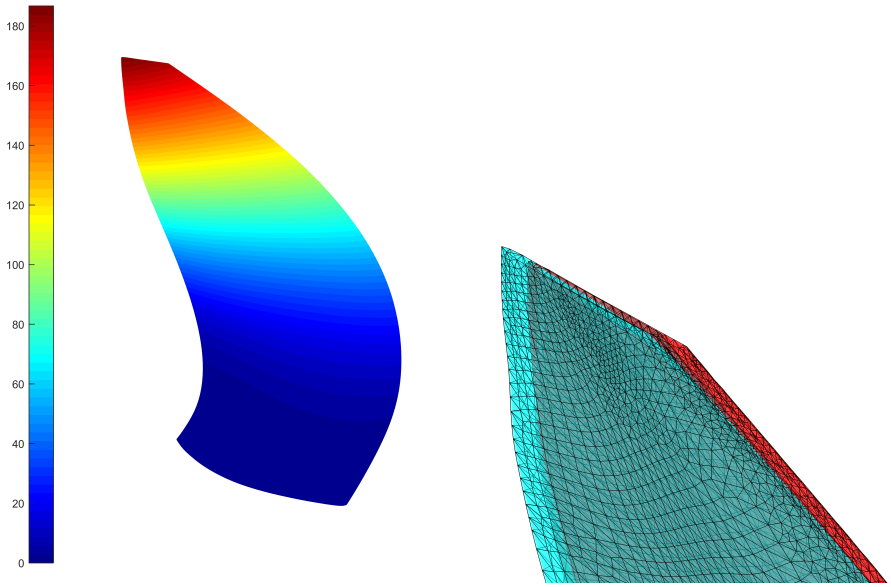

(a) *Error between TET4 and TET10 in the deformed shape under the centrifugal load.*

(b) *A zoom on the blade tip shows the different displacement fields obtained by TET4 (cyan) and TET10 (red).*

Figure 48

with pitch angles because of the different distribution of the centrifugal load onto the blade. The first two frequencies are more affected to the variable pitch. The modal shapes, instead, remain nearly unaltered.

$\beta_{0\%}[°]$	1st	2nd	3rd	4th	5th	6th
45	50.12	117.25	182.73	222.06	345.27	356.48
50	49.95	117.28	182.83	222.22	345.43	356.78
55	49.78	117.26	182.88	222.32	345.53	356.98
60	49.60	117.21	182.87	222.35	345.56	357.07
65	49.42	117.13	182.80	222.31	345.53	357.05
70	49.25	117.01	182.67	222.20	345.43	356.92
75	49.09	116.85	182.49	222.02	345.26	356.68
80	48.95	116.67	182.26	221.78	345.04	356.33

Table 12: Dependency of Eigenvalues with variable pitch angle at $\Omega = 895$ RPM

Convergence Study with SHELL model

Since plate model is seen as the most reliable and simple solution to represent the structural system in aeroelastic analyses (as explained in [22]), various model with an increasing number of shell elements have been developed to validate the results obtained with the solid models of previous the section. The blade geometry is simplified with its mid-plane surface plus a function describing its thickness distribu-

tion. Only the *NASTRAN*® solver is used to perform such a study and its parabolic CQUAD8 element is selected. The related parametric study has the goal to validate the eigenfrequencies and modal shapes obtained VS the more complex solid models. Tab.(13) and tab.(14) report the eigenvalues of the coarsest and finest structural grid, for both rotational and non-rotational conditions. Fig.(49) shows the structural grids above introduced.

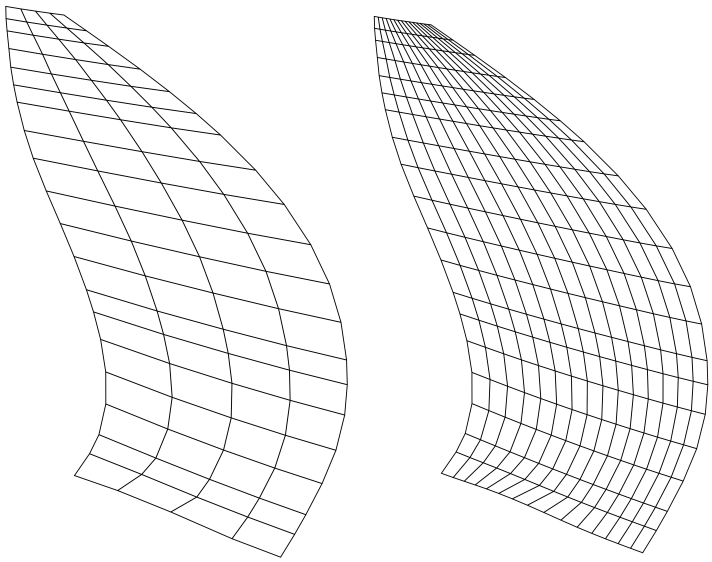

(a) 4x19 *CQUAD8 elements*. **(b)** 15x19 *CQUAD8 elements*.

Figure 49

	CQUAD4		CQUAD8	
mode	coarse	fine	coarse	fine
1st	42.28	43.64	43.15	43.11
2nd	106.95	110.86	108.73	108.64
3rd	164.07	179.45	168.84	166.05
4th	206.76	215.63	211.89	210.54
5th	302.76	336.17	326.43	321.53
6th	332.8	353.66	345.52	340.33

Table 13: Non Rotating Frequencies [Hz] (Case 1)

For the non rotating frequencies, the results obtained with plate or solid models are very close, as reported in tab.(13) and tab.(10). Nevertheless, even if the blade is slender, there are small differences in the rotating frequencies between solid and plate models probably because the blade thickness distribution near the hub and the clamped joint representation. From the results, it can be inferred that the blade is best represented by a solid model in this case. However, it is demonstrated, in accordance with literature [23], that shell models can be a

	CQUAD4		CQUAD8	
mode	coarse	fine	coarse	fine
1st	48.73	51.16	49.28	53.11
2nd	114.64	118.24	124.70	119.18
3rd	187.89	185.91	184.52	177.31
4th	220.28	223.21	230.27	221.71
5th	346.67	343.50	352.04	340.60
6th	365.85	361.09	369.69	350.92

Table 14: Rotating Frequencies [Hz] with $\Omega = 895$RPM (Case 1)

good approximation for preliminary analyses of rotating blades, their accordance to experimental data or solid models being better for thin thickness distributions.

6.3.2 Aerodynamic Analysis

The aerodynamic mesh is generated as already explained in sections 2.5 and 2.6 with *GAMBIT*®, different grids are developed because of the variable pitch angle of the blade. In particular, the number of the aerodynamic meshes is the same as the trimmed asymptotic velocities V_∞ related to the Penaud diagrams, because there is a perfect correlation between the blade pitch angles and the asymptotic velocities V_∞. In other words, there is a different aerodynamic mesh for every trimmed flight condition, reported in section 5.3.2, because the blade can be set at different pitch angles, so optimizing its aerodynamic behaviour (i.e. to avoid flow separation due to high angles of attack). Actually, every asymptotic velocity V_∞ generates a different wake helicoid (as explained in sec.(2.6)). In every grid created, the wake rolling is reproduced using the specific trimmed V_∞ and Ω, in order to reduce the sources of any errors. Tab.(15) reports the relationships between the asymptotic velocities V_∞ and the blade pitch angles.

Pitch Angle [deg]	V_∞ [m/s]
45	70
50	90
55	110
60	130
65	150
70	180
75	210

Table 15: Relationship between $\beta_{0\%}$ (at the root of the blade) and V_∞

In particular, the discretization adopted consist of nearly 180k nodes and 1M tetrahedrons for each mesh. The external mesh onto the aero-

dynamic body is refined at the leading and trailing edges in order to correctly represent the variation of pressure distribution. A good wake discretization is obtained with a medium-size uniform discretization. Fig.(50),fig.(51), fig.(52) and fig.(53) show samples of the comparison of the Mach and pressure coefficient distributions provided by the full potential scheme, S^T and *AeroX* (*AX*) Euler solver in some cases. Since the local Mach number almost reaches the sonic condition, the two solvers provide nearly the same solutions.

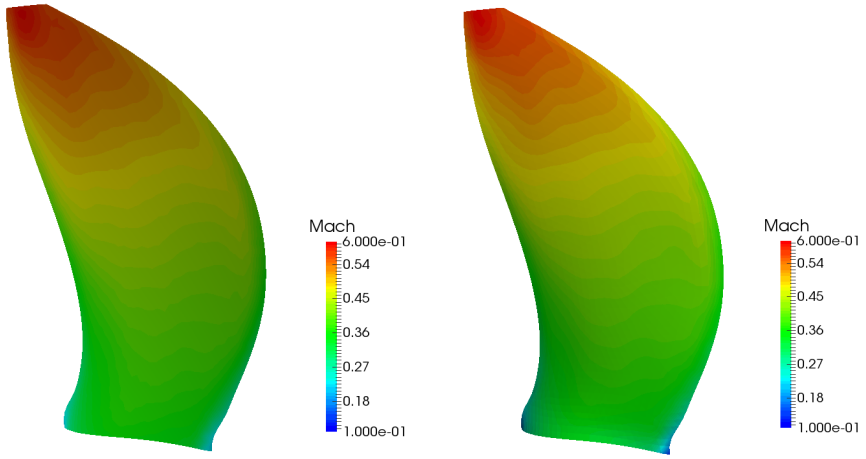

(a) Mach distribution obtained by S^T **(b)** Mach distribution obtained by *AX*

Figure 50: Mach distributions for $V_\infty = 70$ m/s at $h = 0$ km.

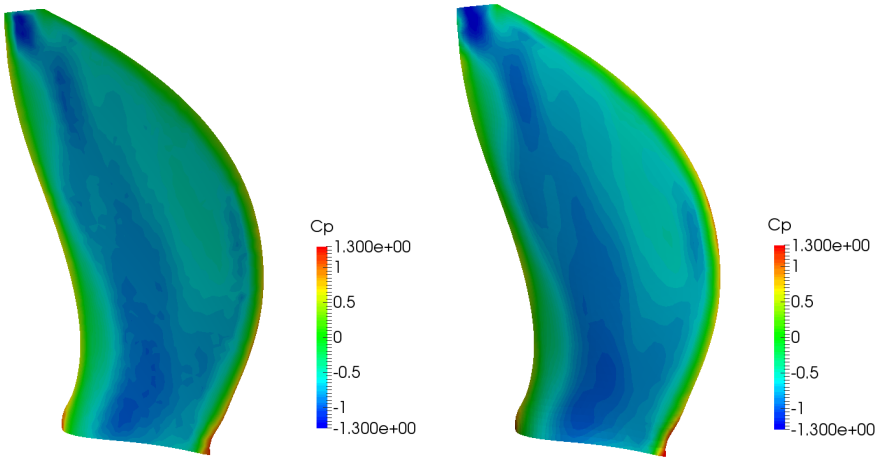

(a) Cp distribution obtained by S^T **(b)** Cp distribution obtained by *AX*

Figure 51: Cp distributions for $V_\infty = 70$ m/s at $h = 0$ km.

It is worth noting that the flight conditions are always subsonic except for highest pitch angles (or equivalently the highest trimmed asymptotic velocities V_∞) where the local Mach number can be at most

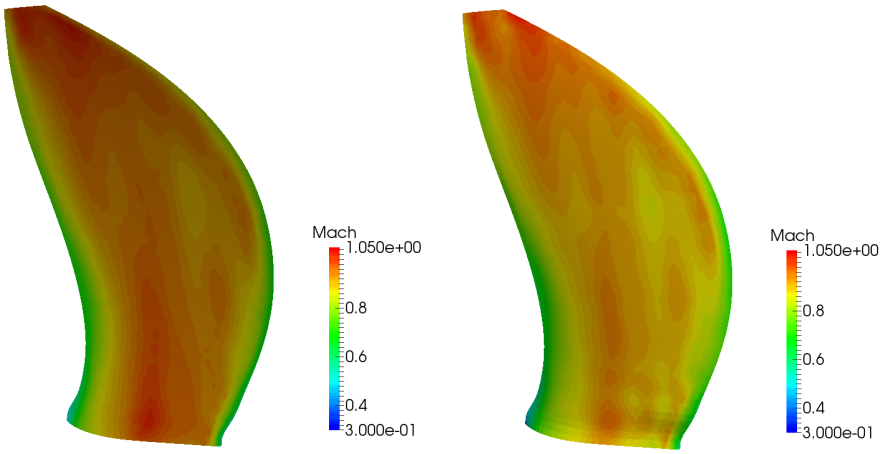

(a) Mach distribution obtained by S^T **(b)** Mach distribution obtained by AX

Figure 52: Mach distributions for $V_\infty = 205$ m/s at $h = 10$ km.

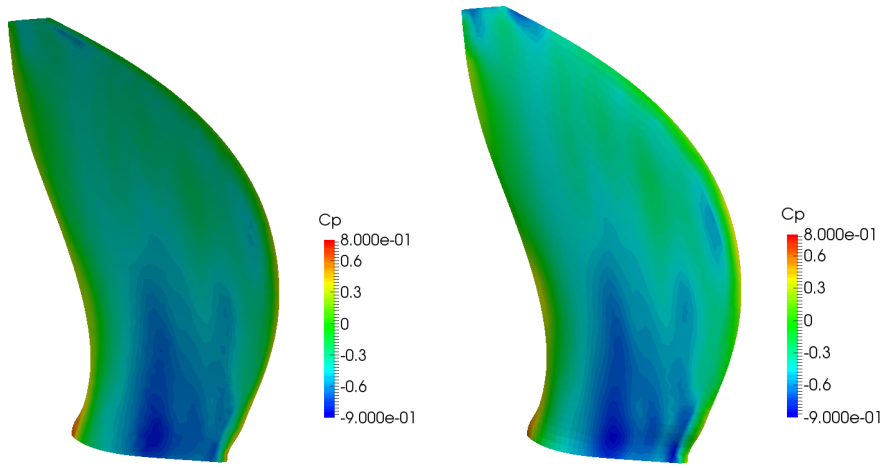

(a) Cp distribution obtained by S^T **(b)** Cp distribution obtained by AX

Figure 53: Cp distributions for $V_\infty = 202$ m/s at $h = 10$ km.

1.1. For this reason, the entropy correction developed in S^T had no appreciable effect because of the relatively weak downstream shock waves. Thanks to the "friendly" operating conditions, it is possible to state that the differences between the solutions obtained from S^T and AX are only imputable to the different numerical methods implemented. The rapid variation of the Cp distribution over the outward surface of the blade can be better approximated by using a finer grid around the leading and trailing edges, in fact a correct mesh generation will help in predicting the flow field around lifting bodies.

6.3.3 Aeroelastic Trim

Within the frame of rotating bodies, the main load acting on the blades is the centrifugal force but it is right to query if the steady aerodynamic load, which is a follower force, is strong enough to introduce non-negligible deformations. If it is not true, then eigenvalues and mode shapes can be quite different respect to the case in which only the centrifugal load acts. In this way, the static aeroelastic equilibrium has to be computed at every flight operating condition in order to correctly evaluate the blade deformation, the eigenvalues and the modal shapes before proceeding with the identification of the aerodynamic transfer functions $\mathbf{H_{am}}(k, M_\infty)$.

Recalling eq.(3.37)

$$\bar{\mathbf{K}} = \mathbf{K} + \mathbf{K_L} + \mathbf{K_G}, \tag{6.4}$$

where

$$\begin{aligned}
\mathbf{K} &= \int_{\mathcal{V}} \mathbf{B_{L0}}^T \mathbf{D} \mathbf{B_{L0}} d\mathcal{V}, \\
\mathbf{K_L} &= \int_{\mathcal{V}} \left(\mathbf{B_{L0}}^T \mathbf{D} \mathbf{B_{L1}} + \mathbf{B_{L1}}^T \mathbf{D} \mathbf{B_{L0}} + \mathbf{B_{L1}}^T \mathbf{D} \mathbf{B_{L1}} \right) d\mathcal{V}, \\
\mathbf{K_G} &= \int_{\mathcal{V}} \mathbf{B_{NL}}^T \mathbf{D} \mathbf{B_{NL}} d\mathcal{V},
\end{aligned}$$

the non-linear trim with the centrifugal force is

$$\bar{\mathbf{K}}(\mathbf{q})\, \mathbf{q} = \mathbf{F}_C. \tag{6.5}$$

Considering also the aerodynamic load, the equilibrium condition yields

$$\bar{\mathbf{K}}(\mathbf{q})\, \mathbf{q} = \mathbf{F}_C + \mathbf{F}_{aero}(\mathbf{q}), \tag{6.6}$$

which is a non-linear problem that must be solved by an iterative solution, so to update the stiffness matrix $\bar{\mathbf{K}}(\mathbf{q})$ and the aerodynamic load $\mathbf{F}_{aero}(\mathbf{q})$ at every step. In order to simplify such problem, only one step will be performed.
To this end, the non linear trim, eq.(6.5), is performed with the centrifugal load $\mathbf{F}_C$ so to obtain the solution $\mathbf{q}_0$. After that, the linearization of the steady aerodynamic virtual work, as explained in ref.[12], is evaluated

$$\delta W^{aero} = \delta \mathbf{q}^T \frac{1}{2} \rho V_\infty^2 \int_{\mathcal{S}} \mathbf{\Phi}^T C_p^0 \, (\vec{n}_0 + \Delta\vec{n}) \, d\bar{\mathcal{S}}, \tag{6.7}$$

where, $C_p^0 = C_p^0(\mathbf{x}|_{\mathcal{S}}, \bar{t})$ is the steady state pressure coefficient onto the blade surface $\mathcal{S}$, $\vec{n}_0$ is the undeformed normal and $\Delta\vec{n}$ takes into account the *follower* force contribution. Such term is due to the non-conservative behaviour of the aerodynamic force, which follows the motion of the body surface, being always oriented along its normal. Thus, the term containing $\Delta\vec{n}$ in eq.(6.7) provides a follower stiffness

matrix, usually called $\mathbf{K}_0^{aero}$. Eventually, the linearised static aeroelastic trim problem consists in, with an abuse of notation,

$$\left[\bar{\mathbf{K}}(\mathbf{q}_0) + \mathbf{K}_0^{aero}\right] \Delta\mathbf{q} = \frac{1}{2}\rho V_\infty^2 \int_S \mathbf{\Phi}^T C_p^0 \, \vec{n}_0 \, d\bar{S}, \tag{6.8}$$

in which the equilibrium with the centrifugal load is hidden in $\bar{\mathbf{K}}(\mathbf{q}_0)$. After computing the right hand side of eq.(6.8), the updated pre-strain stiffness and the aerodynamic follower matrices, a new eigenvalue problem is solved. In common practice, the pressure load can be added to *NASTRAN*® model with a *PLOAD* chart (i.e. a distributed follower load). The main purpose of this analysis is to determine changes in eigenvalues and eigenvectors with respect to those associated only to a centrifugal-loaded blade.

In this case, it is demonstrated that the effects of the aerodynamic loads are negligible with respect to those associated to the centrifugal force and so it is not required to perform the static aeroelastic equilibrium for every flight condition. In this way, the effectiveness of the linearization of the aerodynamic virtual work is proved because the non-linear problem of eq.(6.6) can be solved in only one step.
Tab.(16) reports the first 6 normal frequencies calculated for a blade pitch angle of 75° at a flight velocity $V_\infty = 210$ m/s and at an angular velocity of 895 RPM. Fig.(55) demonstrates that the modal shapes including the aerodynamic load are practically the same as those of only the centrifugal load acting (i.e. the differences are less than 1%).

mode	Cent+Aero	Cent
1st	49.13	49.09
2nd	116.98	116.85
3rd	182.59	182.49
4th	222.28	222.02
5th	345.24	345.26
6th	357.04	356.67

Table 16: Comparing Normal Frequencies [Hz] with or without the aerodynamic pressure load

As further verification, it is shown that eigenvectors of only centrifugal loaded blade are a good basis for representing the structural behaviour of the blade. The aerodynamic load is projected onto a reduced modal basis as

$$\mathbf{Q}_a = \frac{1}{2}\rho V_\infty^2 \int_S \mathbf{\Phi}^T C_p^0 \, \vec{n}_0 \, d\bar{S}, \tag{6.9}$$

where $\mathbf{Q}_a$ are the so-called steady state generalized aerodynamic forces. Then, the additional displacement field due to only aerodynamic forces can be approximated with

$$\mathbf{s} = \sum_{i=1}^{h} \frac{Q_{a,i}}{\mathcal{K}_i} \mathbf{\Phi}_i \tag{6.10}$$

where $\mathcal{K}_i$ are the generalized stiffness of centrifugal loaded blade. In this way, the influence of the follower aerodynamic stiffness matrix $\mathbf{K}_0^{aero}$ on the displacement field can be evaluated. The displacement field obtained from a *NASTRAN*® simulation with both aerodynamics and centrifugal loads is compared with that computed with eq.(6.10) (plus the displacement field of the centrifugal loaded blade only). Fig.(54) reports the relative error between the solutions obtained with a modal basis of 50 eigenvectors and with a non linear static analysis performed with NASTRAN®. From fig.(54), it can be inferred that the differences in the displacement field are very small (i.e. less than 2%), so to prove that the matrix $\mathbf{K}_0^{aero}$ is negligible also for the calculation of the displacement field and not only for the eigensolution.

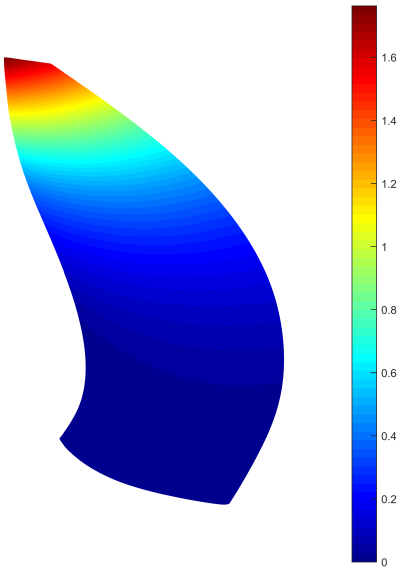

Figure 54: Relative error between the solutions calculated with the modal basis and with SOL 106 in NASTRAN®.

In conclusion, this analysis proves that the equilibrium condition is predominantly affected by the centrifugal load, so the static aeroelastic trim can be avoided because the aerodynamic loads do not have a strong influence on the eigenvalues, mode shape and deformed configuration of the blade. Such an approach is the common way in the literature.

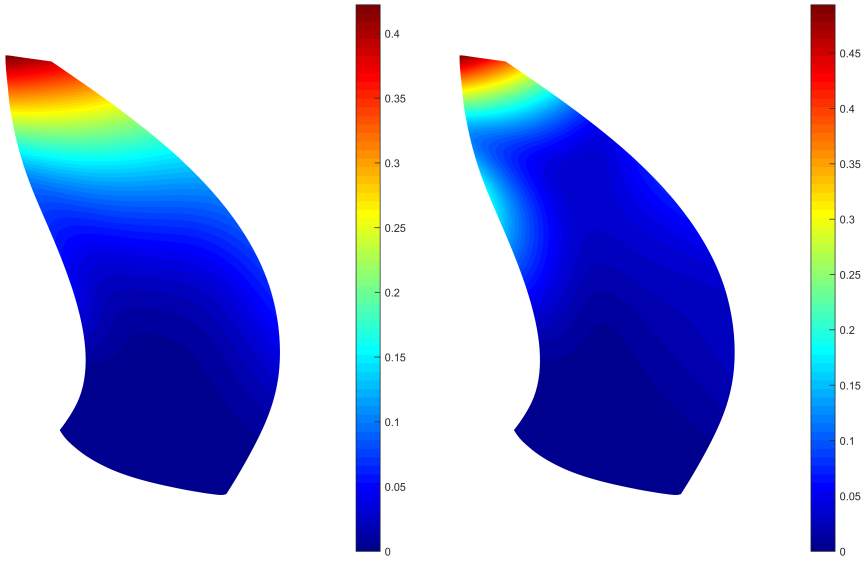

(a) *Error 1st Mode (%)).* **(b)** *Error 2nd Mode (%)).*

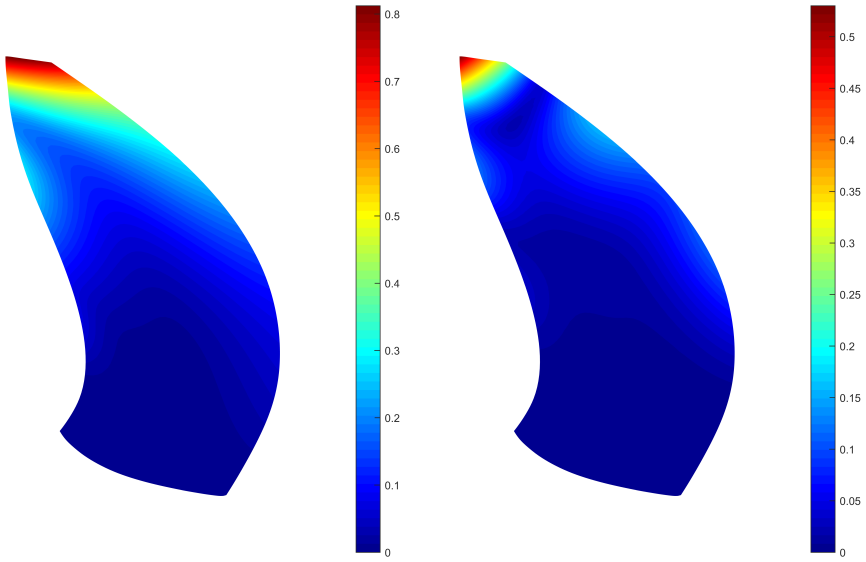

(c) *Error 3rd Mode (%)).* **(d)** *Error 4th Mode (%)).*

Figure 55: Relative error between mode shapes including or not the aerodynamic load.

6.3.4 Flutter Analysis

The aerodynamic transfer functions matrices resulting from a blended step input computed with AeroX (AX) and S^T at different asymptotic Mach numbers are shown in appendix B (for a single trimmed flight condition only). Once again, it is stressed that the aerodynamic transfer functions are calculated for each trimmed flight condition (i.e. T = D) and for every altitude considered. Considering that those reference data are obtained on the same aerodynamic grid but with different numerical schemes, the agreement is satisfactory in almost all cases. After performing a parametric stability analysis of the linear(ized) time-invariant aeroelastic dynamic system it is possible to build the $V-\omega$ and $V-g$ diagrams shown in fig.(56), fig.(57) and fig.(58). The flutter boundaries are investigated at different altitudes so verifying the critical conditions in a plausible flight envelope. In agreement with [60], there are no classical flutter instabilities for this aeroelastically optimized blade.
The values of the damping g obtained with the full-potential code S^T are more conservative than those obtained with the Euler solver AX. It can also be observed that the values of g are lower than those of common wing test cases, e.g. [72]. This fact was already justified by ref.[5, 6].
It can be inferred that the centrifugal force has greater importance than the aerodynamic load, so the effects of the latter have less influence on the (in)stability of the system.

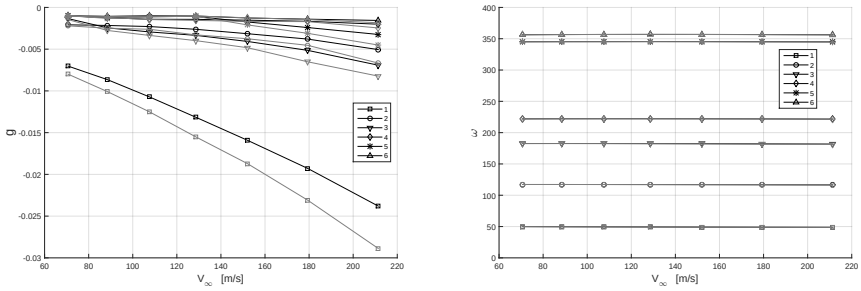

(a) (b)

Figure 56: $V - g$ and $V - \omega$ diagrams at 0 meters

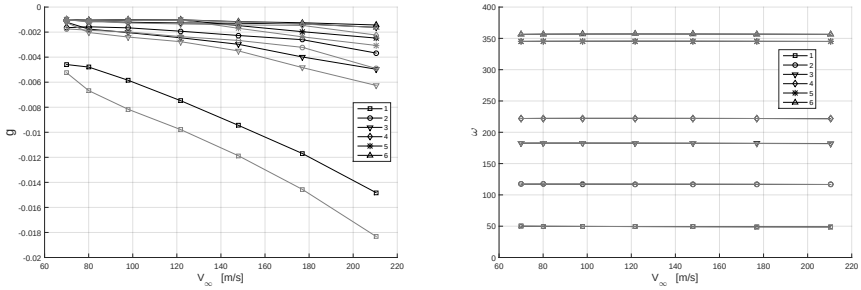

(a) (b)

Figure 57: $V - g$ and $V - \omega$ diagrams at 5.000 meters

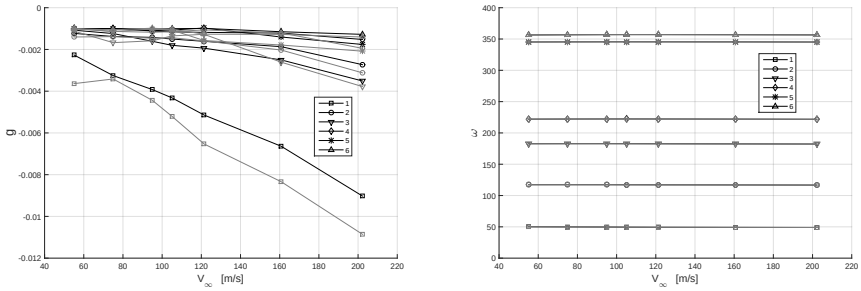

(a) (b)

Figure 58: $V - g$ and $V - \omega$ diagrams at 10.000 meters

6.4 TEST CASE 4

After demonstrating the capabilities of the S^T solver, a flutter analysis of a CROR is performed. The blade shape is the same as the previous case [60]. The developed CROR is composed of two 8-bladed stages placed at a distance of $d/D = 0.25$, in accordance to the guidelines explained in ref.[63, 64]. The internal radius is $r = 0.76$ m and the disk diameter is $D = 3.7041$ m. The aerodynamic meshes and the flight conditions are the same as sec.(6.3).

6.4.1 Aerodynamic Analyses

As already stated, the flight conditions are the same as the test case of sec.(6.3) so verifying the existence of flutter instabilities in a plausible flight envelope. First, the assumption of equally partitioned thrust between both rotors at each asymptotic velocity V_∞ must be set adjusting the blade pitches by means of the transpiration boundary conditions. In every case, the pitch angles of the blades of the front and after rotor are modified of about two degrees at most with respect to the values reported in the first column of tab.(15). Tab.(17) reports the pitch angles at the root of the blade for every operating condition. It can be inferred that the blade pitch angle for the two rotors is always similar, probably because of the particular twist angle distribution β along the span-wise direction of the blade of [60].

	SRP	Front Rotor	After Rotor
V_∞ [m/s]	$\beta_{0\%}$ [deg]	$\beta_{0\%}$ [deg]	$\beta_{0\%}$ [deg]
70	45	44.9	44.8
90	50	50	50.1
110	55	55	55.5
130	60	60	60.7
150	65	65	66.3
180	70	71.1	71.3
210	75	77.5	76.5

Table 17: Pitch Angles $\beta_{0\%}$ for CROR.

6.4.2 Processing of the Aerodynamic Modal Responses

Since the system is periodic due to the combination of the rotational speed and the number of blades of the two rotors, the classical theory for predicting instabilities for Linear-Time-Invariant (LTI) system cannot be used. In the case of CROR which is a Linear-Time-Periodic (LTP) system, more complex theory, e.g. Floquet, must be used to correctly predict the instability boundaries. Moreover, the cascade effects due to

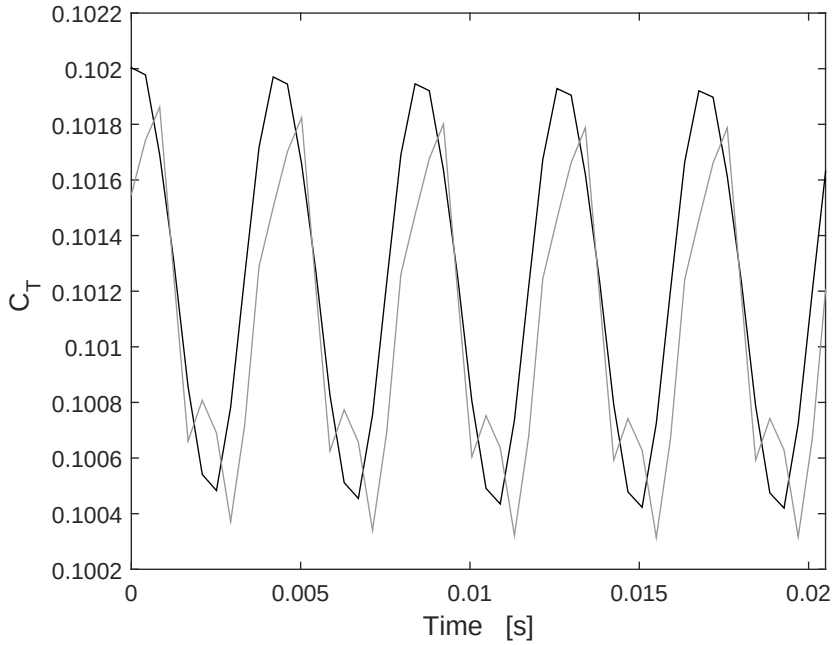

Figure 59: Thrust coefficient C_T of the front (●) and after (●) rotors at the asymptotic velocity $V_\infty = 130$ m/s.

non-zero IBPA must be accounted for, as in the case of the linearised flutter analysis of turbomachines [19]. Such effects modify the damping g of the system and they are not always negligible as reported in ref.[5]. In this way, the aerodynamic transfer matrices $\mathbf{H_{am}}$ will depend not only on the reduced frequency k and the asymptotic Mach number M_∞ but also on the IBPA σ. Besides, the $\mathbf{H_{am}}(\bar{\sigma}, k, M_\infty)$ for a particular flight condition and IBPA ($\bar{\sigma}$) is a 2×2 block matrix, whose main diagonal contains the aerodynamic influences between the blades of the same rotor while the antidiagonal contains the mutual aerodynamic influences between the blades of the two stages.
However, as already explained in sec.(5.1), only simulations with 0° IBPA are carried out. The limitations of such results, in particular for the case of CROR, do not allow a complete view of the stability region but are useful to understand the behaviour of such systems. Furthermore, thanks to the small variation of the aerodynamic loads around the equilibrium condition, a simplification of the above cited theory can be exploited. Systems that shows small variation around an equilibrium state are also called, in the literature, *small varying systems*. In particular, ref.[67] explains the conditions required for a linear stability of the response of a LTP system. A very simple technique deriving from the theory proposed in [67] is now presented.

In the field of classical aeroelasticity, the hardest thing to do is the correct identification of the aerodynamic transfer functions $\mathbf{H_{am}}(k, M_\infty)$ in the frequency domain. Since the aerodynamic simulations are done

in the time domain, a Fourier transform of the output signals must be performed. However, if the signal is periodic in some way, the frequencies spectrum presents many peaks as the found harmonics. In particular, the multiples of the fundamental harmonic appear:

$$\omega_i = \Omega \, N \, i, \qquad \text{for } i = 1,2,... \tag{6.11}$$

where Ω is the angular velocity expressed in rad/s and N is the total number of blades of the two rotors (this is true if the two stage of propeller have the same number of blades). Fig.(60) shows the magnitude of the black signal reported in fig.(59). In this case, since $\Omega = 895$ RPM, the fundamental harmonic is 238 Hz.

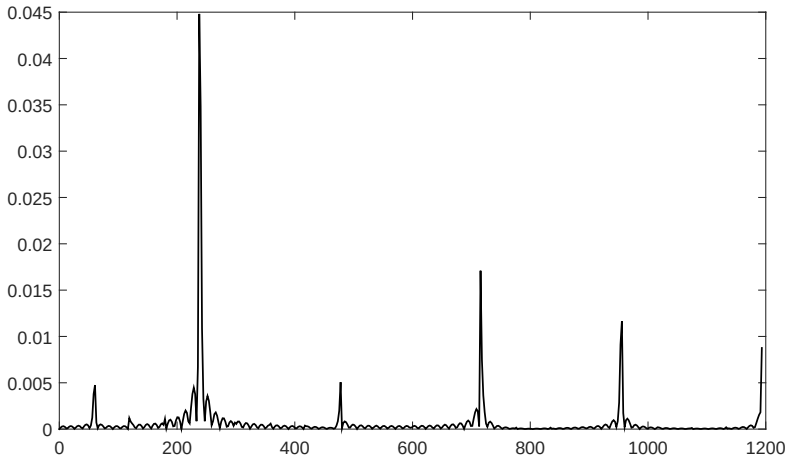

Figure 60: Example of the frequency spectrum.

So, the idea is to build the aerodynamic transfer functions $\mathbf{H_{am}}(k, M_\infty)$ without the peaks of the various harmonics so obtaining a non-periodic signal in the time domain. In other words, the frequencies spectrum has to be filtered in some way in order to represent the variation of the aerodynamic responses respect to the equilibrium solution (which is periodic in time).

There are various technique for filtering a signal. The most simple idea is to use a low pass filter of appropriate order, i.e. Butterworth, with a cut-off frequency lower than the fundamental harmonic $\omega_1 = \Omega \, N$. Even if the phase lag is recovered with high order filters, the reduction of the modulus of the transformed signal at low frequencies still persists. Besides, the frequency spectrum is badly approximated in the neighbouring of the fundamental harmonic so losing primary informations about the variation of the aerodynamic load respect to its steady-periodic state, as can be inferred by fig.(61).

Thus, an interpolation of the frequency spectrum seems to be the best solution. Actually, the real and the imaginary part of the $\mathbf{H_{am}}(k, M_\infty)$ are interpolated separately as showed in fig.(62). Moreover, only the

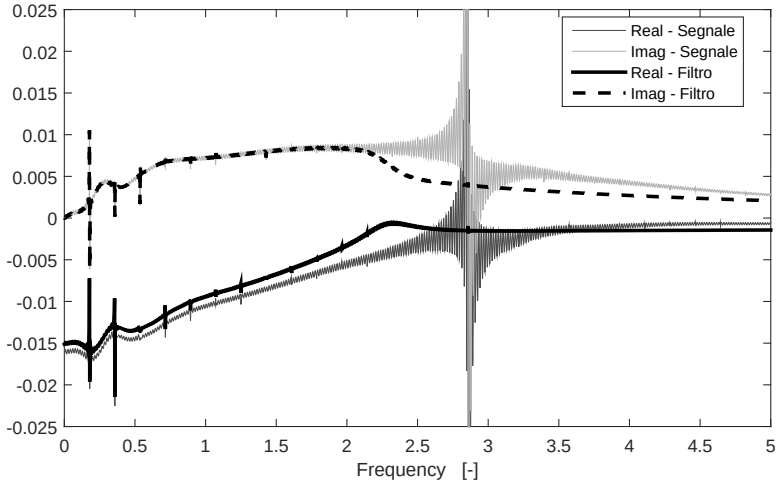

Figure 61: Example of the filtering of an element of the matrix $\mathbf{H_{am}}(k, M_\infty)$ with a Butterworth filter of 15th order and cut-off reduced frequency of 2.27.

reduced frequency spectrum lower than $k = 10$ is interpolated because the higher frequency values are not needed in the flutter analysis, i.e. $k_{max} = 5$.

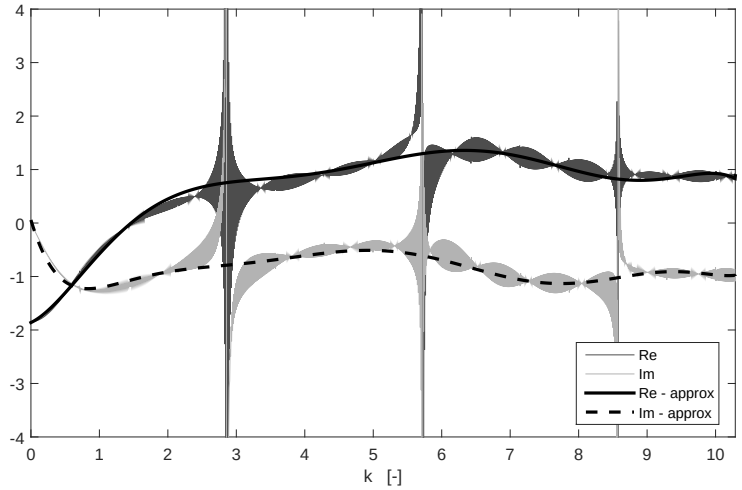

Figure 62: Example of the interpolation of an element of the matrix $\mathbf{H_{am}}(k, M_\infty)$.

6.4.3 Flutter Analyses

The interpolation of the aerodynamic responses above discussed is used to build the aerodynamic transfer matrices $\mathbf{H_{am}}(0°, k, M_\infty)$. The maximum value of the reduced frequency is $k_{max} = 5$ and the am-

plitudes of the inputs are calculated with eq.(5.8). The flutter analysis exploits the non linear root-tracking of sec.(5.3) and it is carried out only at an altitude of 0 m. Moreover, it is proven that different results can be obtained in relation with the beginning of the blended step input in the oscillation period of the aerodynamic load. The transient of such input must be lesser than one period so simulating nearly a step. In particular, the chosen transient lasts about an half of a period. In this way, the assumption of a "frozen" stability analysis is valid because the change of the aerodynamic boundary conditions is very fast. Thus, the results are obtained for two different beginnings of the input, i.e. at $\Phi = 0°$ and $\Phi = 180°$. In other words, $\Phi = 0°$ means that the input starts at the beginning of the oscillating period while $\Phi = 180°$ means the half of the oscillating period.

The credibility of the results cannot be proven because there are no such studies reported in the literature. The assumption of a *small varying system* is legitimated by the small variation of the aerodynamic loads as shown in the case of fig.(59). The results are reported in fig.(63) and fig.(64). It can be noted that the third mode (torsional) of the rear rotor assumes positive values of the damping g. In particular, the flutter velocities are $V_f = 212$ m/s and $V_f = 202$ m/s for $\Phi = 0°$ and $\Phi = 180°$, respectively.

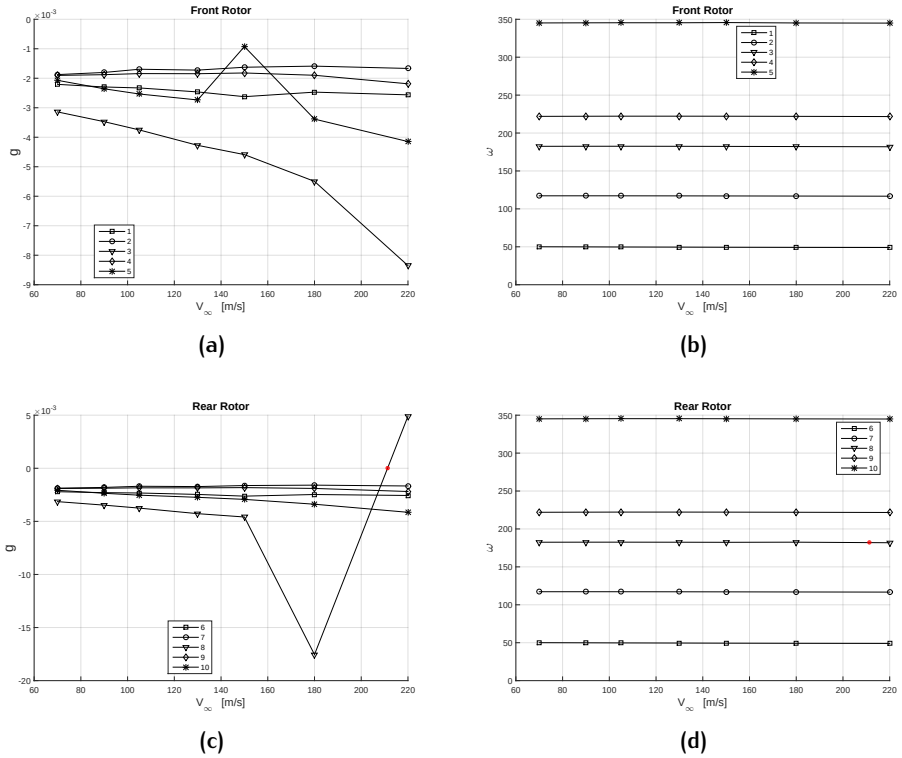

Figure 63: $V - g$ and $V - \omega$ with $\Phi = 0°$

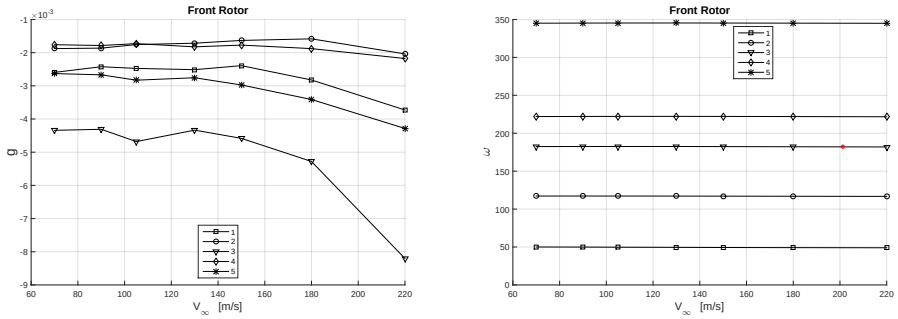

(a)

(b)

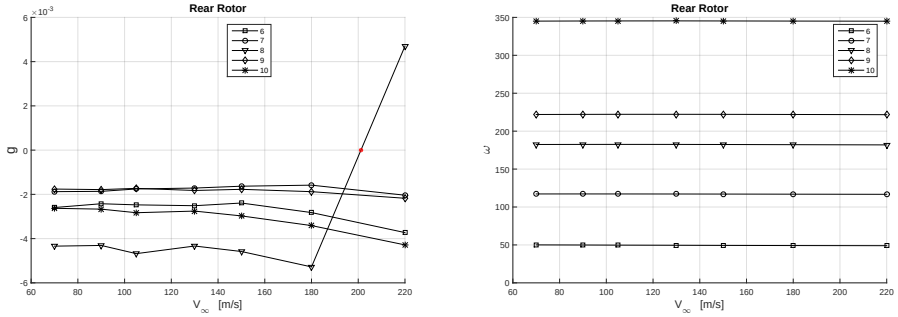

(c)

(d)

Figure 64: $V - g$ and $V - \omega$ with $\Phi = 180°$

7

CONCLUDING REMARKS AND FUTURE DEVELOPMENTS

The structural sub-system is modelled with the Finite-Element (FE) solvers NASTRAN and ANSYS. The comparison of natural frequencies and mode shapes performed using both tetrahedral and shell element models proves that the structural dynamic is well approximated by shell element models, especially when second order elements are employed. In this way, the accordance with the experimental results is even better when the thickness distributions of the blade are small.

Among the innovative contributions it is worthwhile to remark the *ghost* technique proposed for simulating simultaneously the flow field around two lifting bodies in relative motion. This technique enables to re-use the grids of a single rotating propeller for the simulation of a contra-rotating open rotor without introducing more complicated strategies, e.g. Chimera methods and Mixing Planes.

The effectiveness of the proposed aeroelastic analysis is successfully assessed by tackling a set of realistic dynamic problems and by comparing the results with reference experimental and numerical data available in the literature and with the results obtained by the Euler flow solver *AeroX* [44, 58]. In particular, the capabilities of the aerodynamic solver S^T are pointed out comparing the results obtained from uRANS and Euler simulations of ref.[63]. The results so obtained shows a good accordance with those of the uRANS simulations even if local Mach numbers reach high transonic values. Even if the entropy correction implemented is turned off, the solutions obtained are very similar to those reported in the literature. Such a fact proves that the entropy correction is mandatory for simulating transonic flows in 2D analyses (as reported in ref.[53]) but needs some improvements to be more effective in 3D, especially for rotating problems. It is also showed that the *ad hoc* technique for computing the flow field around CROR gives good correlations with more sophisticated strategies, i.e. Chimera method. The blade pitch angles obtained for an equally partitioned thrust between the two rotor are in accordance to those obtained by ref.[63]. Thus, the transpiration technique can be an effective tool not only for simulating the generalized aerodynamic responses $\mathbf{Q}_a(t)$ but also for varying the blade pitch.

Successively, the benchmark taken by [22], including structural, aero-

dynamic and flutter computations, is addressed. This test case is used as a validation problem of the strategies employed for computing the aerodynamic transfer functions $\mathbf{H_{am}}(k, M_\infty)$ and the eigenvalues of the reduced order aeroelastic system. The results obtained from S^T and AeroX are less in accordance because the high transonic regime in combination with high angles of attack along the span-wise direction of the blade. The reliability of the proposed aerodynamic solver decreases when simulating such flows and, probably, even the Eulerian solution is far away from the reality because the high angles of attack are symptoms of separating flow.
However, the flutter analysis conducted with the K-E method gives very acceptable results in accordance with the literature. It can be inferred that in this case the effects related to the transonic flows have a small influence on the flutter prediction.
Eventually, two complete studies of the patent blade of [60] are surveyed with the awareness gained by the previous validation process. The static aeroelastic trim analysis conducted for this blade proves that the effects of the steady aerodynamic loads are negligible with respect to those of the centrifugal force in terms of eigenvalues, mode shapes and deformed configurations. Thus, such analysis can be avoided so performing a trim with the centrifugal load only as it is usually done in the literature. The flutter boundaries of both propfan and contra-rotating open rotor are evaluated in a plausible flight envelope. The stability of the propfan is verified in accordance with the patent. The damping values g are always smaller (i.e. lower than 0.1) with respect to those of common wings. Such a fact is well documented in the literature; so other forms of damping are needed in order to augment the stability region of such systems. For example, the introduction of some sort of absorbing supports can be a possible solution.
Eventually, the flutter stability of the CROR is investigated with justified assumptions related to the resources available for the present work. Such system, which responses are time-periodic, can be considered as a small-varying system so enabling a *frozen* stability analysis. The results so obtained will be justified in future works because more complex strategies, e.g. *Floquet* theory, are required to perform such analyses.

In conclusion, more improvements can be exploited so allowing a more detailed flutter analysis because the time-periodic responses of such system. In addiction, other interesting problems can be faced, e.g. the aeroacustic prediction of noise emissions. To this end, many opportunities for future development can be identified:

- The development of a toolbox for the analysis of the aeroacustic field around a moving lifting body. The solver S^T can be modified for such application in order to solve the non-homogeneous wave equation proposed by Ffowcs Williams-Hawkings [70]. In

this way a complete analysis of the aeroacustic sub-system can be performed;

- The development of the solver S^T in the frequency domain. Thanks to the time-implicit integration scheme implemented, the exact Jacobian matrices allow to simulate the CROR directly in the frequency domain. In this way, the linear(ised) harmonic analysis of rotors, including the effect of periodic boundary conditions with phase lag (i.e. Inter Blade Phase Angles, IBPA, different from 0°), can be easily performed, as in the case of turbomachines. With such an improvement, the aerodynamic transfer functions $\mathbf{H_{am}}(\sigma, k, M_\infty)$ will depend also by the IBPA. To this end, *ad hoc* stability theory for time-varying system (i.e. periodic) can be exploited to perform a more reliable flutter analysis.

A

VALIDATION OF "GHOST TECHNIQUE"

A 2D problem is investigated in order to validate the technique explained in sec.4.5. Thanks to the simplicity of the investigated test cases, it is proved the validity and the limits of the proposed method to solve the flow field around two lifting bodies in relative motion (i.e. two NACA 0012 airfoils with a unitary chord). Two different configurations are investigated with the asymptotic conditions reported in tab.(18).

P_∞	101325 Pa
ρ_∞	1.225 kg/m^3
M_∞	$0.5 \div 0.7$
α	2°

Table 18: Asymptotic condition for the test cases. The polytropic ideal gas model ($\gamma = 1.4$) is employed.

As already explained in sec.(4.5), the peculiar idea of this method consist in simulating the flow field around two lifting bodies by exploiting the *superimposition principle*.
The so-called *real body* refers to the aerodynamic body effectively modelled within the mesh, while the *ghost* is only fictitious.
The ghost body appears only as a contour in the discretized domain where the density $\rho(\mathbf{x}, t)$ and velocity potential $\phi(\mathbf{x}, t)$ fields have to be evaluated. Such values are used to modify the boundary conditions on the real body at the next time step with a slightly modified *transpiration* technique, sec.(4.5.1).
The numerical procedures are described as follows with the help of fig.(65) which represents the simple 2D test case of sec.(A.1). At each time step $\bar{t}$, two problems are solved in succession:

- *Simulation 1*: the *ghost body* is placed below the *real body*. The solution is calculated by adding the transpiration contribution eq.(4.15) (obtained from the previous time step) onto the *real body*. After solving the non-linear system of sec.(2.2.2), the transpiration contribution onto the *ghost body* is updated and it will be used in "simulation 2";
- *Simulation 2*: the *ghost body* is placed above the *real body*. The solution is calculated by adding the transpiration contribution

eq.(4.15) (obtained from "simulation 1") onto the *real body*. After solving the non-linear system of eq.s reported in sec.(2.2.2), the transpiration contribution is updated and it will be used in "simulation 1" of the next time step.

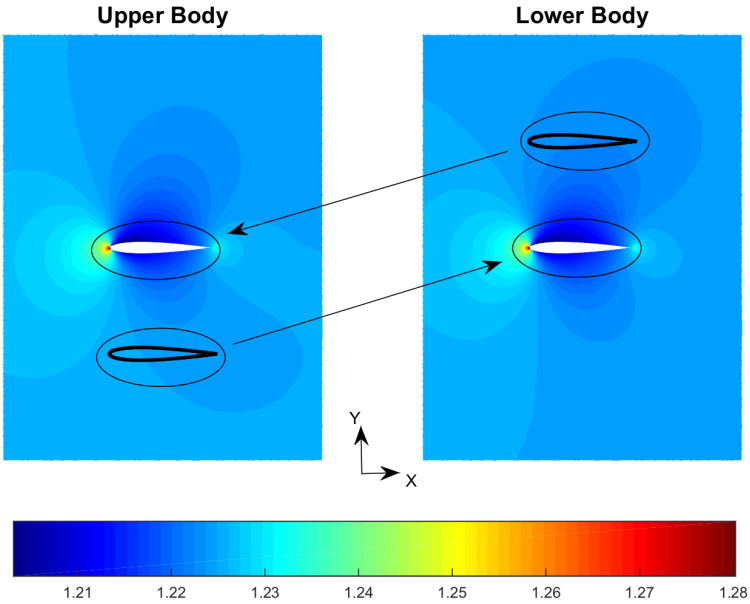

Figure 65: The density field $\rho(\boldsymbol{x}, \bar{t})$ of each STEP is represented.

A.1 ALIGNED AIRFOILS

The flow field around two NACA 0012 airfoils placed one above the other is solved numerically. The spatial domain is represented in fig.(66) and it contains two perfectly aligned airfoils placed at a distance of 1 m from each other ("Mesh 1").

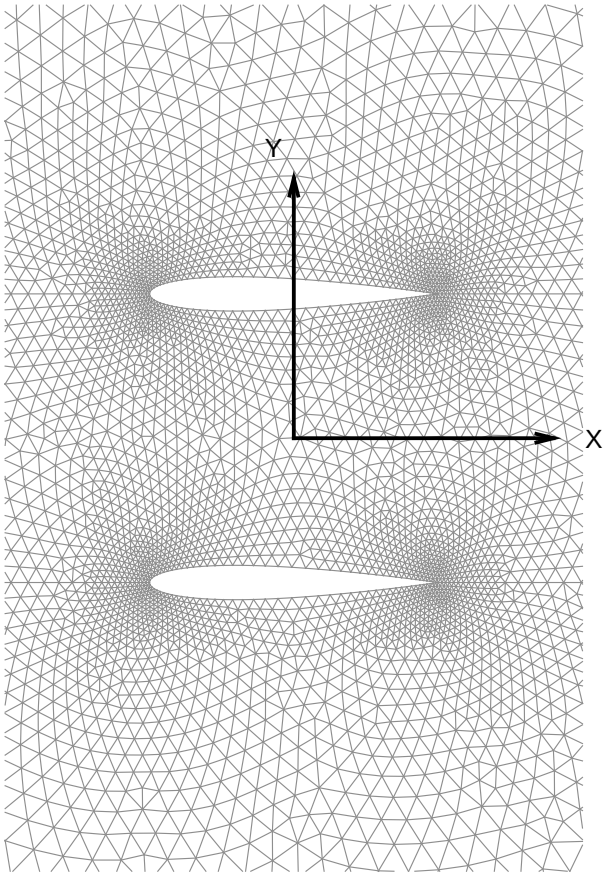

Figure 66: Detail of grid with two NACA.

Another mesh contains only one airfoil centred in the axis origin ("Mesh 2") and the so called *ghost technique* is applied as previously explained.

Results

In this section, the results obtained from numerical simulations are reported. It can be seen a good correlation in the subsonic flight condition. However, the airfoils are too close when simulating the transonic condition: the system acts like a supersonic nozzle with the generation

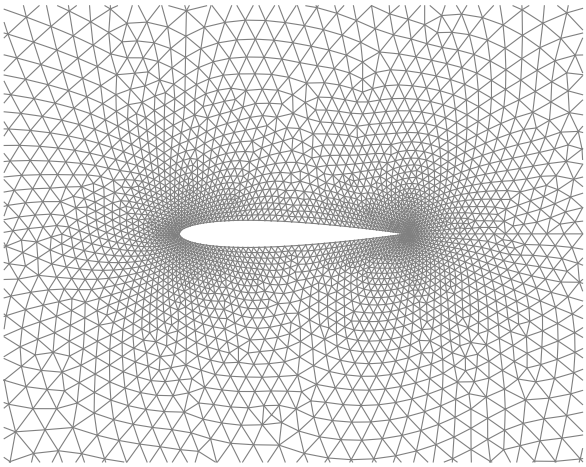

Figure 67: Detail of the grid with one NACA (XY view).

of a shock at the trailing edges (exhaust). It can be inferred the importance of the relative position between the two bodies. Thus, this extreme condition has to be avoided in the case of contra-rotating blades. Fortunately, the relative position between blades is periodic and the overlap position last for short periods of time.

In next figures are represented the density fields $\rho(\mathbf{x}, t)$ near the bodies and Cp distributions. Eventually, the values of lift, drag and pitch moment (referred to 25% of chord) coefficients are reported in tab.(19) and tab.(20).

	Reference Mesh		*Ghost Technique*	
	Body UP	Body LOW	Body UP	Body LOW
CL	$3.08 \cdot 10^{-1}$	$1.43 \cdot 10^{-1}$	$3.01 \cdot 10^{-1}$	$1.41 \cdot 10^{-1}$
CM	$8.59 \cdot 10^{-3}$	$-1.72 \cdot 10^{-2}$	$7.30 \cdot 10^{-3}$	$-1.68 \cdot 10^{-2}$

Table 19: Aerodynamic coefficients for $M_\infty = 0.5$. The *Reference Mesh* gives the exact solution while the *Ghost Technique* exploits the so called formulation.

	Reference Mesh		*Ghost Technique*	
	Body UP	Body LOW	Body UP	Body LOW
CL	1.016	$-4.59 \cdot 10^{-1}$	$4.85 \cdot 10^{-1}$	$5.07 \cdot 10^{-2}$
CM	$2.46 \cdot 10^{-1}$	$-2.73 \cdot 10^{-1}$	$1.66 \cdot 10^{-2}$	$-3.63 \cdot 10^{-2}$

Table 20: Aerodynamic coefficients for $M_\infty = 0.7$. The *Reference Mesh* gives the exact solution while the *Ghost Technique* exploits the so called formulation.

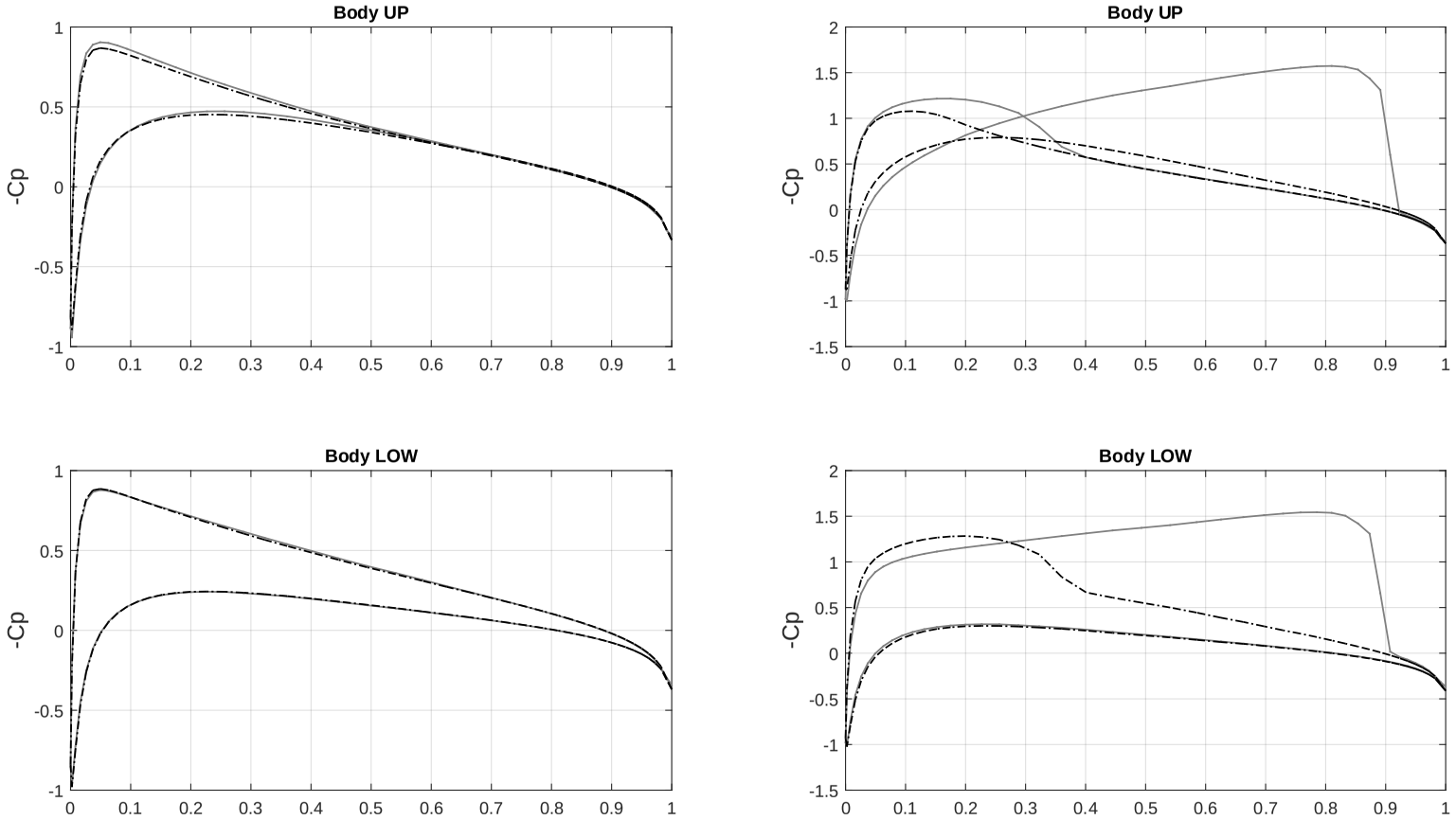

(a) $M_\infty = 0.5$ **(b)** $M_\infty = 0.7$

Figure 68: Cp distributions over the airfoils. The *reference* solution is (●) while the *ghost* one is dashed-(●).

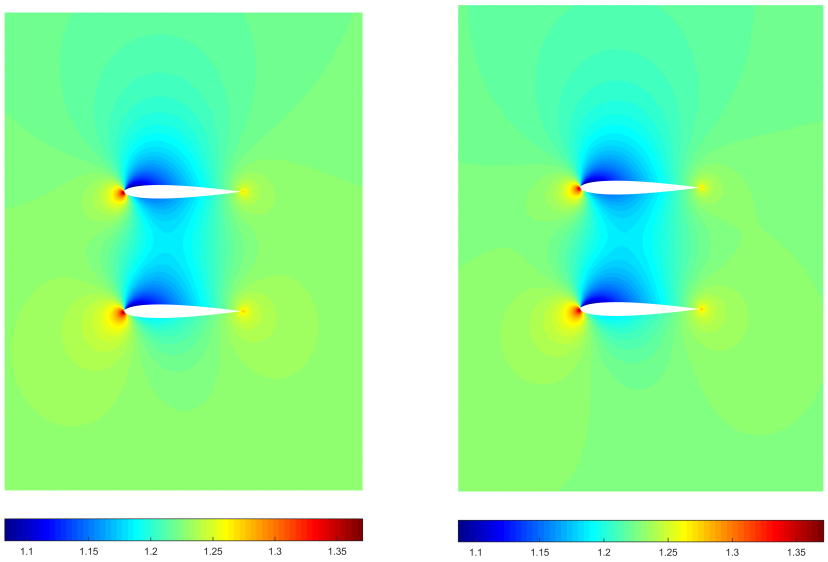

(a) *Reference*. **(b)** *Ghost*.

Figure 69: Density Fields for $M_\infty = 0.5$

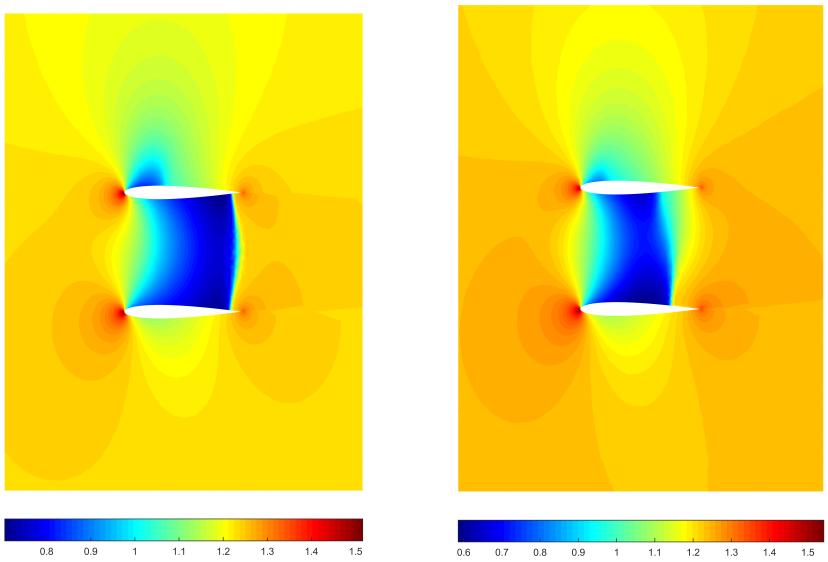

(a) *Reference*. **(b)** *Ghost*.

Figure 70: Density Fields for $M_\infty = 0.7$

A.2 MISALIGNED AIRFOILS

The flow field around two misaligned NACA 0012 airfoils with chord $c = 1$ m is solved numerically in order to better understand the limitation of the proposed technique. The spatial domain is represented in fig.(71) and it contains two misaligned airfoils placed at a distance of 1 m from each other.

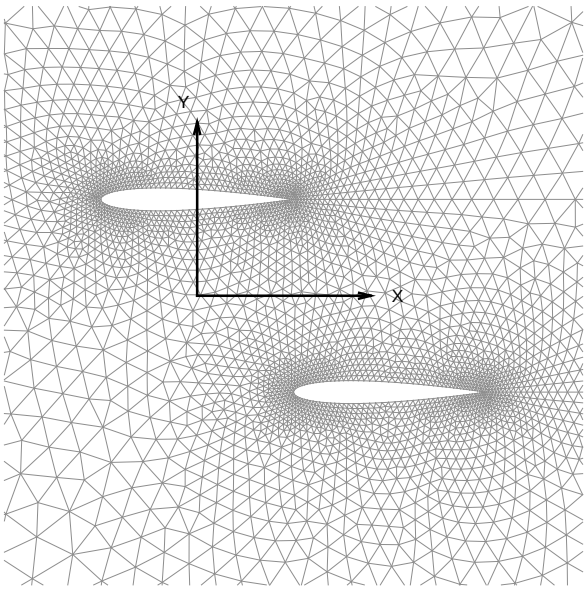

Figure 71: Detail of grid

Another mesh contains only one airfoil centred in the axis origin (i.e. the mesh of fig.(67)) and the so called *ghost technique* is applied as explained in sec.4.5.

Results

In this section, the results obtained from numerical simulations are reported. It can be seen that the obtained solutions are very similar in the subsonic flight condition. The transonic condition is better respect the case of two aligned NACA. It can be inferred that the technique works like a "superimposition of effects", so it gives a very good approximation if the coupling between the two separated flow field solutions is not too strong as the transonic case of the previous section, fig.(70).

In next figures are represented the density fields $\rho(\mathbf{x}, t)$ near the bodies and Cp distributions. Eventually, the values of lift, drag and pitch moment (referred to 25% of chord) coefficients are reported in tab.(21) and tab.(22).

	Reference Mesh		*Ghost Technique*	
	Body UP	Body LOW	Body UP	Body LOW
CL	$3.91 \cdot 10^{-1}$	$1.93 \cdot 10^{-1}$	$3.99 \cdot 10^{-1}$	$2.09 \cdot 10^{-1}$
CM	$3.19 \cdot 10^{-3}$	$-1.69 \cdot 10^{-3}$	$2.66 \cdot 10^{-3}$	$-1.85 \cdot 10^{-3}$

Table 21: Aerodynamic coefficients for $M_\infty = 0.5$. The *Reference Mesh* gives the exact solution while the *Ghost Technique* exploits the so called formulation.

	Reference Mesh		*Ghost Technique*	
	Body UP	Body LOW	Body UP	Body LOW
CL	$5.79 \cdot 10^{-1}$	$1.98 \cdot 10^{-1}$	$5.66 \cdot 10^{-1}$	$2.28 \cdot 10^{-1}$
CM	$1.05 \cdot 10^{-3}$	$-3.35 \cdot 10^{-3}$	$2.19 \cdot 10^{-3}$	$-5.32 \cdot 10^{-3}$

Table 22: Aerodynamic coefficients for $M_\infty = 0.7$. The *Reference Mesh* gives the exact solution while the *Ghost Technique* exploits the so called formulation.

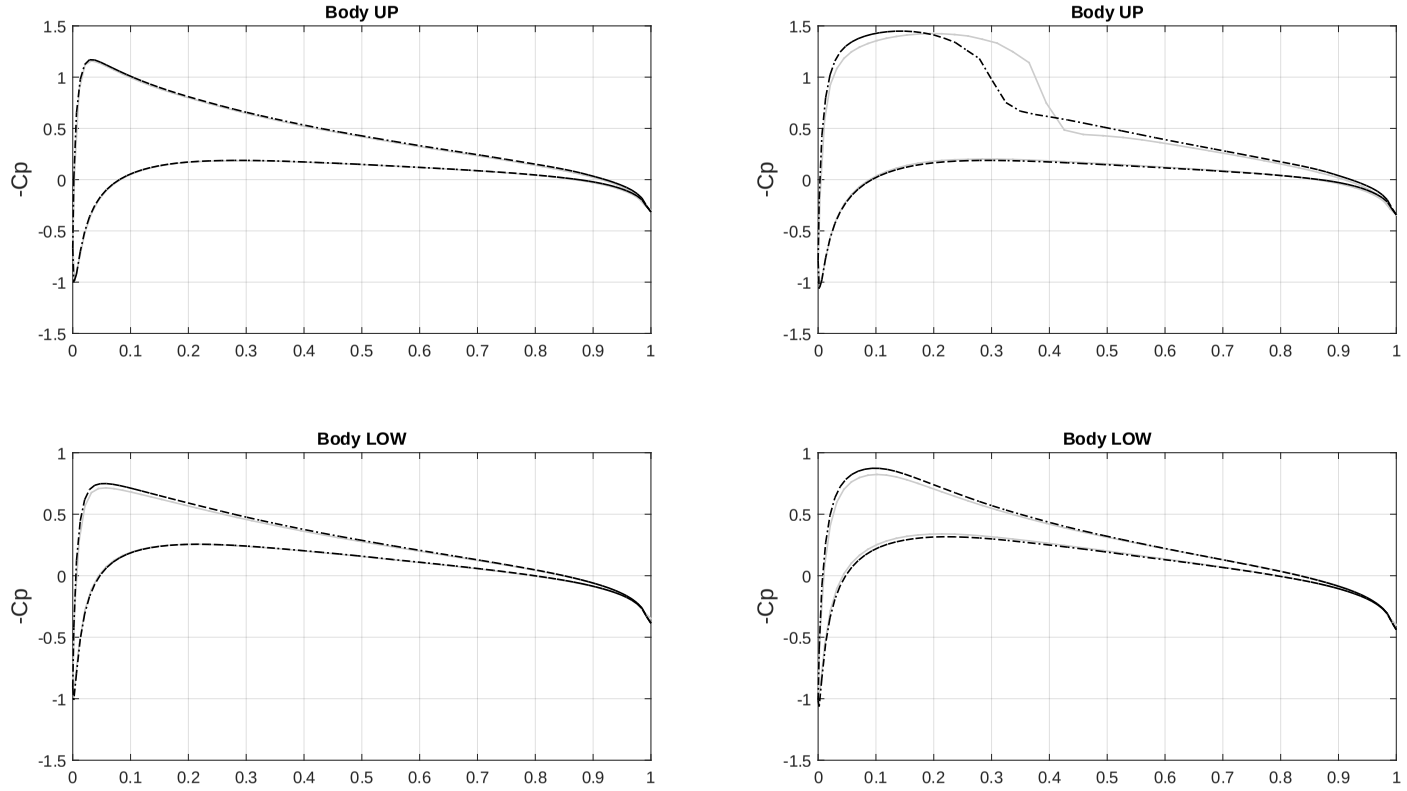

(a) M=0.5 **(b)** M=0.7

Figure 72: Cp distributions over the airfoils. The *reference* solution is (●) while the *ghost* one is dashed-(●).

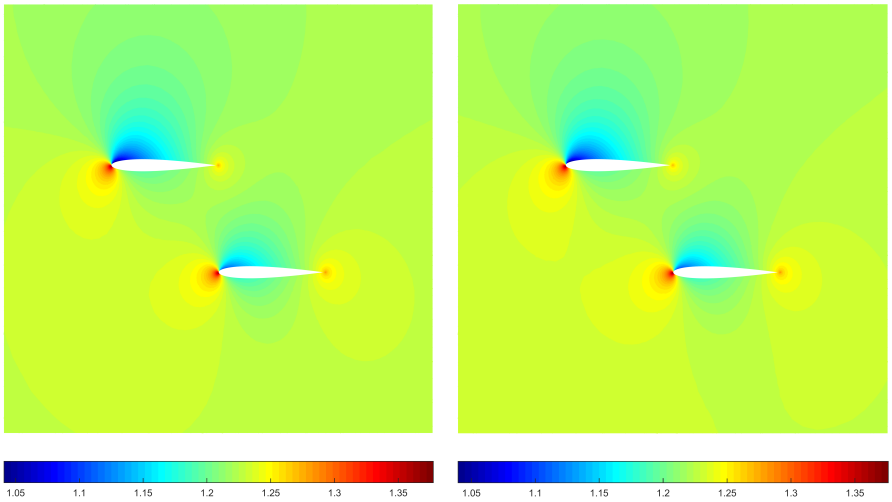

(a) *Reference*. **(b)** *Ghost*.

Figure 73: Density Fields for $M_\infty = 0.5$

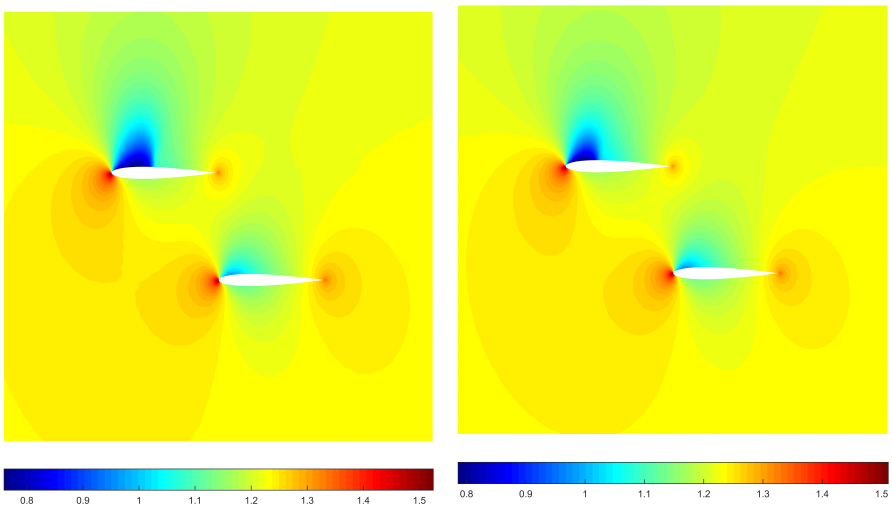

(a) *Reference*. **(b)** *Ghost*.

Figure 74: Density Fields for $M_\infty = 0.7$

B

AERODYNAMIC TRANSFER FUNCTIONS

In this Appendix, the Generalized Aerodynamic Forces GAFs $\mathbf{Q}_{am}(t)$ of sec.(6.3) obtained with S^T and AeroX are reported. For each trimmed condition, it is evaluated a matrix of 6×6 dimensions, derived from 6 structural modes. There are also the related aerodynamic transfer functions $\mathbf{H_{am}}(k, M_\infty)$.

B.1 NUMERICAL RESULTS

Fig.(75) shows the aerodynamic responses $\mathbf{Q}_{am}(t)$ to a blended step input explained in sec.(5.2). Fig.(76) shows the aerodynamic transfer matrix $\mathbf{H_{am}}(k, M_\infty)$ within the interval $k \in [0, 1]$.

The maximum value of the reduced frequency is $k_{max} = 5$ with a reference chord $L_a = 0.40$ m. In this appendix there are reported only the aerodynamic responses and matrix for the asymptotic velocity $V_\infty = 70$ m/s. The adimensional length τ of the transient of the blended step input is:

$$\tau = \frac{2\pi}{k_{max}} \frac{V_\infty}{L_a}. \tag{B.1}$$

The amplitudes of the inputs are calculated with eq.(5.8).

A moderate accordance is observed between the results obtained with S^T and AeroX. The differences can be probably imputed to different numerical schemes implemented (in particular, the aeroelastic interface method).

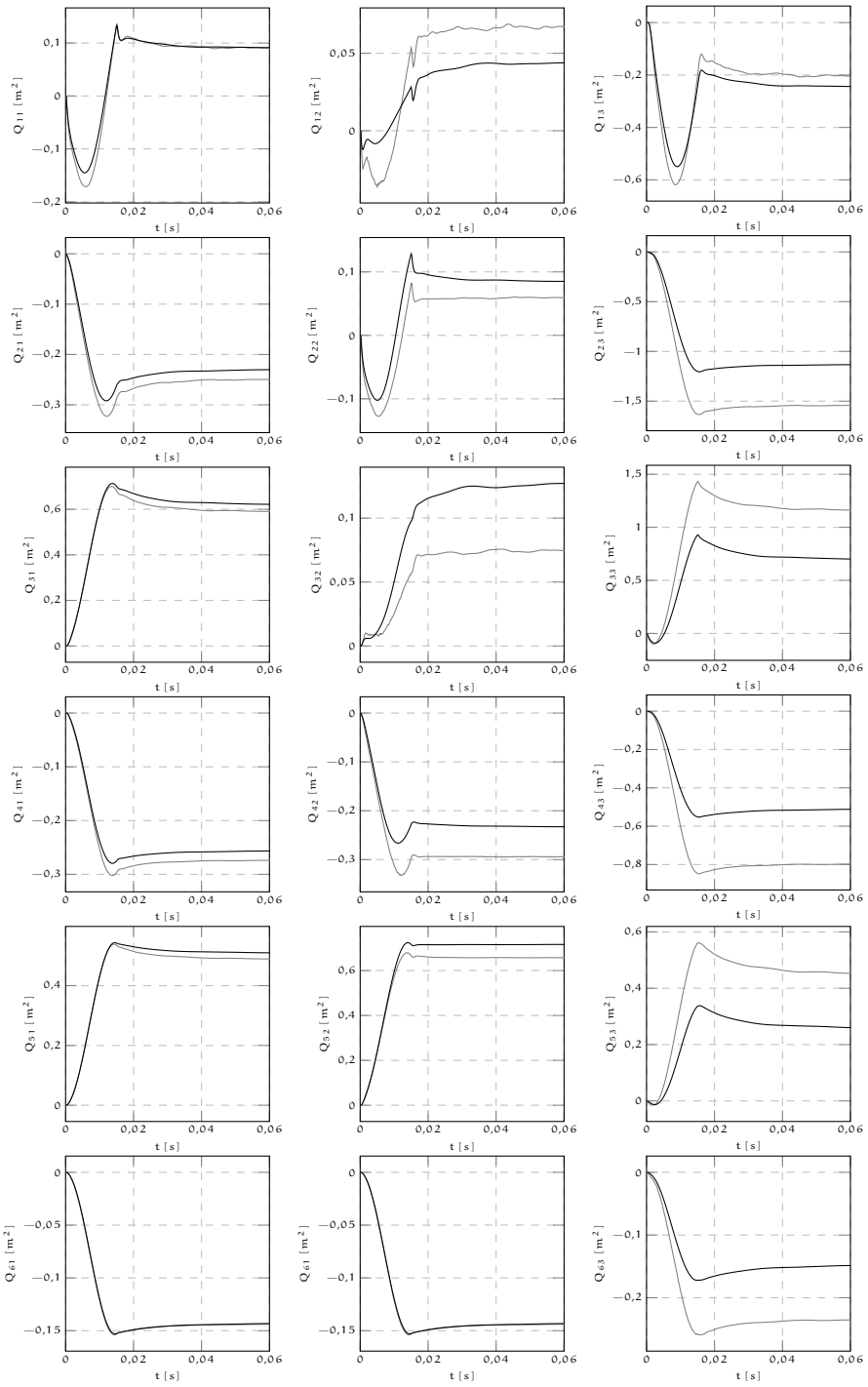
Q11 [m²]
Q12 [m²]
Q13 [m²]
Q21 [m²]
Q22 [m²]
Q23 [m²]
Q31 [m²]
Q32 [m²]
Q33 [m²]
Q41 [m²]
Q42 [m²]
Q43 [m²]
Q51 [m²]
Q52 [m²]
Q53 [m²]
Q61 [m²]
Q61 [m²]
Q63 [m²]
t [s]

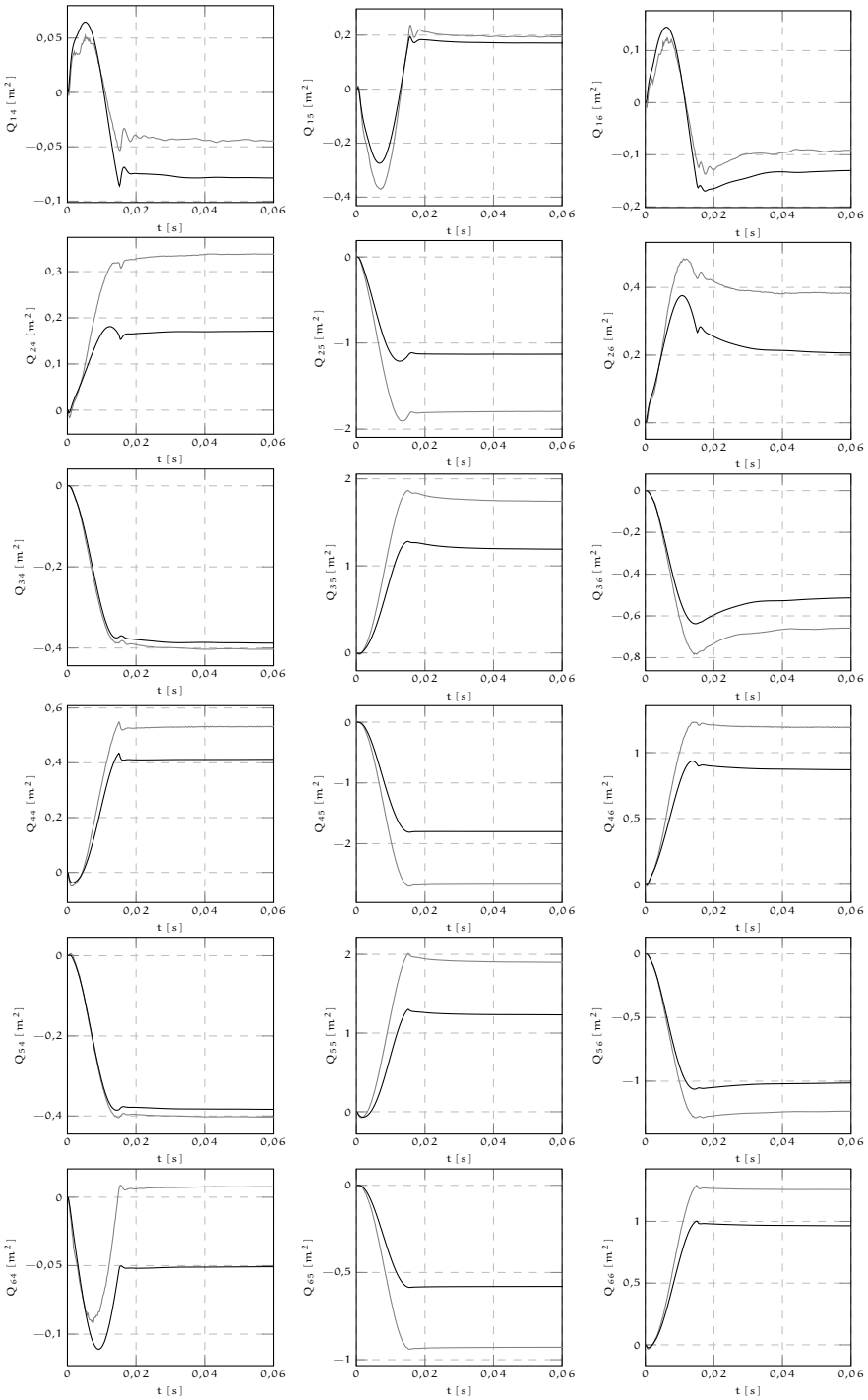

Figure 75: Comparison of the aerodynamic transfer functions matrix $\mathbf{Q_a m}(t)$ computed with S^T (●) and AeroX (●) at $V_\infty = 70$ m/s.

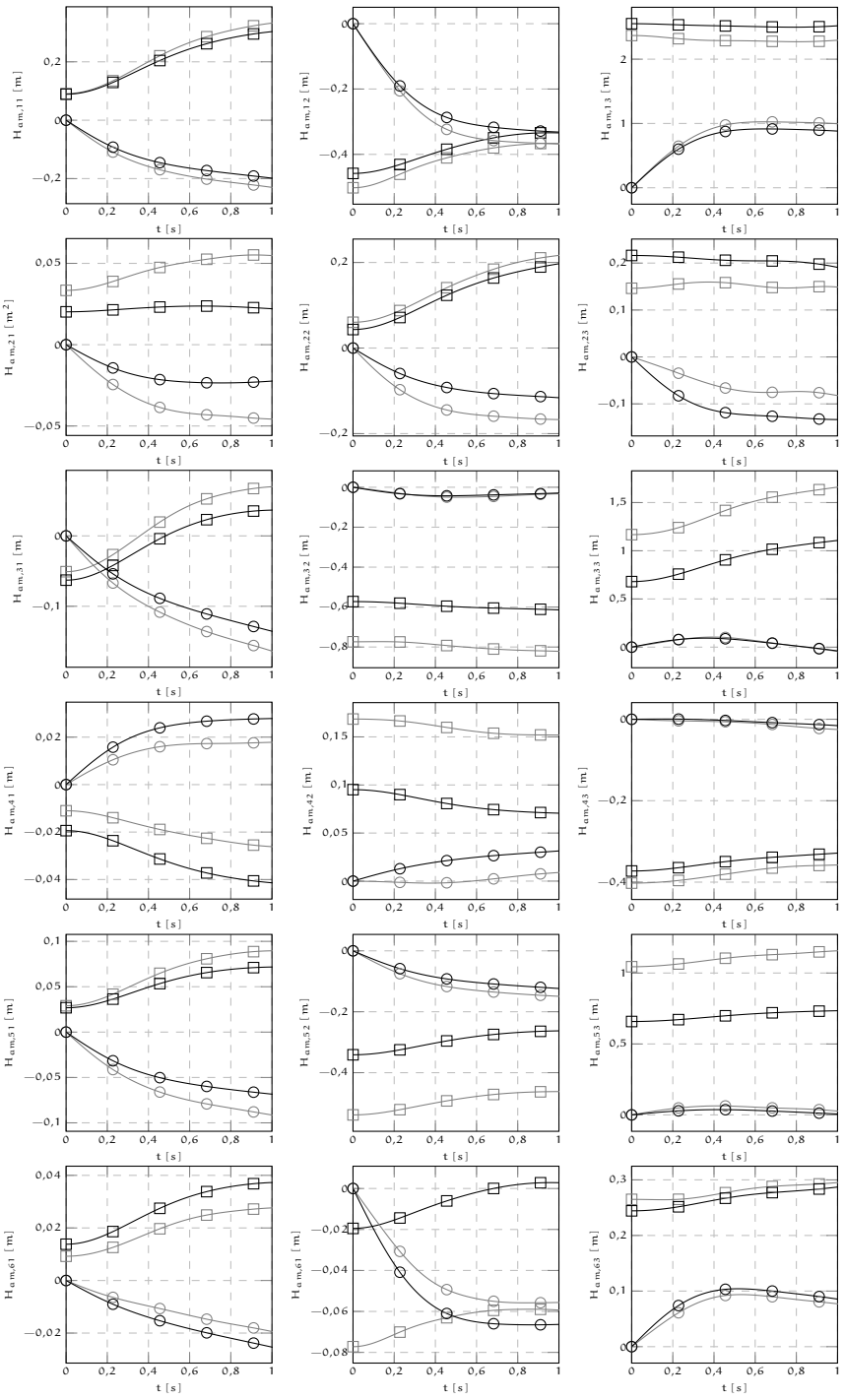
$H_{a\,m,11}$ [m]
$H_{a\,m,12}$ [m]
$H_{a\,m,13}$ [m]
$H_{a\,m,21}$ [m^2]
$H_{a\,m,22}$ [m]
$H_{a\,m,23}$ [m]
$H_{a\,m,31}$ [m]
$H_{a\,m,32}$ [m]
$H_{a\,m,33}$ [m]
$H_{a\,m,41}$ [m]
$H_{a\,m,42}$ [m]
$H_{a\,m,43}$ [m]
$H_{a\,m,51}$ [m]
$H_{a\,m,52}$ [m]
$H_{a\,m,53}$ [m]
$H_{a\,m,61}$ [m]
$H_{a\,m,61}$ [m]
$H_{a\,m,63}$ [m]
t [s]

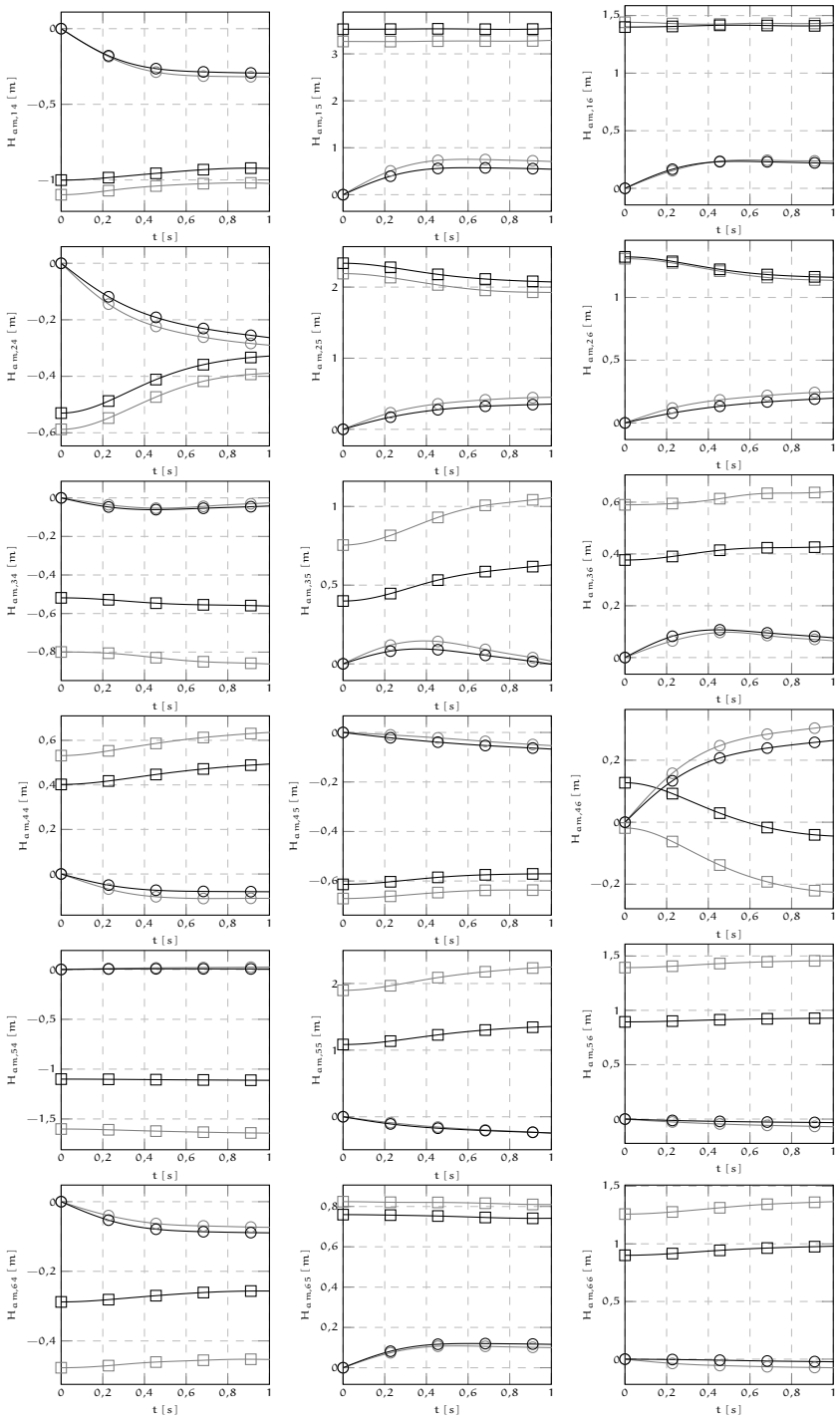

Figure 76: Comparison of the aerodynamic transfer functions matrix $\mathbf{H_a m}(k, M_\infty)$ computed with S^T (●) and AeroX (●) at $V_\infty = 70$ m/s. The marker of the real part is the square, while that of the imaginary part is the circle.

REFERENCES

[1] R.K. Agarwal and J.E. Deese. "Euler calculations for flowfield of a helicopter rotor in hover". In: *Journal of Aircraft* 24.4 (1987), pp. 231–238.

[2] Airbus. *Global Market Forecast, Future Journeys 2013*. Tech. rep. 2013. URL: www.airbus.com/company/market/forecast/.

[3] ANSYS Mechanical APDL. "release 14.0". In: *ANSYS Ltd* (2012).

[4] W.E. Arndt. "Propfans go full scale". In: *Aerospace America* (1984).

[5] R. August. "Vibration and flutter analysis of the SR-7L large-scale propfan". In: *In NASA, Lewis Research Center, Lewis Structures Technology* 1 (1988). URL: www.ntrs.nasa.gov/archive/nasa/casi.ntrs.nasa.gov/19880008652.pdf.

[6] R. August and K. Kaza. "Vibration, performance, flutter and forced response characteristics of a large-scale propfan and its aeroelastic model". In: (1988). URL: www.ntrs.nasa.gov/archive/nasa/casi.ntrs.nasa.gov/19890000672.pdf.

[7] R. August and K.R. Kaza. "Vibration, performance, flutter and forced response characteristics of a large-scale propfan and its aeroelastic model". In: (1988). URL: www.ntrs.nasa.gov/archive/nasa/casi.ntrs.nasa.gov/19890000672.pdf.

[8] Klaus-Jürgen Bathe. *Finite element procedures*. Klaus-Jurgen Bathe, 2006.

[9] J.M. Besson and D. Petot. "Comportement dynamique d'un propfan". In: *Aéronautique et l'astronautique* 111 (1985), pp. 35–44.

[10] R.T. Biedron and J.L. Thomas. "Recent enhancements to the fun3d flow solver for moving-mesh applications". In: *AIAA Paper* 1360 (2009), p. 2009. URL: www.ntrs.nasa.gov/archive/nasa/casi.ntrs.nasa.gov/20090007605.pdf.

[11] L.C. Billman et al. "Large scale prop-fan structural design study. Volume 2: Preliminary design of SR-7". In: (1988). URL: www.ntrs.nasa.gov/archive/nasa/casi.ntrs.nasa.gov/19900000728.pdf.

[12] R.L. Bisplinghoff, H. Ashley, and R.L. Halfman. *Aeroelasticity*. Courier Corporation, 2013.

[13] B.M. Brooks. "Acoustic measurements of three Prop-Fan models". In: (1980).

[14] L. Cavagna et al. "Efficient application of CFD aeroelastic methods using commercial software". In: *International Forum on Aeroelasticity and Structural Dynamics 1FASD-2005*. Citeseer. 2005.

[15] G. Chesshire and W.D. Henshaw. "Composite overlapping meshes for the solution of partial differential equations". In: *Journal of Computational Physics* 90 (1990), pp. 1–64.

[16] R. Chipman and A. Jameson. "Alternating-direction implicit algorithm for unsteady potential flow". In: *AIAA Journal* 20.1 (1982), pp. 18–24.

[17] R.W. Cornell and E.A. Rothman. "Structural Design and Analysis of Prop-Fan Blades". In: (1979).

[18] J. Donea et al. "Arbitrary lagrangian-eulerian methods". In: *Encyclopedia of Computational Mechanics* (2004).

[19] N. Donini. "Aeroelasticity of turbomachines linearized flutter analysis". MA thesis. Politecnico di Milano, 2012.

[20] T.D. Economon, F. Palacios, and J.J. Alonso. "Optimal shape design for open rotor blades". In: *AIAA paper* 3018 (2012), p. 2012. URL: www.adl.stanford.edu/papers/AIAA-2012-3018.pdf.

[21] V. Elchuri, A.M. Gallo, and S.C. Skalski. "NASTRAN documentation for flutter analysis of advanced turbopropellers". In: (1982). URL: www.ntrs.nasa.gov/archive/nasa/casi.ntrs.nasa.gov/19840007085.pdf.

[22] V. Elchuri and G.C.C. Smith. "Flutter analysis of advanced turbopropellers". In: *AIAA journal* 22.6 (1984), pp. 801–802.

[23] V. Elchuri and G.C.C. Smith. "NASTRAN flutter analysis of advanced turbopropellers". In: (1982). URL: www.ntrs.nasa.gov/archive/nasa/casi.ntrs.nasa.gov/19840006080.pdf.

[24] T. Fanion, M. Fernández, and P. Le Tallec. "Deriving adequate formulations for fluid-structure interaction problems: from ALE to transpiration". In: *Revue Européenne des éléments finis* 9.6-7 (2000), pp. 681–708.

[25] H.D. Gans. *Structural optimization including centrifugal and Coriolis effects*. Tech. rep. DTIC Document, 1988. URL: www.dtic.mil/dtic/tr/fulltext/u2/a196873.pdf.

[26] M. Geradin and N. Kill. "A new approach to finite element modelling of flexible rotors". In: *Engineering Computations* 1.1 (1984), pp. 52–64.

[27] T. Gerhold. "Overview of the hybrid RANS code TAU". In: *MEGAFLOW-Numerical Flow Simulation for Aircraft Design*. Springer, 2005, pp. 81–92.

[28] V. Giavotto et al. "Anisotropic beam theory and applications". In: *Computers & Structures* 16.1 (1983), pp. 403–413.

[29] H. Guillard and C. Farhat. "On the significance of the geometric conservation law for flow computations on moving meshes". In: *Computer Methods in Applied Mechanics and Engineering* 190.11 (2000), pp. 1467–1482.

[30] R.D. Hager and D. Vrabel. *Advanced turboprop project*. Tech. rep. National Aeronautics and Space Administration, Cleveland, OH (USA). Lewis Research Center, 1988.

[31] R.W. Harris and R.D. Cuthbertson. "UDF/727 flight test program". In: *Proc. of 23rd AIAA/SAE/ASME/ASEE Joint Propulsion Conference*. 1987. URL: www.arc.aiaa.org/doi/pdf/10.2514/6.1987-1733.

[32] H.J. Hassig. "An approximate true damping solution of the flutter equation by determinant iteration". In: *Journal of Aircraft* 8.11 (1971), pp. 885–889.

[33] C. Hirsch. *Numerical Computation of Internal and External Flows: The Fundamentals of Computational Fluid Dynamics*. Vol. 1. Butterworth-Heinemann, 2007.

[34] M. Hirschbein et al. "Structural and aeroelastic analysis of the SR-7L propfan". In: (1985). URL: www.ntrs.nasa.gov/archive/nasa/casi.ntrs.nasa.gov/19870012840.pdf.

[35] D.G. Holmes and S.S. Tong. "A three-dimensional Euler solver for turbomachinery blade rows". In: *Journal of Engineering for Gas Turbines and Power* 107.2 (1985), pp. 258–264.

[36] C. Lambert. "Aviation and Environment - Open Rotor Engines". In: *SBAC,[Online]* (2012). URL: www.sustainableaviation.co.uk/wp-content/uploads/open-rotor-engine-briefing-paper.pdf.

[37] F. Lane. "System mode shapes in the flutter of compressor blade rows". In: *Journal of the Aeronautical Sciences* 23.1 (1956).

[38] J.G. Leishman. *Principles of Helicopter Aerodynamics*. Cambridge university press, 2006.

[39] M.J. Lighthill. "On displacement thickness". In: *Journal of Fluid Mechanics* 4.4 (1958), pp. 383–392.

[40] A.C. Limache and E.M. Cliff. "Aerodynamic sensitivity theory for rotary stability derivatives". In: *Journal of aircraft* 37.4 (2000), pp. 676–683. URL: www.arc.aiaa.org/doi/pdf/10.2514/2.2651.

[41] B.H. Little et al. "Propfan Test Assessment (PTA): Flight Test Report". In: (1989). URL: www.ntrs.nasa.gov/archive/nasa/casi.ntrs.nasa.gov/19900002423.pdf.

[42] A. Madrane, A. Raichle, and A. Stuermer. "Parallel Implementation of a Dynamic Unstructured Chimera Method in the DLR Finite Volume TAU-code". In: (2004), pp. 524–534.

[43] B. Magliozzi and B.M. Brooks. "Advanced turbo-prop airplane interior noise reduction-source definition". In: *Final Report Hamilton Standard, Windsor Locks, CT.* 1 (1979).

[44] L. Mangani et al. "Comparison of acceleration techniques on CFD open-source software for aerospace applications". In: *AIAA journal* (2015).

[45] P. Mantegazza and C. Cardani. "An iterative technique to compute flutter speed through the simultaneous solution of each aeroelastic mode and frequency at increasing speed". In: *Aerotecnica Missili Spazio* 54 (1975), pp. 286–291.

[46] P. Mantegazza and C. Cardani. "Continuation and direct solution of the flutter equation". In: *Computers & Structures* 8.2 (1978), pp. 185–192.

[47] M. Martegani. "Un Metodo per il Calcolo del FLutter Linearizzato in Regime Transonico". MA thesis. Politecnico di Milano, 2003.

[48] P. Middleton. "Frugal, fast, but fractious prop-fan technology". In: *Flight International* 126 (1984), pp. 113–116.

[49] L. Morino and M. Gennaretti. "Boundary integral equations in aerodynamics". In: *Applied Mechanics Reviews* 46.8 (1993), pp. 445–466.

[50] D. Muffo et al. "Interface Velocity Consistency in time-accurate flow simulations on dynamic meshes". In: *Politecnico di Milano* (2007).

[51] Ganapathy Venkata Narayanan and KRV Kaza. "ASTROP2 users manual: a program for aeroelastic stability analysis of propfans". In: (1991). URL: www.ntrs.nasa.gov/archive/nasa/casi.ntrs.nasa.gov/19910019313.pdf.

[52] H.E. Neumann et al. "An analytical and experimental comparison of the flow field of an advanced swept turboprop". In: *AIAA* 189 (1983). URL: www.ntrs.nasa.gov/archive/nasa/casi.ntrs.nasa.gov/19830005790.pdf.

[53] A. Parrinello and P. Mantegazza. "Improvements and Extensions to a Full-Potential Formulation Based on Independent Fields". In: *AIAA journal* 50.3 (2012), pp. 571–580.

[54] A. Parrinello and P. Mantegazza. "Independent Two-Fields Solution for Full-Potential Unsteady Transonic Flows". In: *AIAA journal* 48.7 (2010), pp. 1391–1402.

[55] A. Parrinello, M. Morandini, and P. Mantegazza. "Automatic Embedding of Potential Flow Wake Surfaces in Generic Monolithic Unstructured Meshes". In: *Journal of Aircraft* 50.4 (2013), pp. 1179–1188.

[56] G. Quaranta, P. Masarati, and P. Mantegazza. "A conservative mesh-free approach for fluid-structure interface problems". In: *International Conference for Coupled Problems in Science and Engineering, Greece*. 2005.

[57] L. Quartapelle and F. Auteri. *Fluidodinamica Incomprimibile*. Casa editrice Ambrosiana, 2013.

[58] G. Romanelli et al. "Implementation of an explicit density-based unstructured CFD solver for turbomachinery applications on graphical processing units". In: 2015.

[59] J. Roskam. *Airplane Design: Determination of stability, control, and performance characteristics, FAR and military requirements*. DARcorporation, 1985.

[60] E.A. Rothman and J.A. Violette. "Prop-fan with improved stability". Patent US 4730985 (US). 1988. URL: www.google.com/patents/US4730985.

[61] V. Shankar et al. "A fast time-accurate unsteady full potential scheme". In: *AIAA journal* 25.2 (1987), pp. 230–238.

[62] MSC Software. "MSC/NASTRAN Advanced Analysis User Guide". In: (2010).

[63] A. Stuermer. "Unsteady CFD Simulations of Contra-Rotating Propeller Propulsion Systems". In: *Paper No. AIAA-2008-5218* (2008).

[64] W.E. Sullivan, J.E. Turnberg, and J.A. Violette. *Large-scale Advanced Prop-fan (LAP) Blade Design*. Hamilton Standard Division, United Technologies, 1984. URL: www.ntrs.nasa.gov/archive/nasa/casi.ntrs.nasa.gov/19880004715.pdf.

[65] S. Timme. "Transonic aeroelastic instability searches using a hierarchy of aerodynamics models". PhD thesis. University of Liverpool, 2010.

[66] D.F. Vernon, G.S. Page, and H.R. Welge. "Propfan experimental data analysis". In: (1984). URL: www.ntrs.nasa.gov/archive/nasa/casi.ntrs.nasa.gov/19870019112.pdf.

[67] M. Vidyasagar. *Nonlinear systems analysis*. Prentice Hall, 1993.

[68] D. Vogt. "Turbomachinery Blade Vibrations, Meeting the Challange". In: *ISROMAC, Hawaii*. 2012.

[69] G. Warwick and J. Moxon. "Power of persuasion". In: *Flight International* 131 (1987), pp. 39–41.

[70] Ffowcs Williams and D. Hawkings. "Sound generation by turbulence and surfaces in arbitrary motion". In: *Philosophical Transactions of the Royal Society of London: Mathematical, Physical and Engineering Sciences* 264.1151 (1969), pp. 321–342.

[71] H. Yang. "3D unsteady flow in oscillating compressor cascade". PhD thesis. Durham University, 2004.

[72] Jr. Yates and E. Carson. *AGARD standard aeroelastic configurations for dynamic response I-wing 445.6*. Tech. rep. DTIC Document, 1988.

[73] A. Zachariadis, C. Hall, and A. Parry. "Contrarotating Open Rotor Operation for Improved Aerodynamics and Noise at Take-off". In: *Journal of Turbomachinery* 135.3 (2013).

[74] M. Zucchi. "Problemi aeroelastici dei propfan". MA thesis. Politecnico di Milano, 1986.